A Time Dependent Model of the Trade-Wind Boundary Layer

By
Bruce A. Albrecht

Department of Atmospheric Science
Colorado State University
Fort Collins, Colorado

Research report supported by the Global Atmospheric Research Program, NSF and the GATE Project Office, NOAA under grants OCD 74-21678 and 04-6-158-44036.
May 1977

Colorado State University

Department of Atmospheric Science

Paper No. 267

A TIME-DEPENDENT MODEL

OF THE TRADE-WIND BOUNDARY LAYER

By

Bruce A. Albrecht

Research Report supported by
The Global Atmospheric Research Program,
National Science Foundation and the
GATE Project Office, NOAA under grants
OCD -74-21678 and 04-6-158-44036

Department of Atmospheric Science
Colorado State University
Fort Collins, Colorado
80523

May 1977

Atmospheric Science Paper No. 267

ABSTRACT

A TIME-DEPENDENT MODEL OF THE TRADE-WIND BOUNDARY LAYER

In this dissertation a numerical model which predicts the time variation of the convective boundary layer is developed. Horizontally homogeneous conditions are assumed and the large-scale divergence field, sea surface temperature, and surface wind speed are specified externally. The model predicts the average value of mixing ratio and moist static energy in the subcloud and cloud layer and the lapse rates of these quantities in the cloud layer; the model also predicts the height of the transition layer (the layer which defines the boundary between cloud and subcloud layer) and the height of the inversion. Subcloud layer convective fluxes are specified by using the bulk aerodynamic method for specifying the surface fluxes and a mixed layer parameterization of the fluxes at the top of the subcloud layer. The moist convective processes are parameterized in terms of a mass flux which varies linearly with height and a cloud-environment difference which also varies linearly with height. Radiative fluxes are parameterized in terms of a specified cloud cover and average boundary layer heating.

The steady-state structure predicted with the model is in good agreement with the structure observed during the Atlantic Trade-Wind Experiment (ATEX). The predicted structure is warmer and more moist than that observed which is consistent with the fact that horizontal advection is not included in the model. The thermodynamic structure below the inversion is shown to be sensitive to the specification of surface wind velocity, sea surface temperature, radiative heating and cloud cover. In addition to these parameters, the height of the inversion is shown to be sensitive to the large-scale divergence.

The time-dependent capability of the model is demonstrated by simulating the reformation of the trade-wind boundary layer in the wake of disturbed conditions. The growth rate of the depth of the boundary layer is shown to be most sensitive to parameters which directly influence the surface fluxes of heat and moisture.

The model is used to study the effect of a diurnally varying radiative heating and large-scale divergence on the height of the inversion. When both effects were considered simultaneously the amplitude of the predicted variation in height was in good agreement with the amplitude observed during ATEX.

The model was also used to simulate the thermodynamic structure when the cloud layer becomes saturated (assuming no precipitation). The steady-state results of this simulation are in excellent agreement with the theoretical stratocumulus results of Lilly (1968) and Schubert (1976).

ACKNOWLEDGEMENTS

I would like to express my sincere gratitude to Dr. S. K. Cox for his guidance and encouragement during the course of this research. I would also like to thank Drs. A. K. Betts, W. H. Schubert, and D. A. Krueger for their interest and countless suggestions. A special note of appreciation is due to my wife, Nancy, for her patience and encouragement during my graduate study.

This research has been supported by The Global Atmospheric Research Program, National Science Foundation and the GATE Project Office, NOAA under grants OCD -74-21678 and 04-6-158-44036.

TABLE OF CONTENTS

TABLE OF CONTENTS - Continued

LIST OF TABLES

LIST OF FIGURES

LIST OF FIGURES - Continued

LIST OF FIGURES - Continued

LIST OF FIGURES - Continued

I. INTRODUCTION

The trade winds are one of the most persistent features of the earth's atmosphere. Associated with the trade winds is a characteristic vertical distribution of temperature and moisture which extends from the earth's surface to 1000-2000m. The trade inversion, which is characterized by a sharp increase in potential temperature and a corresponding decrease in moisture, defines the upper boundary of the trade-wind boundary layer. Below the inversion there are typically numerous shallow cumulus clouds whose tops penetrate into the trade inversion.

The earliest observational studies of the trade-wind boundary layer (e.g. Ficker; 1936) illustrated the variation of the trade-wind structure with latitude and longitude. In particular these observations showed the inversion height to increase towards the equator with the inversion occurring less frequently near the equator. Riehl et al. (1951) used radiosonde measurements made during World War II to determine the variation of temperature and moisture along a surface air trajectory in the Pacific trades. Riehl and Malkus (1957) used these data to demonstrate the role of the trades in transporting heat and moisture equatorward. Since the trades exist over approximately 20% of the earth's surface these transports are unquestionably important in terms of the earth's general circulation. Malkus (1956) and Mak (1976) have shown the importance of the horizontal variations of temperature in the trades in maintaining the trade winds themselves.

The aircraft measurements reported by Bunker et al. (1949) and Malkus (1958) provided the first detailed account of the temperature and moisture structure of the cloud and subcloud layer of the trade-wind boundary layer. These measurements showed that in the subcloud layer

potential temperature and water vapor mixing ratio did not vary significantly with height. In the cloud layer these observations showed potential temperature to increase slightly and mixing ratio to decrease slightly with height.

The investigations of Riehl et al. (1951), Riehl and Malkus (1957) and Malkus (1958) suggested the importance of convective processes in maintaining the vertical structure of the trades. Betts (1973) theorized that the cooling and moistening due to cumulus convection maintained the inversion against the warming and drying effect of the large-scale subsidence which exists in the region of the trades. During the Barbados Oceanographic and Meteorological Experiment (BOMEX), 1969, and the Atlantic Trade-Wind Experiment (ATEX), 1969, the vertical structure of temperature, moisture, and wind was periodically determined from an array of ships. These data provided a unique data set for a quantitative determination of the convective transports which exist in undisturbed trade-wind conditions. The convective fluxes were deduced from the ATEX and BOMEX data by calculating large-scale budgets of heat and moisture, estimating the radiative heating, and obtaining the convective fluxes as a residual (Augstein et al., 1973; Holland and Rasmusson, 1973; Nitta and Esbensen; 1974). These studies demonstrated the importance of the convective transports in balancing changes in the thermodynamic structure due to large-scale and radiative processes.

Although the budget studies may be used to deduce the convective fluxes, these types of studies provide little physical insight into the processes which are responsible for these fluxes. The interpretation of the BOMEX convective fluxes given by Betts (1975) and Nitta (1975) illustrated the validity of expressing the fluxes in terms of a convective

mass flux and a cloud-environment difference of thermodynamic variables. The treatment given by Betts (1975) allowed a simple interpretation of the effect of shallow non-precipitating convection on the environment in terms of subsidence warming and drying and detrainment cooling and moistening.

Although the diagnostic method used by Nitta (1975) and Betts (1975) allows the fluxes to be interpreted in terms of entrainment and detrainment processes, it does not explain what controls these processes. In a predictive model, however, it is desirable to determine the time variation of the environment due to the effect of many clouds without considering the dynamics of each individual cloud. Consequently, in order to parameterize the convective fluxes in such a model, the factors which control the entrainment and detrainment processes must be defined. Although several parameterization schemes have been proposed (Betts, 1973; Kuo, 1965, 1974; Arakawa and Schubert, 1974; Fraderich, 1973, 1976; and Esbensen, 1976), the utility of these schemes for predicting the structure observed in the trade-wind boundary layer has not been explicitly demonstrated.

Sommeria (1976) incorporated moisture into the three-dimensional turbulence model of Deardorff (1972) in order to simulate the structure of the trade-wind boundary layer. His model results are particularly suited for a detailed study of turbulent processes in the convective boundary layer. The usefulness of this approach, however, is limited by computer time requirements since a 5 h simulation requires approximately 30 h of NCAR CDC 7600 time.

Radiative processes may also be important in the determination of the trade-wind boundary-layer structure. In the diagnostic study

presented by Betts (1975), for example, the cooling due to radiative fluxes was shown to be of the same magnitude as the convective warming in the cloud and subcloud layer. Yanai et al. (1976) used the diagnostic approach to demonstrate the sensitivity of the mass flux of shallow cumulus to the specification of the radiative heating. Since it is well established that clouds can significantly alter the vertical distribution of the radiative fluxes, it is apparent that the amount of boundary-layer cloudiness may be an important parameter in determining the radiative fluxes. Boundary-layer cloudiness may in fact vary from nearly clear sky conditions to a completely overcast situation when low-level stratus are present. Consequently, the radiative fluxes may be coupled directly to the convective fluxes. Previous studies of the convective boundary layer have not, however, considered the effect of cloud cover on the radiative budget of the undisturbed boundary layer.

In this dissertation a model which predicts the time variation of the convective boundary layer is developed. Horizontally homogeneous conditions are assumed and the large-scale divergence field, sea surface temperature and surface wind speed are specified externally. The model developed predicts the time variation of the average value of mixing ratio and moist static energy in the subcloud and cloud layer and the lapse rates of these quantities in the cloud layer; the model also predicts the height of the transition layer (the layer which defines the boundary between cloud and subcloud layer) and the height of the trade inversion. The convective and radiative processes are parameterized in terms of the large-scale atmospheric structure. The atmospheric structure predicted by the model is compared to the structure observed during ATEX. The sensitivity of the model to various externally specified

parameters is determined. The time dependent capability of the model is demonstrated by using the model to simulate the reformation of the trade inversion in the wake of disturbed conditions and to study the response of the boundary-layer structure to a diurnally varying heat source and diurnally varying large-scale subsidence.

II. TIME VARIATION OF THE BOUNDARY-LAYER THERMODYNAMIC STRUCTURE

The observed thermodynamic structure of the moist trade wind regime has been documented by many researchers (Ficker, 1936; Riehl et al., 1951; Malkus, 1958; Augstein et al., 1974; and others). The average atmospheric structure that was observed during ATEX from the ship Planet (≈ 35°W, 15°N) from February 7-12 is shown in Fig. 1 (Augstein et al., 1974). The vertical profiles shown in this figure are for water vapor mixing ratio, q; dry static energy, s; moist static energy, h; and saturation static energy, h*; where by definition

$$s \equiv c_p T + gz \tag{II.1}$$

$$h \equiv c_p T + gz + Lq \tag{II.2}$$

and

$$h^* \equiv c_p T + gz + Lq^*. \tag{II.3}$$

The symbol c_p in (II.1 - II.3) is assumed to be the specific heat of dry air at constant pressure, T is absolute temperature, g is the acceleration of gravity and z is the height above the surface. The symbol L in (II.2) and (II.3) represents the latent heat of vaporization and q* in (II.3) is the saturation mixing ratio. The temperature and moisture profiles used to obtain the profiles shown in Fig. 1 were averaged with respect to the inversion height and the transition layer height in order to preserve the details of these features. The vertical coordinate used for the results shown in Fig. 1 is $\hat{p} = p_0 - p$ where p_0 is the surface pressure.

The thermodynamic structure in the trades as illustrated by Fig. 1 consists of a subcloud or mixed layer in the lowest 80 mb where mixing ratio and dry static energy are approximately constant with height. The subcloud layer and cloud layer are separated by the transition layer where moisture decreases sharply and dry static energy increases slightly. In the cloud layer, ($\hat{p}$ = 80 mb to $\hat{p}$ = 160 mb) mixing ratio decreases slightly with height while dry static energy increases with height. The cloud layer is capped by an inversion characterized by a sharp decrease in moisture and a sharp increase in dry static energy with height.

The idealized structure assumed in the model developed below is shown in Fig. 2. Although the model is formulated in terms of q and h, s is easily obtained from (II.1) and (II.2) since s = h - Lq. The idealized structure shown in Fig. 2 closely resembles the structure that is observed. It consists of a subcloud layer where mixing ratio, q_M, and moist static energy, h_M, are constant with height. The top of the subcloud layer is defined by an infinitesimally thin transition layer at $\hat{p} = \hat{p}_B$; the jump in q and h at the transition layer are given as $(\Delta q)_B = q(\hat{p}_{B+}) - q_M$ and $(\Delta h)_B = h(\hat{p}_{B+}) - h_M$.

Mixing ratio and moist static energy in the cloud layer are assumed to vary linearly with height and are represented as

$$q = q_A + \gamma_q(\hat{p} - \hat{p}_A) \tag{II.4}$$

and

$$h = h_A + \gamma_h(\hat{p} - \hat{p}_A) \tag{II.5}$$

where q_A and h_A represent mean values for the layer, γ_q and γ_h are the lapse rates of mixing ratio and moist static energy in the cloud layer,

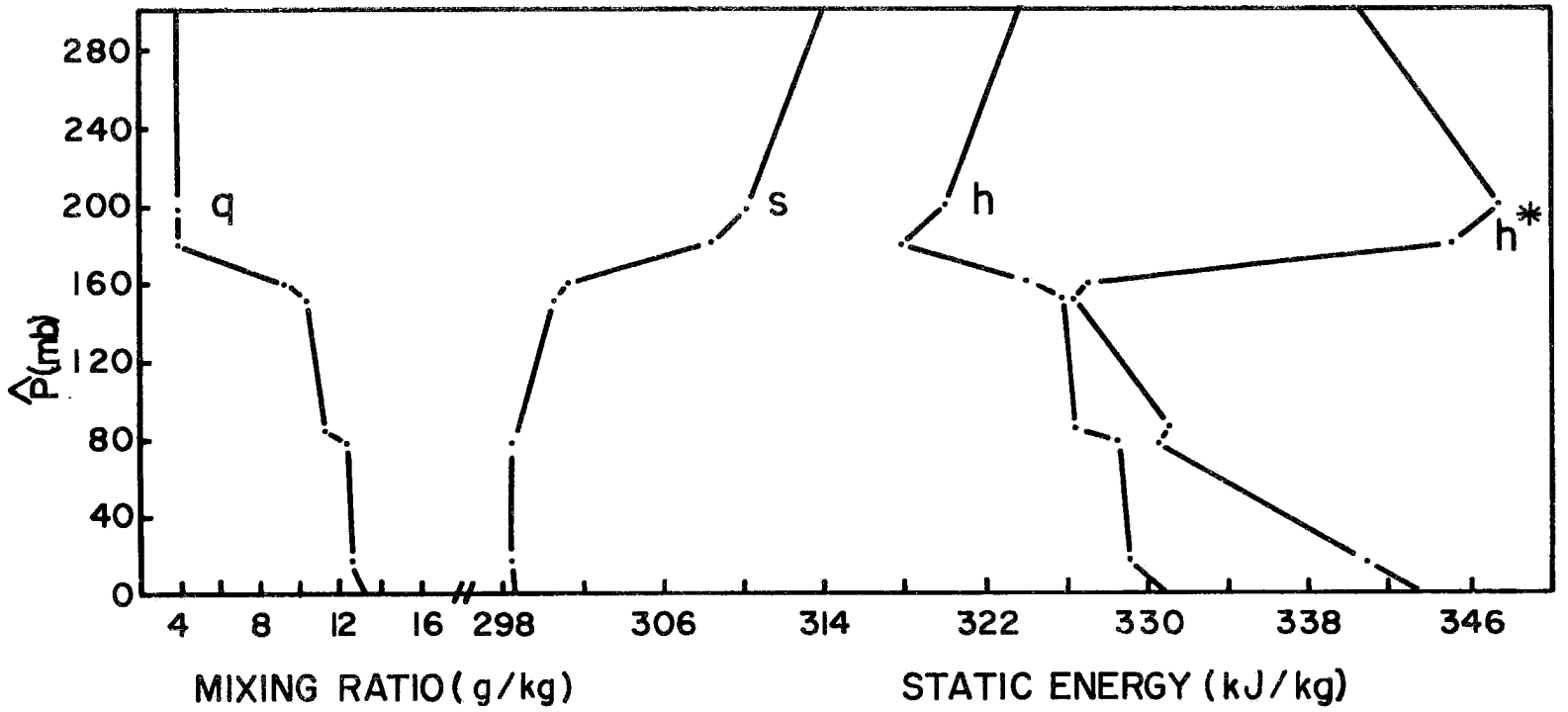

Figure 1. Vertical profiles of mixing ratio, dry static energy, moist static energy, and saturation static energy for the ship Planet, February 7-12, 1969. (Augstein et al., 1974).

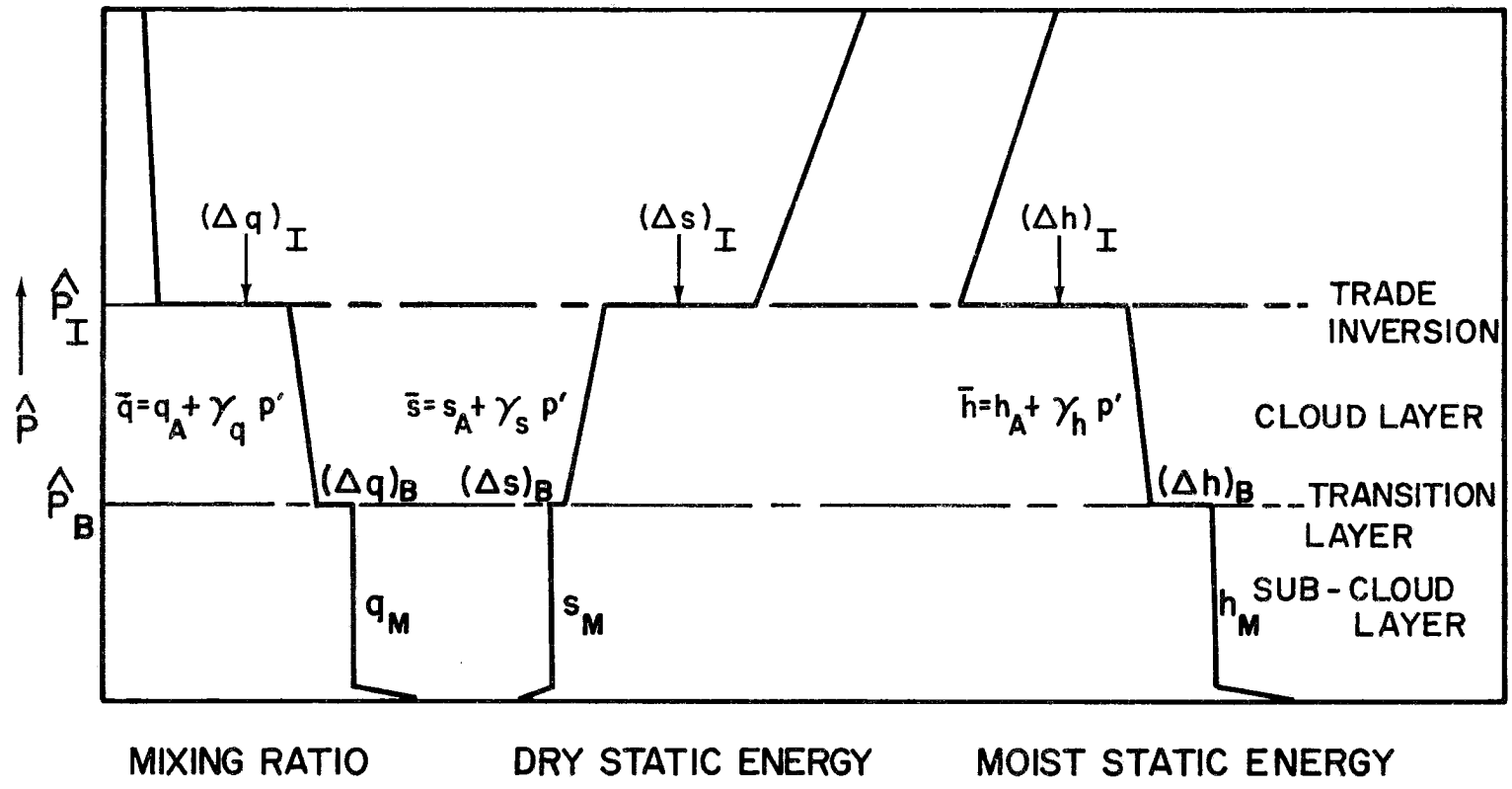

Figure 2. Idealized boundary layer structure assumed for the model.

and $\hat{p}_A$ is the pressure at the midpoint of the layer. The inversion layer which caps the cloud layer is assumed to be infinitesimally thin. The jumps in q and h across the inversion are designated as $(\Delta q)_I = q(\hat{p}_{I+}) - q(\hat{p}_{I-})$ and $(\Delta h)_I = h(\hat{p}_{I+}) - h(\hat{p}_{I-})$. The structure above the inversion is assumed to be specified or given by a separate model formulation, so that $q(\hat{p}_{I+})$ and $h(\hat{p}_{I+})$ are known quantities. A simplified structure similar to that described above was considered by Betts (1973), although he considered an inversion of finite thickness.

The purpose of this paper is to describe a model which predicts the idealized structure shown in Fig. 2. There are several processes which may alter the large-scale thermodynamic structure of the convective boundary layer. Horizontal advection and large-scale vertical motion, for example, may have a significant effect on the thermodynamic processes. Dry and moist convective processes may also result in changes in the temperature and moisture distributions and radiative processes may change the temperature structure. The interaction between these various processes is shown schematically in Fig. 3. This schematic illustrates that although the convective processes may alter the large-scale thermodynamic structure, the convective processes may be controlled by the large-scale thermodynamic and dynamic structure. Similarly radiative processes are not only a function of the large-scale and convective processes but may also alter these processes. While it will not be possible to completely consider all the possible interactions implied by Fig. 3, the basic organization of the model follows that shown in this figure.

A. Budget Equations for an Atmospheric Layer

Time variation of the structure shown in Fig. 2 may be formulated mathematically by considering the budget equations for q and h. For the

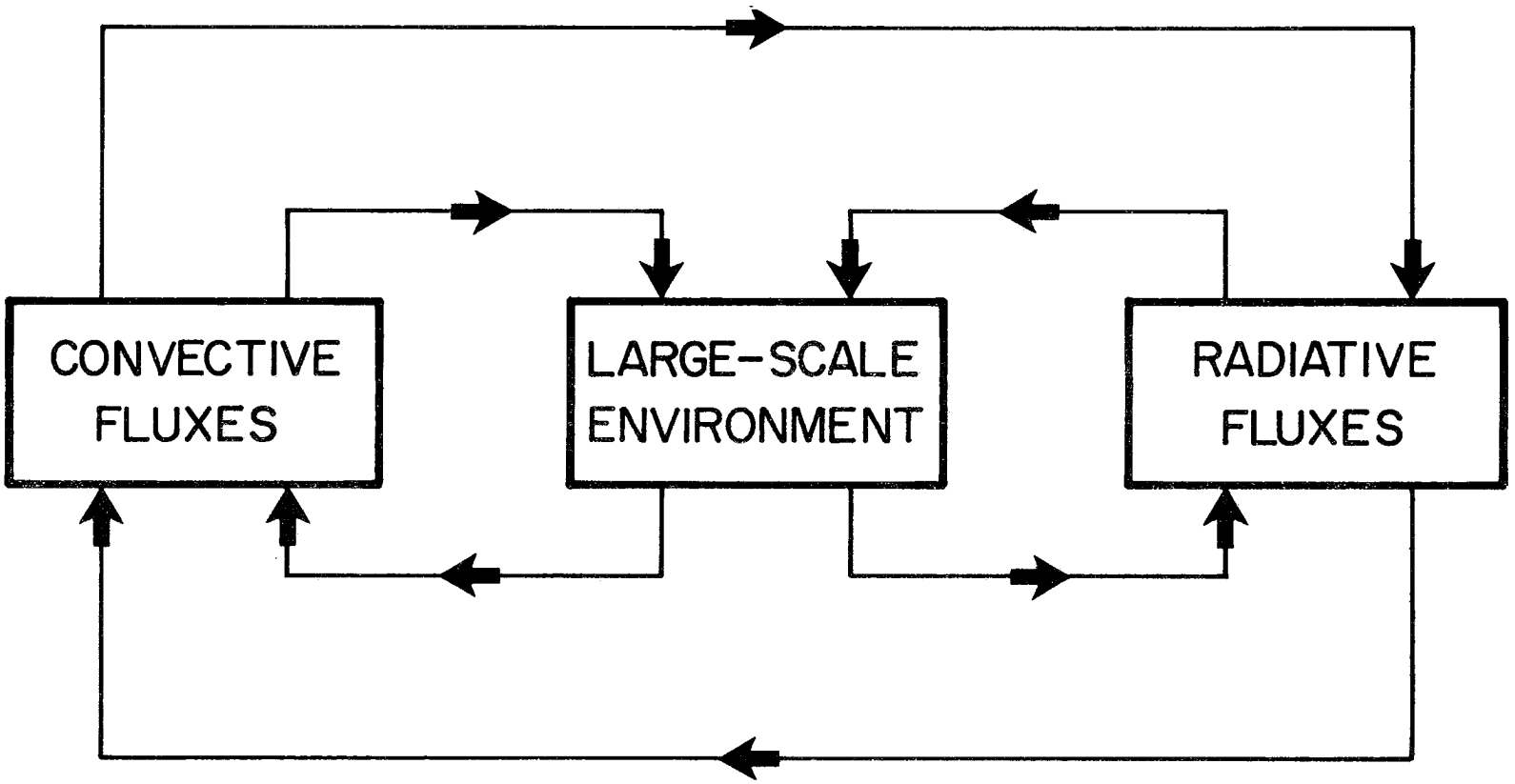

Figure 3. A schematic depicting the possible interactions between large-scale, radiative and convective processes.

general development of the time-dependent equations, the time variation of some conservative scalar quanity $\bar{x}$ is considered, where the bar denotes an average over some horizontal area. The general equations developed for $\bar{x}$ are then applied to the quantities q and h where sources and sinks of these quantities are included in the equations where appropriate.

The conservation of $\bar{x}$ may be written approximately as (c.f. Yanai et al., 1973)

$$\frac{\partial \bar{x}}{\partial t} + \overline{\vec{V}_h \cdot \vec{\nabla}_h \bar{x}} + \hat{\omega} \frac{\partial \bar{x}}{\partial \hat{p}} = -g \frac{\partial F_x}{\partial \hat{p}} \qquad \text{(II.6)}$$

where $\vec{V}_h$ is the horizontal wind vector, $\hat{\omega} \equiv \frac{d\hat{p}}{dt}$ and F_x is the flux of x due to subgrid-scale transports. Furthermore, if horizontally homogeneous conditions are assumed, (II.6) may be reduced to

$$\frac{\partial x}{\partial t} = - \hat{\omega} \frac{\partial x}{\partial \hat{p}} - g \frac{\partial F_x}{\partial \hat{p}} \qquad \text{(II.7)}$$

where the bar has been dropped for convenience. In the derivation given here x is assumed to be linear with pressure within the layer of interest such that

$$x(\hat{p}) = x_A + \gamma_x (\hat{p} - \frac{\hat{p}_1 + \hat{p}_2}{2}) \qquad \text{(II.8)}$$

where $\hat{p}_1$ and $\hat{p}_2$ are the pressure levels of the bottom and top boundaries of the layer, respectively. Substituting (II.8) into (II.7) results in the expression

$$\frac{\partial x_A}{\partial t} + \frac{\partial \gamma_x}{\partial t}(\hat{p} - \hat{p}_A) - \gamma_x \frac{\partial \hat{p}_A}{\partial t} = -\hat{\omega}\,\gamma_x - g\frac{\partial F_x}{\partial \hat{p}} \qquad \text{(II.9)}$$

where $\hat{p}_A = \frac{\hat{p}_1 + \hat{p}_2}{2}$. Since the L.H.S. of (II.9) is linear with pressure, it is assumed that F_x is quadratic with pressure and $\hat{\omega}$ is constrained to be linear with pressure. The linear dependence of $\hat{\omega}$ is specified as

$$\hat{\omega} = \hat{\omega}_1 - \overline{D}(\hat{p} - \hat{p}_1) \qquad \text{(II.10)}$$

where $\overline{D}$ is equivalent to the mean divergence in the layer and defined as $\overline{D} \equiv \frac{(\hat{\omega}_2 - \hat{\omega}_1)}{\hat{p}_2 - \hat{p}_1}$. With these assumptions, (II.9) may be integrated from $\hat{p}_1$ to some level $\hat{p}$ to give

$$\frac{\partial x_A}{\partial t} + \frac{1}{2}(\hat{p} - \hat{p}_2)\frac{\partial \gamma_x}{\partial t} - \frac{\gamma_x}{2}\left(\frac{\partial \hat{p}_1}{\partial t} + \frac{\partial \hat{p}_2}{\partial t}\right) \qquad \text{(II.11)}$$

$$= -\gamma_x\left[\hat{\omega}_1 - \frac{\overline{D}}{2}(\hat{p} - \hat{p}_1)\right] - g\left[F_x - (F_x)_1\right]/(\hat{p} - \hat{p}_1).$$

Evaluation of (II.11) at $\hat{p} = \hat{p}_A$ and $\hat{p} = \hat{p}_1$ yields the expressions

$$\frac{\partial x_A}{\partial t} = \frac{1}{4}(\hat{p}_2 - \hat{p}_1)\frac{\partial \gamma_x}{\partial t} + \frac{\gamma_x}{2}\left(\frac{\partial \hat{p}_1}{\partial t} + \frac{\partial \hat{p}_2}{\partial t}\right) - \gamma_x\left(\frac{3}{4}\hat{\omega}_1 + \frac{1}{4}\hat{\omega}_2\right)$$

$$- 2g\,[(F_x)_A - (F_x)_1]/(\hat{p}_2 - \hat{p}_1) \qquad \text{(II.12)}$$

and

$$\frac{\partial x_A}{\partial t} = \overbrace{\frac{\gamma_x}{2}\left(\frac{\partial \hat{p}_1}{\partial t} + \frac{\partial \hat{p}_2}{\partial t}\right)}^{A} - \overbrace{\frac{\gamma_x}{2}(\hat{\omega}_2 + \hat{\omega}_1)}^{B} \overbrace{-g\,[(F_x)_2 - (F_x)_1]/(\hat{p}_2 - \hat{p}_1)}^{C} \qquad \text{(II.13)}$$

Combining (II.12) and (II.13) results in the expression

$$\frac{\partial \gamma_x}{\partial t} = \overbrace{\bar{D}\,\gamma_x}^{A} \overbrace{- 4g[(F_x)_2 - 2(F_x)_A + (F_x)_1]/(\hat{p}_2 - \hat{p}_1)^2}^{B} \qquad \text{(II.14)}$$

Note that (II.13) and (II.14) may be used to predict the time rate of change of x_A and γ_x provided there exists an expression for term A in (II.13). This term represents variations in the mean value of x due to changes in the mean height of the layer. Term B in (II.13) represents variations in x_A due to the mean vertical pressure velocity in the layer

and term C is equivalent to the first derivative of the flux. Term A in (II.14) represents variations in the slope due to the derivative of the mean vertical pressure velocity and term B is equivalent to the second derivative of the flux. There are specific cases when (II.13) and (II.14) may be significantly simplified. These cases are more easily derived if the slope γ_x is written as $\gamma_x = \frac{\Delta x}{\Delta \hat{p}}$ where $\Delta x = x_2 - x_1$ and $\Delta \hat{p} = \hat{p}_2 - \hat{p}_1$. Consider, for example, the case when $\Delta x \to 0$ for all t. In this case (II.13) reduces to

$$\frac{\partial x_A}{\partial t} = -g \frac{[(F_x)_2 - (F_x)_1]}{(\hat{p}_2 - \hat{p}_1)} \tag{II.15}$$

while (II.14) becomes $$(F_x)_A = \frac{(F_x)_1 + (F_x)_2}{2} . \tag{II.16}$$

Eq. (II.15) simply indicates that if x is constant with pressure the change in x depends only on the differences of the fluxes across the layer. Furthermore, if x is to remain constant throughout the layer, (II.16) indicates that the fluxes must be linear with pressure.

Eq. (II.13) and (II.14) are also simplified if $\Delta p \to 0$, which is the case when the layer becomes infinitesimally thin. For this case (II.13) reduces to

$$\Delta x(\frac{\partial \hat{p}_1}{\partial t} - \hat{\omega}_1) = g\,[(F_x)_2 - (F_x)_1] \tag{II.17}$$

while (II.14) becomes

$$(F_x)_A = \frac{(F_x)_1 + (F_x)_2}{2} \quad . \tag{II.18}$$

In this case the budget equation reduces to an equation which can be used to predict the height of the infinitesimally thin layer. In the absence of a discontinuity of the fluxes across the layer, the height of the layer is simply determined by the large-scale pressure velocity field.

B. Budget Equations for the Boundary Layer

The time variation of the structure shown in Fig. 2 is easily defined with the aid of (II.13)-(II.15). The effect of radiation is included in the equations for h as a flux divergence since

$$\frac{\partial T}{\partial t})_{\text{radiation}} = \frac{-g}{c_p} \frac{\partial F_R}{\partial \hat{p}}$$

where F_R is the net radiative flux at a level. With this formulation the time variation of h_M and q_M are defined from (II.15) as

$$\frac{\partial h_M}{\partial t} = -g \frac{[(F_h)_{B-} - (F_h)_0]}{\hat{p}_B} - g \frac{[(F_R)_{B-} - (F_R)_0)]}{\hat{p}_B} \tag{II.19}$$

and

$$\frac{\partial q_M}{\partial t} = -g \frac{[(F_q)_{B-} - (F_q)_0]}{\hat{p}_B} \qquad \text{(II.20)}$$

where $\hat{p}_B$ refers to the height of the mixed layer, F_R are radiative fluxes, the subscript B- refers to the fluxes at the top of the mixed layer but below the transition layer, while the subscript 0 refers to fluxes at the surface. Since only non-precipitating convection is being considered there are no sources or sinks of q_M in (II.20). Physically, (II.19) and (II.20) are easily interpreted since they simply relate the time variation of subcloud layer mixing ratio and moist static energy to the divergence of the fluxes. Similar equations describing the time variation of mixed layer and subcloud layer quantities have been discussed by Lilly (1968), Betts (1973), Ogura and Cho (1974), Arakawa and Schubert (1974) and others.

In the cloud layer the equation predicting the mean value of h is easily obtained from (II.13) as

$$\frac{\partial h_A}{\partial t} = \gamma_h \left(\frac{\partial \hat{p}_A}{\partial t} - \hat{\omega}_A\right) - g \frac{[(F_h)_{I-} - (F_h)_{B+}]}{(\hat{p}_I - \hat{p}_B)} - g \frac{[(F_R)_{I-} - (F_R)_B]}{(\hat{p}_I - \hat{p}_B)} \qquad \text{(II.21)}$$

where $\frac{\partial \hat{p}_A}{\partial t} = \frac{1}{2}\left(\frac{\partial \hat{p}_B}{\partial t} + \frac{\partial \hat{p}_I}{\partial t}\right)$,

and $\hat{\omega}_A = \frac{1}{2}(\hat{\omega}_I + \hat{\omega}_B)$.

The I- subscript in (II.21) refers to the fluxes just below the inversion, while B+ refers to fluxes just above the transition layer. The time variations of $\hat{p}_B$ and $\hat{p}_I$ which appear in (II.21) will be defined below. The subgrid scale fluxes in the cloud layer are due to moist cumulus convection. Consequently, the appropriate conservative moisture quantity in the cloud layer is not mixing ratio q but total water $q + \ell$ where ℓ is the liquid water content. Betts (1975), however, suggested that the time variation of the mean liquid water content in the trade wind boundary layer may be neglected. With this assumption the equation describing the time variation of the average mixing ratio in the cloud layer may be written as

$$\frac{\partial q_A}{\partial t} = \gamma_q \left(\frac{\partial \hat{p}_A}{\partial t} - \hat{\omega}_A\right) - g \frac{\left[(F_{q+\ell})_{I-} - (F_{q+\ell})_{B+}\right]}{(\hat{p}_I - \hat{p}_B)} . \qquad \text{(II.22)}$$

Note that the convective fluxes in (II.22) are the fluxes of total water.

Equation (II.14) may be used to determine how the lapse rates of h and q in the cloud layer vary with time. These equations may be written

$$\frac{\partial \gamma_h}{\partial t} = \overline{D}\gamma_h - 4g \frac{\left[(F_h)_{I-} - 2(F_h)_A + (F_h)_{B+}\right]}{(\hat{p}_I - \hat{p}_B)^2} - 4g \frac{\left[(F_R)_{I-} - 2(F_R)_A + (F_R)_{B+}\right]}{(\hat{p}_I - \hat{p}_B)^2} \qquad \text{(II.23)}$$

and $$\frac{\partial \gamma_q}{\partial t} = \overline{D}\gamma_q - 4g \frac{[(F_{q+\ell})_{I-} - 2(F_{q+\ell})_A + (F_{q+\ell})_{B+}]}{(\hat{p}_I - \hat{p}_B)^2}, \qquad \text{(II.24)}$$

where the A subscript refers to fluxes at the midpoint of the cloud layer.

The budget equations for the transition layer and the inversion layer are easily derived from (II.17). For the transition layer these equations become

$$(\Delta h)_B \left(\frac{\partial \hat{p}_B}{\partial t} - \hat{\omega}_B\right) = g\,[(F_h)_{B+} - (F_h)_{B-}], \qquad \text{(II.25)}$$

and $$(\Delta q)_B \left(\frac{\partial \hat{p}_B}{\partial t} - \hat{\omega}_B\right) = g\,[(F_{q+\ell})_{B+} - (F_q)_{B-}], \qquad \text{(II.26)}$$

where $\hat{\omega}_B$ is the vertical velocity at the top of the subcloud layer.

The discontinuity in the radiative fluxes at cloud base has been assumed to be zero. For the inversion layer the budget equations become

$$(\Delta h)_I \left(\frac{\partial \hat{p}_I}{\partial t} - \hat{\omega}_I\right) = -g\,(F_h)_{I-} + g\,[(F_R)_{I+} - (F_R)_{I-}] \qquad \text{(II.27)}$$

and $$(\Delta q)_I \left(\frac{\partial \hat{p}_I}{\partial t} - \hat{\omega}_I\right) = -g\,(F_{q+\ell})_{I-} \qquad \text{(II.28)}$$

where the convective fluxes at the top of the inversion have been assumed to be zero. A discontinuity in the radiative fluxes is included in (II.27) to account for the cloud-top cooling of clouds penetrating the inversion. A similar discontinuity in the radiative fluxes is considered in models of stratocumulus convection (Lilly, 1968; Schubert, 1976). Eq. (II.25)-(II.28) predict the height of the subcloud layer and the height of the trade inversion. Using these expressions, $\frac{\partial \hat{p}_B}{\partial t}$ and $\frac{\partial \hat{p}_I}{\partial t}$ which appear in (II.21) and (II.22) may be eliminated.

C. Summary

The equations derived in this chapter formalize the time variation of the boundary layer structure in terms of the large-scale subsidence and the convective and radiative fluxes. In this model the subsidence (divergence) is specified as an external parameter. Consequently, if the convective and radiative fluxes can be formalized in terms of the large-scale thermodynamic structure, the equations derived in this chapter will represent a closed set of equations which can be used to predict the boundary layer structure. Chapters III and IV are devoted to the parameterization of the convective and radiative fluxes. The numerical integration of the equations derived in this chapter will be considered in Chapter V.

III. PARAMETERIZATION OF CONVECTIVE PROCESSES

The predictive equations developed in Chapter II may be solved provided the convective and radiative fluxes appearing in those equations are expressed in terms of the large-scale fields. In this chapter the parameterization of the convective fluxes in the cloud and subcloud layer are considered.

A. Subcloud Layer Fluxes

The budget equations for the subcloud layer are expressed in terms of the surface fluxes, $(F_h)_o$ and $(F_q)_o$, and the fluxes at the top of the mixed layer, $(F_h)_{B-}$ and $(F_q)_{B-}$. The bulk aerodynamic method is used to specify the surface fluxes and a mixed layer k closure is used to specify the fluxes at the top of the subcloud layer.

The bulk aerodynamic method gives the surface fluxes as

$$(F_q)_o = \rho_o C_q V_o (q_o - q_M) \tag{III.1}$$

and

$$(F_h)_o = \rho_o C_T V_o (s_o - s_M) + \rho_o C_q V_o L (q_o - q_M) \tag{III.2}$$

where ρ_o is the density of air near the surface, V_o is the wind speed above the surface, s_o is $c_p T_o$ where T_o is the sea surface temperature and q_o is the saturation mixing ratio of air at the sea surface temperature. The coefficients C_q and C_T in (III.1) and (III.2) are the bulk aerodynamic coefficients for moisture and sensible heat transfer. In

conventional usage the bulk aerodynamic formulation of the surface fluxes is applied at a height of 10 m above the ocean surface. The sub-cloud layer moisture and temperature predicted by the model described here, however, refer to the mixed layer which is above the surface layer. In the ATEX data the surface layer extends to 100-150 m so that the differences $(q_o - q_M)$ and $(s_o - s_M)$ will be larger than the corresponding air-sea differences at 10 m height. Consequently, the transfer coefficients obtained from measurements made at 10 m height (C_T' and C_q') should be appropriately reduced when the surface fluxes are defined from data at a higher level (Fissel et al., 1977). The ATEX Planet data suggest that C_T and C_q given in (III.1) and (III.2) be obtained by multiplying C_T' and C_q' by a factor of $\simeq 0.9$ in order to use $(q_o - q_M)$ and $(s_o - s_M)$ to specify the surface fluxes.

The coefficients C_T' and C_q' may be evaulated by comparing surface fluxes measured directly to values of $\rho_o V_o(s_o - s')$ and $\rho_o V_o(q_o - q')$. Friche and Schmitt (1976) made such a comparison for several independent data sets. They found $C_q' \sim 1.3X10^{-3}$ and $C_T' \sim 1.4X10^{-3}$. There was, however some uncertainty in the values of C_T' and some indication that this coefficient varied with the stability. For convenience it is assumed that $C_T' = C_q' = 1.3X10^{-3}$ so that $C_T = C_q = 1.15X10^{-3}$.

The fluxes at the top of the mixed layer are specified by assuming that

$$(F_{sv})_{B-} = -k(F_{sv})_o \qquad \text{(III.3)}$$

where $(F_{sv})_{B-}$ is the flux of virtual dry static energy just below cloud base, $(F_{sv})_o$ is the surface flux for virtual dry static energy at the surface and k is a constant. Similar closure schemes have been used in treatments of the dry mixed layer and the subcloud layer (Lilly, 1968; Betts, 1973; Tennekes, 1973; and others). While there have been numerous values of k assumed or determined by laboratory and field measurements (Stull, 1976a), it is assumed here that k = .25 unless noted otherwise.

The virtual fluxes of dry static energy in the subcloud layer may be defined as

$$F_{sv} = F_h - (1 - \delta\varepsilon') LF_q \qquad \text{(III.4)}$$

where $\delta = .608$ and $\varepsilon' = \frac{c_p \overline{T}}{L}$.

Consequently, (III.3) relates $(F_h)_{B-}$ and $(F_q)_{B-}$ to the surface fluxes which are given by (III.1) and (III.2). If it is assumed that the discontinuities in h and q at the transition layer are maintained at the same height, (II.25) and (II.26) may be combined to give the relationship

$$\frac{(F_q)_{B-}}{(\Delta q)_B} - \frac{(F_h)_{B-}}{(\Delta h)_B} = \frac{(F_{q+\ell})_{B+}}{(\Delta q)_B} - \frac{(F_h)_{B+}}{(\Delta h)_B} \qquad \text{(III.5)}$$

The cloud-layer fluxes $(F_h)_{B+}$ and $(F_{q+\ell})_{B+}$ which appear in (III.5) are defined in the following section. Presently, it is convenient to note that the definitions given below result in the expression

$$\frac{(F_{q+\ell})_{B+}}{(\Delta q)_B} = \frac{(F_h)_{B+}}{(\Delta h)_B} \tag{III.6}$$

Eq. (III.6), (III.5), (III.4) and (III.3) may then be combined to give the fluxes at the top of the subcloud layer as

$$(F_q)_{B-} = - \frac{k(\Delta q)_B}{(\Delta s_v)_B} (F_{sv})_o \tag{III.7}$$

and

$$(F_h)_{B-} = - \frac{k(\Delta h)_B}{(\Delta s_v)_B} (F_{sv})_o. \tag{III.8}$$

Eq. (III.1), (III.2), (III.7), and (III.8) provide expressions for the subcloud layer convective fluxes needed in (II.19) and (II.20).

B. Cloud Layer Fluxes

The basic formulation in the fluxes of the cloud layer of the model is similar to the formulation suggested by Ooyama (1971), Yanai, et al., (1973), and Betts (1975). The basic assumption in this scheme is that the convective fluxes may be separated into a characteristic mass flux associated with the convective elements, and the difference between the

thermodynamic characteristics of the cloud and its environment. Using this formulation, the flux of some quanity of x due to convective elements may be written as

$$g F_x = \frac{\sigma}{1-\sigma} (x_c - \bar{x}) (\hat{\omega}_c - \bar{\hat{\omega}}) \qquad \text{(III.9)}$$

where σ is the fractional area covered by active updrafts, x_c represents a characteristic in-cloud value of the quantity x and $\hat{\omega}_c$ represents a characteristic cloud velocity. The barred quantities in (III.9) represent mean values which are defined as

$$\bar{\hat{\omega}} \equiv \sigma \hat{\omega}_c + (1-\sigma) \hat{\omega}_e \qquad \text{(III.10)}$$

and

$$\bar{x} \equiv \sigma x_c + (1-\sigma) x_e \qquad \text{(III.11)}$$

where the subscript e refers to values in the environment. A complete derivation of (III.9) is given by Yanai, et al., (1973).

Typically, $\hat{\omega}_c >> \bar{\hat{\omega}}$ so that (III.9) may be approximated as

$$g F_x \simeq \frac{\sigma \hat{\omega}_c}{1-\sigma} (x_c - \bar{x}). \qquad \text{(III.12)}$$

Furthermore, if the fractional area of active updrafts is small ($\sigma << 1$), (III.12) is further reduced to

$$g F_X \simeq \sigma \hat{\omega}_c (x_c - \bar{x}) \qquad \text{(III.13)}$$

where $\sigma \hat{\omega}_c$ is the convective mass flux.

Using (III.13), the fluxes of moist static energy and total water in the model may be defined as

$$gF_h = \hat{\omega}^* (h_c - \bar{h}) \qquad \text{(III.14)}$$

and

$$gF_{q+\ell} = \hat{\omega}^* (q_c + \ell_c - \bar{q}) \qquad \text{(III.15)}$$

where $\hat{\omega}^* = \sigma\hat{\omega}_c$ is the convective mass flux. Eq. (III.14) and (III.15) are equivalent to the formulation used by Yanai, et al., (1973) and Betts (1975). In the parameterization scheme presented below $\hat{\omega}_c$ is defined to represent a characteristic velocity of all active clouds averaged over the active lifetime of these clouds. The cloud-environment differences in (III.14) and (III.15) are also defined as an average over the lifetime of these clouds. With these definitions the convective fluxes given by (III.14) and (III.15) may be formulated without considering a spectrum of clouds such as that employed by Arakawa and Schubert

(1974). Betts (1975) demonstrated the validity of using such a transient cloud model to diagnostically specify the convective fluxes for shallow non-precipitating convection.

The parameterization of the convective fluxes in the cloud layer are somewhat simplified since the profiles of $\bar{q}$ and $\bar{h}$ are linear with pressure in the cloud layer. Consequently, the fluxes in the cloud layer are assumed to vary quadratically with pressure. For simplicity, it is assumed that the mass flux and cloud-environment differences that appear in (III.14) and (III.15) vary linearly with pressure. With this assumption (III.14) and (III.15) may be written as

$$g(F_h) = -\omega_B^*(1 + \mu p')\ (\Delta h)_{CB}\ (1 + \lambda_h p') \qquad \text{(III.16)}$$

and

$$g(F_{q+\ell}) = -\omega_B^*(1 + \mu p')\ (\Delta q)_{CB}\ (1 + \lambda_q p') \qquad \text{(III.17)}$$

where $p' \equiv \hat{p} - \hat{p}_B$, $-(\Delta h)_{CB}$, and $-(\Delta q)_{CB}$ are the cloud-environment differences at cloud base, and ω_B^* is the mass flux at cloud base. The parameters μ, λ_h, and λ_q give the vertical distribution of mass flux and cloud-environment differences. The remainder of this chapter will be devoted to the derivation of relationships which give ω_B^*, $(\Delta h)_{CB}$, $(\Delta q)_{CB}$, λ_h, λ_q and μ.

The cloud-environment differences at cloud base are specified by assumirg that the air rising into clouds has properties similar to that of the subcloud layer. Observations, however, indicate that air near the

base of clouds is slightly more moist and possibly cooler than the surrounding subcloud layer (Betts, et al. 1974 and LeMone and Pennell, 1976). In the aircraft measurements made by LeMone and Pennell, for example, the air just beneath clouds was typically more moist by $\simeq .4$ g kg^{-1} and cooler by $\simeq .1°C$ than the surrounding subcloud layer. The ATEX profiles shown in Fig. 1 also indicate that for cloud base to be at the transition layer, cloud parcels rising out of the mixed layer would have to be more moist and/or cooler than the mixed layer air. If the deviations of h_c and q_c from the subcloud layer values are defined as δh and δq, the cloud environment differences at cloud base may be written as

$$-(\Delta h)_{CB} = -(\Delta h)_B + \delta h \qquad \text{(III.18)}$$

and

$$-(\Delta q)_{CB} = -(\Delta q)_B + \delta q. \qquad \text{(III.19)}$$

No attempt is made here to theoretically quantify δq and δh. For simplicity it is assumed that

$$\frac{\delta q}{(\Delta q)_B} = \frac{\delta h}{(\Delta h)_B} = \frac{\delta s}{(\Delta s)_B} \qquad \text{(III.20)}$$

and that δq is specified as a constant. It is interesting to note that with (III.16) - (III.20), (III.5) reduces to

$$\frac{(F_q)_{B-}}{(\Delta q)_B} = \frac{(F_h)_{B-}}{(\Delta h)_B} . \qquad \text{(III.21)}$$

A similar equation is obtained if the δh and δq parameters are not considered. As demonstrated by LeMone and Pennell the parcels rising into the clouds may account for a significant portion of the subcloud layer fluxes at cloud base. Consequently, (III.20) insures the consistency of the cloud base fluxes with the deviation of the cloud parcels from the mixed layer values.

The cloud base mass flux, ω_B^* may be determined by defining cloud base to be at the top of the mixed layer. This assumption is used by Betts (1973), Sarachik (1974) and Stull (1976b) and is used below to define the fluxes of F_h and $F_{q+\ell}$ at cloud base from which ω_B^* may be determined.

If cloud parcels are to become saturated at the top of the mixed layer, then by definition

$$q_M + \delta q = \frac{\varepsilon\, e_s\,(T_B + \delta T)}{p_o - \hat{p}_B - e_s(T_B + \delta T)} \qquad \text{(III.22)}$$

where T_B is the temperature of the subcloud air at cloud base, $\delta T = \delta s/c_p$ is the deviation of the temperature of the cloud parcel from the mean air temperature at the top of the mixed layer, $\varepsilon = .622$, and $e_s\,(T_B + \delta T)$ is the saturation vapor pressure of air at the temperature $T_B + \delta T$. Eq. (III.22) is an expression which relates q_M, s_M and $\hat{p}_B$. Consequently, the time variation of the height of the subcloud layer is not independent of the time variation of s_M and q_M if (III.22) is

assumed. The dependence of $\frac{\partial \hat{p}_B}{\partial t}$ on $\frac{\partial s_M}{\partial t}$ and $\frac{\partial q_M}{\partial t}$ may be quantified by differentiating (III.22) with respect to time. This operation results in the expression

$$\tilde{\omega}_B \equiv \frac{\partial \hat{p}_B}{\partial t} = \frac{T^* \, p^*}{(T^* - \kappa T_B)(q_M + \delta_q)} \frac{\partial q_M}{\partial t} - \frac{(p_o - \hat{p}_B) T_B}{(T^* - \kappa T_B)} \frac{1}{s_M} \frac{\partial s_M}{\partial t} \tag{III.23}$$

where $p^* = \hat{p}_o - p_B - e_s$, $T^* = \frac{4098.0}{(T_B + \delta t - 35.86)^2}$ and $\kappa = R/c_p$. Eq. (III.23) was derived by assuming $\frac{\partial(\delta q)}{\partial t} = \frac{\partial(\delta T)}{\partial t} = \frac{\partial p_o}{\partial t} = 0$. A complete derivation of (III.23) is given in Appendix A. The predictive equations for q_M and h_M [Eq. (II.18) and Eq. (II.19)] may be used to eliminate the time derivatives of s_M and q_M from (III.23). With this operation $\tilde{\omega}_B$ may be written as

$$\tilde{\omega}_B = - \frac{gT^*p^* \left[(F_q)_{B-} - (F_q)_o\right]}{\hat{p}_B (T^* - \kappa T_B)(q_M + \delta q)} + \frac{g (p_o - \hat{p}_B) T_B \left[(F_s)_{B-} - (F_s)_o + (F_R)_B - (F_R)_o\right]}{\hat{p}_B (T^* - \kappa T_B) s_M} \tag{III.24}$$

where $F_s = F_h - LF_q$. The mixed layer convective fluxes which appear in

(III.24) are given by (III.1), (III.2), (III.7) and (III.8). The radiative fluxes will be formulated in Chapter IV. Eq. (III.23) may be combined with (II.25) and (II.26) to write $(F_h)_{B+}$ and $(F_{q+\ell})_{B+}$ as

$$(F_h)_{B+} = (F_h)_{B-} + \frac{(\Delta h)_B}{g} (\tilde{\omega}_B - \hat{\omega}_B) \qquad \text{(III.25)}$$

and

$$(F_{q+\ell})_{B+} = (F_q)_{B-} + \frac{(\Delta q)_B}{g} (\tilde{\omega}_B - \hat{\omega}_B). \qquad \text{(III.26)}$$

Eq. (III.25) and (III.26) simply give the flux discontinuity across the transition layer that is required to maintain the height of the transition layer at cloud base. Consequently, as the mixed layer cools or moistens ($\tilde{\omega}_B < 0$) the discontinuity in the convective fluxes across the transition layer decreases since $(\Delta h)_B < 0$ and $(\Delta q)_B < 0$. On the other hand, if the large-scale subsidence increases the magnitude of the flux discontinuity increases. The discontinuity in the fluxes also depends on the magnitude of $(\Delta h)_B$ and $(\Delta q)_B$. For example as $(\Delta h)_B \to 0$ the convective flux $(F_h)_{B+} \to (F_h)_{B-}$, while as $(\Delta h)_B$ increases the discontinuity in the cloud base fluxes also increases. While the fluxes $(F_h)_{B+}$ and $(F_{q+\ell})_{B+}$ are the parameters which are needed to specify the fluxes given in the predictive equations, it is useful to note that the cloud-base mass flux may be given as

$$\omega_B^* = \frac{-g(F_{q+\ell})_{B+}}{(\Delta q)_{CB}} = \frac{-g(F_h)_{B+}}{(\Delta h)_{CB}} \qquad \text{(III.27)}$$

The cloud-environment difference in thermodynamic variables which is represented in (III.16) and (III.17) may be formalized by considering the entrainment relationships

$$\frac{\partial(q_c + l_c)}{\partial \hat{p}} = - \frac{E}{\delta \hat{p}} (q_c + l_c - \bar{q}) \qquad \text{(III.28)}$$

and

$$\frac{\partial h_c}{\partial \hat{p}} = \frac{E}{\delta \hat{p}} (h_c - \bar{h}) \qquad \text{(III.29)}$$

where the subscript c refers to cloud parcel properties and E is an entrainment parameter assumed to be constant with pressure. Similar entrainment relationships have been used by Ooyama (1971), Yanai et al. (1973), Arakawa and Schubert (1974), and Betts (1975). Since $\bar{q}$ and $\bar{h}$ in (III.28) and (III.29) are linear functions of pressure these expressions are easily integrated to obtain the expressions

$$(h_c - \bar{h}) = [\frac{\gamma_h \delta \hat{p}}{E} - (\Delta h)_{CB}] \exp (\frac{-Ep'}{\delta \hat{p}}) - \frac{\gamma_h \delta \hat{p}}{E} \qquad \text{(III.30)}$$

and

$$(q_c + l_c - \bar{q}) = [\frac{\gamma_q \delta \hat{p}}{E} - (\Delta q)_{CB}] \exp (\frac{-Ep'}{\delta \hat{p}}) - \frac{\gamma_q \delta \hat{p}}{E} \qquad \text{(III.31)}$$

where the boundary conditions (III.18) and (III.19) have been applied.

To obtain a linear cloud-environment difference (III.30) and (III.31) are approximated as

$$h_c - \bar{h} = - (\Delta h)_{CB} (1 + \lambda_h p') \qquad \text{(III.32)}$$

and

$$q_c + \ell_c - \bar{q} = - (\Delta q)_{CB} (1 + \lambda_q p') \qquad \text{(III.33)}$$

where $\lambda_h = (\frac{\gamma_h}{(\Delta h)_{CB}} - \frac{E}{\delta \hat{p}}) (1 - \frac{E}{3})$ and $\lambda_q = (\frac{\gamma_q}{(\Delta q)_{CB}} - \frac{E}{\delta \hat{p}}) (1 - \frac{E}{3})$.

A derivation of the λ_h and λ_q in (III.32) and (III.33) is given in Appendix B. For realistically possible values of γ_h, γ_q, $(\Delta h)_{CB}$, and $(\Delta q)_{CB}$, the linear cloud-environment differences given by (III.32) and (III.33) differ from the exact solutions given by (III.30) and (III.31) by less than 10% at all levels for $E \leq .60$ and less than 3% for $E \leq .20$.

The entrainment parameter E which appears in the cloud-environment differences (III.32) and (III.33) is determined by assuming that the cloud-environment difference in virtual temperature averaged over the cloud layer is a constant. This is approximately equivalent to assuming that the buoyancy force averaged over the depth of the cloud layer, $\delta \hat{p}$, is a constant. Mathematically this constraint may be written as

$$\frac{1}{c_p \delta \hat{p}} \int_0^{\delta \hat{p}} (s_{vc} - \bar{s}_v) \, dp' = \Delta T_o \qquad \text{(III.34)}$$

where ΔT_o is a constant, s_{vc} is the virtual dry static energy of the cloud parcels and $\bar{s}_v$ is the virtual dry static energy of the environment. Constraints similar to (III.34) have been used in the parameterization theories proposed by Betts (1973) and Arakawa and Schubert (1974). The way in which they applied this constraint, however, is different than that being proposed here. In the model proposed by Betts (1973) an inversion of finite depth was considered. The negative buoyancy of cloud parcels in the inversion layer was constrained to be a specified fraction of the positive buoyancy generated in the cloud layer. In this formulation however, the entrainment parameter E was specified and the stratification of the large-scale environment was altered to satisfy the buoyancy constraint and a liquid water constraint. In the Arakawa and Schubert (1974) parameterization scheme a cloud work function, $A(\lambda)$, for a particular cloud type λ was defined as the vertical integral of the buoyancy force weighted by the normalized mass flux distribution. The quasi-equilibrium assumption used to close the Arakawa and Schubert parameterization was that $\frac{\partial A(\lambda)}{\partial t} = 0$. This expression is basically equivalent to (III.34) although the buoyancy force is not weighted by the mass flux distribution in (III.34). In the Arakawa and Schubert treatment, however, the cloud type is synonymous with a specific entrainment rate and the quasi-equilibrium assumption is applied to determine the cloud-base mass flux for each cloud type.

In the parameterization scheme being presented here, the constraint given by (III.34) is used to determine the entrainment parameter E. Qualitatively (III.34) indicates that if the environmental lapse rate of s_v becomes less stable the entrainment rate would have to increase in order to maintain the integrated buoyancy force as a constant. This

increased entrainment would in fact result in a tendency with time for the convection to stabilize the layer. This is demonstrated more clearly by combining (II.23) and (II.24) to obtain an equation which predicts the time rate of change of the lapse rate of s due only to convective processes as

$$\frac{\partial \gamma_s}{\partial t})_{conv} = -4g\,[(F_{s\ell})_{I-} - 2(F_{s\ell})_A + (F_{s\ell})_{B+}] / \delta p^2 \qquad \text{(III.35)}$$

where $F_{s\ell} \equiv F_h - LF_{q+\ell}$.

The convective flux of $F_{s\ell}$ may be determined from (III.16), (III.17), (III.32) and (III.33) so that (III.35) may be written as

$$\frac{\partial \gamma_s}{\partial t})_{conv} = 2\,\omega_B{}^*\mu\,(\gamma_s - \frac{E(\Delta s)_{CB}}{\delta \hat{p}})\,(1-\frac{E}{3}). \qquad \text{(III.36)}$$

The results given by Betts (1975) indicate that $\omega_B{}^*\mu$ which appears in (III.36) is less than zero for undisturbed conditions. Consequently, the term $-\omega_B{}^*\mu\,(1-\frac{E}{3})\,\frac{E(\Delta s)_{CB}}{\delta \hat{p}}$ is positive and represents a stabilization of the environment. It is interesting to note that if E=0, (III.36) predicts the equilibrium lapse rate to be $\gamma_s = 0$ in the absence of any radiative or large-scale processes. With the constraint given by (III.34), E will typically be greater than zero unless the environment becomes sufficiently stable.

Qualitatively the dependence of E on the stability implied by the buoyancy constraint is easily demonstrated if virtual effects are neglected. The cloud-environment difference in this case may be written as

$$(s_c - \bar{s}) = \frac{1}{1+\gamma} \; (h_c - \bar{h}^*) \qquad \text{(III.37)}$$

where γ is defined in Appendix C and is assumed to be constant. For the qualitative argument given here it is assumed that $\bar{h}^*$ is a linear function of p' and that $(h_c - \bar{h}^*)_{B+} = 0$. With these assumptions $(h_c - \bar{h}^*)$ in (III.37) may be written as

$$h_c - \bar{h}^* = (\gamma_{hc} - \gamma_{h^*})\, p' \qquad \text{(III.38)}$$

where $\gamma_{hc} = \frac{\partial h_c}{\partial p'}$ and $\gamma_{h^*} = \frac{\partial \bar{h}^*}{\partial p'}$ and γ_{hc} and γ_{h^*} are constant with pressure. Substituting (III.38) into the buoyancy constraint (III.34) gives

$$\gamma_{hc} \simeq \gamma_{h^*} + 2(1+\gamma)\, c_p\, \Delta\bar{T}_o \,/\delta\hat{p}. \qquad \text{(III.39)}$$

If it is assumed from (III.32) that $\lambda_h \simeq \left(\frac{\gamma_h}{(\Delta h)_{CB}} - \frac{E}{\delta\hat{p}}\right)$ then $\gamma_{hc} = \frac{E(\Delta h)_{CB}}{\delta\hat{p}}$.

Eq. (III.39) may then be written as

$$E = \frac{\delta \hat{p} \gamma_{h^*}}{(\Delta h)_{CB}} + \frac{2(1+\gamma)\, c_p \Delta T_o}{(\Delta h)_{CB}} . \qquad \text{(III.40)}$$

From (III.40) the dependence of E on the stability of the layer and on the specification of ΔT_o becomes more apparent. As the layer becomes more unstable $\gamma_h{}^*$ becomes more negative which results in E being greater since $(\Delta h)_{CB}$ is less than zero. This larger E, as illustrated from (III.36), would result in a stabilization of the environment. The effect of ΔT_o is also apparent from (III.40). Since $\frac{2(1+\gamma)\, c_p \Delta T_o}{(\Delta h)_{CB}}$ is a negative quantity, the larger the value of ΔT_o, the smaller E becomes. Eq. (III.36) indicates that this smaller value of E would result in a destabilization of the environment.

The exact form of the constraint given by (III.34) may be determined by noting that if the effect of liquid water is considered, the cloud-environment difference of virtual dry static energy may be written as

$$(s_{vc} - \bar{s}_v) = (s_c - \bar{s}) + \delta\varepsilon' L(q_c - \bar{q}) - \varepsilon' L \ell_c \qquad \text{(III.41)}$$

where, as in (III.4), $\varepsilon' = \frac{c_p \bar{T}}{L}$ and $\delta = .608$. It is convenient to approximate (III.41) as a linear function of pressure. Such an expression is derived in Appendix C and is given as

$$(s_{vc} - \bar{s}_v) = -\beta(\Delta h)_{CB}\ (1+\lambda_h p') + \varepsilon' L(\Delta q)_{CB}\ (1+\lambda_q p')$$

$$-\alpha L\ [\bar{q}_B^* - \bar{q}_{B+} + (\gamma_q^* - \gamma_q)\ p'] \qquad \text{(III.42)}$$

where λ_h and λ_q are defined by (III.32) and (III.33), q_B^* is the saturation mixing ratio of air just above the transition layer and γ_q^* is the lapse rate of saturation mixing ratio in the cloud layer. The coefficients, ε', β and α are assumed to be constant and are specified as $\varepsilon' = 288\ c_p/L$, $\beta = .500$ and $\alpha = .312$ where $L = 2.45 \times 10^6\ J \cdot kg^{-1}$ and $c_p = 1005\ J \cdot kg^{-1} \cdot K^{-1}$. Using (III.42) in the buoyancy constraint (III.34) results in the expression

$$c_p\ \Delta T_o = -\beta(\Delta h)_{CB} + \varepsilon' L(\Delta q)_{CB} - \alpha L(q_B^* - \bar{q}_B) + [-\beta(\Delta h)_{CB}\ \lambda_n$$

$$+ \varepsilon' L(\Delta q)_{CB}\ \lambda_q - \alpha L(\gamma_q^* - \gamma_q)]\ \frac{\delta \hat{p}}{2}\ . \qquad \text{(III.43)}$$

Since λ_n and λ_q in (III.43) depend only on the entrainment factor E and large-scale variables, E is easily obtained by combining (III.43) with the definition of λ_h and λ_q to give

$$E = \frac{-b - \sqrt{b^2 - 4\ ac}}{2a} \qquad \text{(III.44)}$$

where $a = [-\beta(\Delta h)_{CB} + \varepsilon' L(\Delta q)_{CB}] / 3,$

$$b = -3a + (\beta\delta\hat{p}\gamma_h - \varepsilon' L\delta\hat{p}\gamma_q) / 3,$$

and $$c = -\beta\delta\hat{p}\gamma_h + \varepsilon' L\delta\hat{p}\gamma_q - \alpha L\delta\hat{p}(\gamma_q^* - \gamma_q) - 2 [\beta(\Delta h)_{CB} - \varepsilon' L(\Delta q)_{CB}$$

$$+ \alpha L(\bar{q}_B^* - \bar{q}_B) + c_p\Delta T_o].$$

The jump in the thermodynamic variables at cloud base result in a small area of negative buoyancy just above cloud base. This area is represented by the $-\beta(\Delta h)_{CB} + L(\Delta q)_{CB} - \alpha L(\bar{q}_B^* - \bar{q}_B)$ term in (III.43). Because of this small negative area it is possible for a given value of ΔT_o that the E determined from (III.44) may be small and possibly negative. This possibility is eliminated by requiring that $E \geq .1$. If E from (III.44) is less than this limit, the equality is assumed. In the results given in Chapter V the sensitivity of the predicted structure to the specification of ΔT_o will be determined.

The factor, μ, which appears in (III.16) and (III.17) remains to be specified in order to close the cumulus parameterization scheme. Betts (1975) has expressed the mass flux in terms of entrainment and detrainment processes. Betts (1975) and Fraedrich (1976) used a transient cloud model to illustrate the concept of detrainment and its effect on the mass flux. The derivation given here follows their treatments and is more of a conceptual argument than an exact mathematical derivation.

In the transient cloud model the important concept is that cloud properties are defined over the lifetime of the cloud. To formalize this concept a very simple cloud model is considered. This cloud model has a uniform updraft velocity, $\hat{\omega}_{co}$, during the active lifetime of the cloud. Consequently, if the mass budget of the cloud is considered, the fractional area covered by the active updraft of an individual cloud, σ_i, may be approximated from the entrainment relationship

$$\frac{\partial \sigma_i}{\partial \hat{p}} = \frac{E}{\delta \hat{p}} \sigma_i \qquad \text{(III.45)}$$

where E is the entrainment factor described above. Although the solution of (III.45) is clearly an exponential function, this solution will be approximated as

$$\sigma_i \simeq \sigma_{io} \left(1 + \frac{E}{\delta \hat{p}} p'\right) \qquad \text{(III.46)}$$

where σ_{io} is the fractional area covered by the active updraft at cloud base. The mass flux due to an individual cloud at any given time during the active life cycle of the cloud may then be written as

$$\sigma_i\,\hat{\omega}_c = \begin{cases} \hat{\omega}_{co}\,\sigma_{io}\,(1 + \frac{E}{\delta\hat{p}}\,p'), & 0 < p' < \hat{\omega}_{co}(t-t_o) \\ 0, & p' \geq \hat{\omega}_{co}(t-t_o) \\ 0, & p' \geq \delta\hat{p} \end{cases} \qquad \text{(III.47)}$$

where t_o is the time at which the cloud begins to grow. The formulation given in (III.47) was made by assuming that the upper boundary of the updraft region moves with the updraft velocity. It is also assumed that the influence of the convection is not felt above the infinitesimally thin inversion so that the mass flux goes to zero at $\hat{p}_{I+}$.

The mass flux given by (III.47) averaged over the lifetime of the cloud, τ_{CLD}, may be written as

$$\widetilde{\sigma_i\,\hat{\omega}_c} = \begin{cases} \hat{\omega}_{co}\,\sigma_{oi}\,(1 + \frac{E}{\delta\hat{p}}\,p')\,(1 - \frac{p'}{\hat{\omega}_{co}\,\tau_{CLD}}), & p' \leq \delta\hat{p} \\ 0, & p' > \delta\hat{p} \end{cases} \qquad \text{(III.48)}$$

where $$\widetilde{\sigma_i\hat{\omega}_c} = \frac{1}{\tau_{CLD}} \int_0^{\tau_{CLD}} \sigma_i\,\hat{\omega}_c\,dt'.$$

If an ensemble of active clouds is considered where each cloud has a mass

flux associated with it of that given by (III.48), the mass flux due to all convective elements may be written as

$$\omega^* = \begin{cases} \omega_B^* \left(1 + \frac{Ep'}{\delta\hat{p}}\right)\left(1 - \frac{\sigma_o p'}{\omega_B^* \tau_{CLD}}\right), & p' \leq \delta\hat{p} \\ 0, & p' > \delta\hat{p} \end{cases} \tag{III.49}$$

where if the number of clouds per unit area is N

$$\omega^* \equiv \sum_i^N \sigma_i \tilde{\hat{\omega}}_c, \quad \omega_B^* \equiv \sum_i^N \hat{\omega}_{co}\, \sigma_{oi} \text{ and } \sigma_o \equiv \sum_i^N \sigma_{oi}.$$

In the formulation given by (III.16) and (III.17) the mass flux is assumed to be linear. To linearize (III.49) for $p' < \delta\hat{p}$ it is assumed that

$$\int_0^{\delta\hat{p}} \omega_B^* \left(1 + \mu p'\right) dp' = \int_0^{\delta\hat{p}} \omega_B^* \left(1 + \frac{Ep'}{\delta p}\right)\left(1 - \frac{\sigma_o p'}{\omega_B^* \tau_{CLD}}\right) dp' \tag{III.50}$$

which upon integration gives

$$\mu = \frac{E}{\delta\hat{p}} - \frac{\sigma_o}{\omega_B^* \tau_{CLD}} \left(1 + \frac{2}{3} E\right) \text{ for } p' \leq \delta\hat{p} \qquad \text{(III.51)}$$

while (III.49) indicates that

$$\mu = \frac{-1}{p'} \text{ for } p' > \delta\hat{p}.$$

As demonstrated by Betts (1975) using a similar derivation, the $\frac{\sigma_o}{\omega_B^* \tau_{CLD}} X \left(1 + \frac{2}{3} E\right)$ term represents a decrease in mass flux with height which is equivalent to a detrainment of cloud mass. Betts used BOMEX data to show that this term may dominate the mass flux distribution in undisturbed conditions resulting in a mass flux which decreases with height. The discontinuity in the mass flux at the inversion represents a detrainment of mass at this level due to a loss of buoyancy by the clouds. A similar detrainment process is considered by Arakawa and Schubert (1974).

While the derivation of (III.51) can hardly be considered rigorous, the importance of considering the effect of the cloud over its lifetime is demonstrated. This derivation has also introduced two additional parameters σ_o and τ_{CLD}. Some physical interpretations of these parameters may be made by noting that if there is no entrainment that (III.51) may be combined with (III.36) to write

$$\left(\frac{\partial \gamma_s}{\partial t}\right)_{conv} = -\frac{2\sigma_o \gamma_s}{\tau_{CLD}} . \qquad \text{(III.52)}$$

This equation is a simple differential equation which has an exponential solution provided σ_o/τ_{CLD} is constant. The time constant for this exponential solution is

$$\tau_{adj} \equiv \frac{\tau_{CLD}}{2\sigma_o} . \qquad \text{(III.53)}$$

Consequently, for no entrainment (III.51) and (III.53) may be combined to give

$$\tau_{adj} = \frac{-1}{2\mu\omega_B^*} . \qquad \text{(III.54)}$$

From the results given by Betts (1975) appropriate values of ω_B^* and μ are $\omega_B^* \simeq 150$ mb day^{-1} and $\frac{1}{\mu} = -80$ mb. From (III.54) this gives an adjustment time of 1/3 - 1/4 of a day. For a τ_{adj} of 1/3 of a day and a cloud cover of active updrafts of .02 at cloud base, (III.53) gives $\tau_{CLD} \simeq 20$ minutes. Unfortunately, the adjustment time is not as easily defined when there is entrainment since E is a function of the atmospheric structure. Furthermore, τ_{CLD} and σ_o are parameters which are not easily obtained from observations since σ_o refers only to active or

growing clouds. Consequently, for simplicity it is assumed that $\tau_{adj} = \tau_{CLD}/2\sigma_o$ = constant so that μ may be defined for (III.24) from (III.51) as

$$\mu = \frac{E}{\delta\hat{p}} - \frac{1}{2\omega_B^* \tau_{adj}} (1 + \frac{2}{3} E) \qquad \text{(III.55)}$$

where τ_{adj} is specified as an external parameter. The sensitivity of the model results to τ_{adj} will be determined in Chapter V.

The role of τ_{adj} may be further evaluated by noting the time rate of change of s just above the transition layer due to convective processes. This may be determined by evaluating the expression

$$\frac{\partial s(\hat{p}_{B+})}{\partial t} = -g \frac{\partial F_{s\ell}}{\partial \hat{p}})_{\hat{p} = \hat{p}_{B+}} \qquad \text{(III.56)}$$

provided that $\frac{\partial \hat{p}_B}{\partial t} = 0$. The appropriate expression for $F_{s\ell}$ derived from (III.32) and (III.33) may be written as

$$F_{s\ell} = - \omega_B^* (1 + \mu p') (\Delta s)_{CB} (1 + \lambda_s p')$$

where $$\lambda_s \simeq \left[\frac{\gamma_s}{(\Delta s)_{CB}} - \frac{E}{\delta\hat{p}}\right]$$

and μ is given by (III.55). With this definition Eq. (III.56) may be written as

$$\frac{\partial s(\hat{p}_{B+})}{\partial t} = \omega_B^* \gamma_s - \frac{(\Delta s)_{CB}}{2\tau_{adj}} (1 + \frac{2}{3} E). \qquad \text{(III.57)}$$

This is similar to the expression obtained by Betts (1975) where $\omega_B^* \gamma_s$ represents the warming due to cumulus induced subsidence and

$$- \frac{(\Delta s)_{CB}}{2\tau_{adj}} (1 + \frac{2}{3} E)$$

represents the cooling due to the detrainment. Eq. (III.57) represents an interesting control on the jumps in s at cloud base since the greater this jump becomes the greater the cooling at cloud base which tends to decrease the jump in s as a function of time. The time scale for this process is simply $\frac{1}{\tau_{adj}} (1 + \frac{2}{3} E)$.

Using (III.16) and (III.17) and the definitions given above for $(\Delta h)_{CB}$, $(\Delta q)_{CB}$, ω_B^*, λ_h, λ_q, and μ the fluxes at the cloud-layer mid-level may be written as

$$(F_h)_A = (F_h)_{B+} (1 + \mu\delta\hat{p}/2) (1 + \lambda_h\delta\hat{p}/2), \qquad \text{(III.58)}$$

and $$(F_{q+\ell})_A = (F_{q+\ell})_{B+} (1 + \mu\delta\hat{p}/2) (1 + \lambda_q\delta\hat{p}/2) \qquad \text{(III.59)}$$

where λ_h, λ_q and μ are given by (III.32), (III.33), and (III.55) respectively.

A slight complication exists in the specification of the fluxes at the top of the cloud layer. This complication arises from the constraint that the inversion is infinitesimally thin and at the same height in the temperature and moisture field. In the real atmosphere the height and/or thickness of the inversion in the temperature profile may differ slightly from that in the moisture field. If the inversion in the temperature and moisture field are to remain at the same level for all time, the predictive equations for the height of the inversion (II.27) and (II.28) imply that

$$\frac{(F_h)_{I-} - (\Delta F_R)_I}{(\Delta h)_I} = \frac{(F_{q+\ell})_{I-}}{(\Delta q)_I} \tag{III.60a}$$

or alternately

$$\frac{(F_{s\ell})_{I-} - (\Delta F_R)_I}{(\Delta s)_I} = \frac{(F_{q+\ell})_{I-}}{(\Delta q)_I} \tag{III.60b}$$

where $(\Delta F_R)_I = (F_R)_{I+} - (F_R)_{I-}$. A similar consistency relationship is considered in the stratocumulus model described by Lilly (1968) and Schubert (1976). The fluxes given by (III.16) and (III.17), however, do not satisfy (III.60) by definition. In order to insure that (III.60) is satisfied it is assumed that

$$(F_h)_{I-} = (F_h)_{I-}^{conv} + (F_h)_{I-}^{res}, \tag{III.61a}$$

$$(F_{q+\ell})_{I-} = (F_{q+\ell})_{I-}^{conv} + (F_{q+\ell})_{I-}^{res} \qquad \text{(III.61b)}$$

and

$$(F_{s\ell})_{I-} = (F_{s\ell})_{I-}^{conv} + (F_{s\ell})_{I-}^{res} \qquad \text{(III.61c)}$$

where $(F_h)_{I-}^{conv}$, $(F_{q+\ell})_{I-}^{conv}$ and $(F_{s\ell})_{I-}^{conv}$ are the fluxes given by (III.16) and (III.17). $(F_h)_{I-}^{res}$, $(F_{q+\ell})^{res}$ and $(F_{s\ell})_{I-}^{res}$ are residual fluxes, introduced to allow the inversion height to be predicted consistently in both the moisture and the thermal fields and hence insure that (III.60) is satisfied. Ideally these residual fluxes will be small. There may be several ways in which the inversion height may be predicted and the resulting residual fluxes evaluated. In this model it is assumed that the time variation of the inversion height is predicted as

$$\frac{\partial \hat{p}_I}{\partial t} = \hat{\omega}_{I-} - g \frac{[(F_{s\ell})_{I-}^{conv} - (\Delta F_R)_I]}{(\Delta s)_I} . \qquad \text{(III.62)}$$

This expression implies that $(F_{s\ell})_{I-}^{res} = 0$ and hence $L(F_{q+\ell})_{I-}^{res} = (F_h)_{I-}^{res}$. Physically (III.62) implies that the temperature field determines the height of the inversion and that the height of the discontinuity in the moisture profile adjusts to this height. The flux required for this adjustment is simply given as $(F_{q+\ell})_{I-}^{res}$. In actuality it is the stable layer in the temperature profile (if virtual effects are neglected) which determines where the clouds detrain and the mass flux goes to zero.

If for example, the moisture discontinuity was located slightly below the temperature discontinuity, the convection would penetrate the moisture discontinuity and detrain at the discontinuity in the temperature profile. This process would result in a significant moistening above the moisture discontinuity which could be interpreted as an increase in the height of the moisture discontinuity. If initially the moisture discontinuity had been above the inversion, the cloud detrainment would have taken place below this level. In this case, the cloud layer itself would be moistened although the absence of a flux discontinuity across the moisture discontinuity would allow the large-scale subsidence to decrease the height of the discontinuity.

It is instructive to note that it would have been possible to adjust the moisture discontinuity to the height predicted by (III.62) without introducing a residual flux. This procedure, however, may result in a non-conservative loss or gain of moisture from the boundary layer. By introducing a residual flux which is also used in the equations which predict the value of q in the cloud layer, the total water of the boundary-layer system is conserved. The adjustment of the inversion height in this case is at the expense of the mean water content of the cloud layer.

With the assumption that $L(F_{q+\ell})_{I-}^{res} = (F_h)_{I-}^{res}$, (III.61) may be combined with (III.60) to write the residual flux as

$$(F_h)_{I-}^{res} = L(F_{q+\ell})_{I-}^{res} = \frac{\left\{\frac{(\Delta h)_I}{(\Delta q)_I}(F_{q+\ell})_{I-}^{conv} - (F_h)_{I-}^{conv} + (\Delta F_R)_I\right\}}{\left\{1 - \frac{(\Delta h)_I}{L(\Delta q)_I}\right\}} \qquad \text{(III.63)}$$

where $$(F_{q+\ell})^{conv}_{I-} = (F_{q+\ell})_{B+} (1 + \mu\delta\hat{p}) (1 + \lambda_q\delta\hat{p}) \qquad \text{(III.64a)}$$

and $$(F_h)^{conv}_{I-} = (F_h)_{B+} (1 + \mu\delta\hat{p}) (1 + \lambda_h\delta\hat{p}). \qquad \text{(III.64b)}$$

Eq. (III.64) and (III.63) may be combined with (III.61) to define the fluxes $(F_h)_{I-}$ and $(F_{q+\ell})_{I-}$. It is interesting to note that in a 60 hr simulation of the growth of the trade-wind boundary layer $L(F_{q+\ell})^{res}_{I-}$ has an average value of 1 Wm^{-2} and a standard deviation of $\pm$ 3 Wm^{-2}. A complete summary of the convective fluxes used in the model is given in Chapter V.

C. Summary

In this chapter cloud and subcloud layer fluxes have been parameterized in terms of the large-scale structure. In the subcloud layer the surface fluxes are specified by the bulk aerodynamic method while the fluxes at the top of the subcloud layer are parameterized by a mixed layer k closure.

The fluxes in the cloud layer are assumed to be quadratic with respect to pressure and are specified in terms of a linear mass flux and a linear cloud-environment difference. The important concept of the convective parameterization is the transient cloud model. With this concept the mass flux and the cloud-environment differences are interpreted as averages over the lifetime of the cloud. Three major assumptions are made in order to completely specify the convective fluxes in terms of the large-scale variables. The first closure

assumption is that cloud base is assumed to be at the top of the mixed layer. This constraint allows the discontinuity of the convective fluxes at cloud base to be defined and thus specifies the cloud base mass flux. The second assumption is that the buoyancy force averaged through the cloud layer is a constant. This constraint defines an entrainment rate for the convective processes. The third assumption assumes that the ratio of the lifetime of the clouds to the fractional area covered by active or growing clouds at cloud base is a constant. This constraint specifies the detrainment process as defined for a very simple transient cloud model.

IV. THE PARAMETERIZATION OF RADIATIVE PROCESSES

The predictive equations which were developed in Chapter I require the specification of the radiative fluxes. The radiative heating in the boundary layer is determined by the absorption and emission of longwave radiation (in the wavelength interval of 3-60 μm) and the absorption of shortwave radiation (in the wavelength interval of .3-3 μm) by various atmospheric constituents. Although the heating may vary with the quantity of ozone, carbon dioxide, and water vapor in the atmosphere; clouds have been clearly shown to be the principal modulators of the radiative processes (e.g. Cox, 1968; and Starr, 1976). In this chapter the sensitivity of the longwave and shortwave heating rates to variations in water vapor content and cloud cover will be determined.

Since the model described above is constrained to have a constant s in the mixed layer and linear s in the cloud layer, the relevant radiative processes are only those which change the mean values of s in the cloud and subcloud layer and those which change the lapse rate of s in the cloud layer. It is also necessary to determine the discontinuity in the radiative fluxes at the inversion in order to predict the height of the inversion. Although a detailed radiative transfer scheme could be used to determine the radiative fluxes, this approach would not only be computationally time consuming but would also result in vertical detail in the heating rates that would be irrelevant to the model structure. To avoid this complication, heating rates for several representative boundary layer structures will be determined from a detailed broadband radiative transfer calculation. These detailed calculations will then be used to develop a simple parameterization of the radiative process

in terms of the temperature, moisture and cloud cover distributions.

Although trade cumulus are finite clouds, the radiation processes will be investigated separately for clear sky conditions and for clouds of infinite horizontal extent. The radiative heating rates will then be determined as a weighted average of heating rates determined for clear and cloudy conditions. This approach has some short-comings in that the radiative properties of finite clouds may be significantly different than those of infinite horizontal extent (McKee and Cox, 1974; McKee and Cox, 1976). Unfortunately, the treatment of radiative transfer in finite clouds is far from being definitive, and the treatment of finite clouds and particularly an ensemble of finite clouds is virtually nonexistent.

A. Longwave Heating Rates

The two basic atmospheric structures used for the calculation of clear sky longwave fluxes are shown in Fig. 4 and 5. Model atmosphere I shown in Fig. 4 is similar to the temperature and moisture structure observed from the ship Planet during ATEX (see Fig. 2). The mixed layer temperature profile is linear with pressure and approximately the dry adiabatic lapse rate. The inversion at cloud base and at the trade inversion are assumed to have a thickness of 5 mb for the transfer calculation. Model atmosphere II is shown in Fig. 5 and is similar to model I except that the trade inversion is approximately 30 mb lower.

The basic atmospheric structures shown in Fig. 4 and 5 were systematically altered in order to determine the sensitivity of the calculated longwave fluxes to variations in temperature and moisture. A summary of the modifications of model I and II that were used for the radiative transfer calculation is given in Table I. The basic modifications

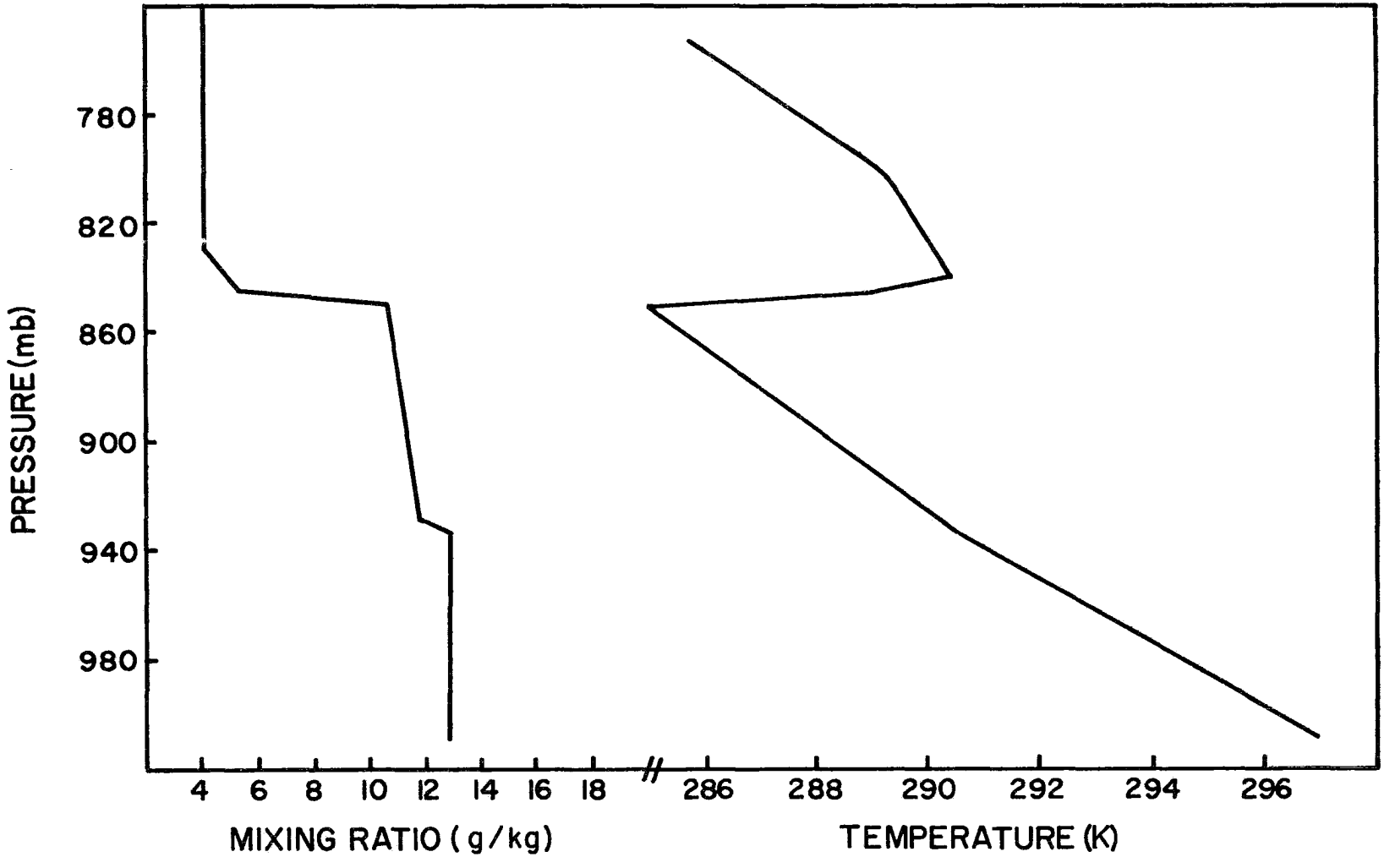

Figure 4. Model atmosphere I temperature and moisture structure assumed for clear sky radiative transfer calculations.

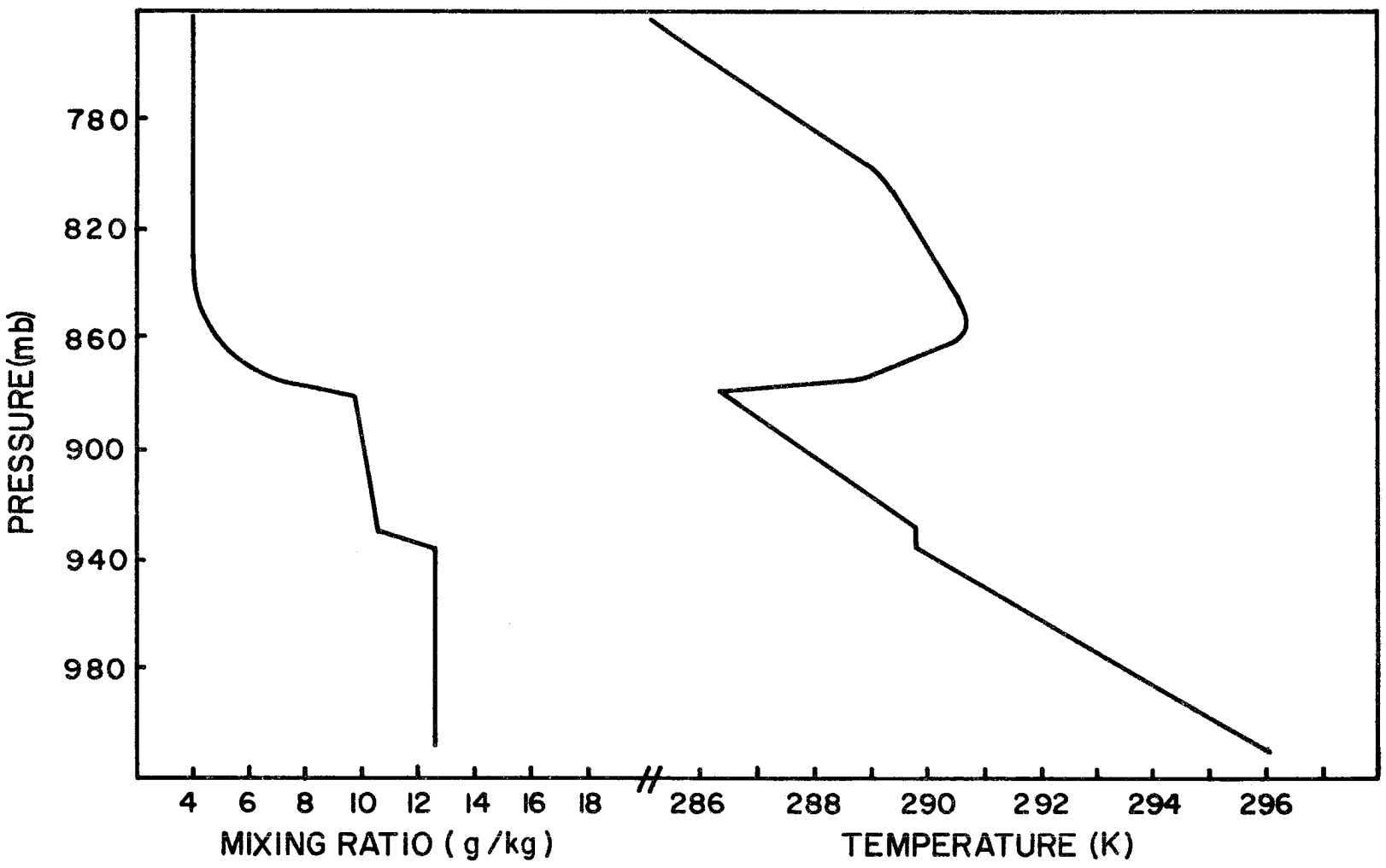

Figure 5. Model atmosphere II temperature and moisture structure assumed for clear sky radiative transfer calculations.

MODEL ATMOSPHERE	$\hat{p}_B$ (mb)	$\hat{p}_I$ (mb)	q_M (g Kg^{-1})	q_A (g Kg^{-1})	γ_q (g Kg^{-1} mb^{-1})	γ_T (°C mb^{-1})
I-0	82.5	167.5	12.9	11.80	0.0	-.0675
I-1	82.5	167.5	12.9	11.20	-.015	-.0675
I-2	82.5	167.5	12.9	10.60	-.03	-.0675
I-3	82.5	167.5	12.9	9.80	-.05	-.0675
II-0	82.5	132.5	12.3	10.50	0.0	-.0675
II-1	82.5	132.5	12.3	10.10	-.015	-.0675
II-2	82.5	132.5	12.3	9.75	-.03	-.0675
II-3	82.5	132.5	12.3	9.25	-.05	-.0675
IA-1	82.5	132.5	14.9	13.20	-.015	-.0675
IIA-1	82.5	132.5	12.3	11.10	-.015	-.0675
IIA-3	82.5	132.5	12.3	10.25	-.050	-.0675
IB-1	82.5	132.5	12.9	11.20	-.015	-.0350
IB-3	82.5	132.5	12.9	9.80	-.050	-.0350
IIB-1	82.5	132.5	12.3	10.10	-.015	-.0350
IIB-3	82.5	132.5	12.3	9.25	-.050	-.0350

TABLE I. Model atmospheres used for radiative transfer calculations.

consist of systematically varying the lapse rate of moisture and temperature in the cloud layer.

The broadband radiative transfer calculation described by Cox (1973) was used to obtain clear sky cooling rates. This calculation includes the effect of continuum pressure broadening, which was shown theoretically by Cox (1973) to be an important effect in the moist tropical boundary layer. The temperature and moisture distributions above the trade inversion were specified from ATEX soundings while climatological distributions of ozone and carbon dioxide were assumed. The cooling rates in the boundary layer were calculated for 5 mb layers while for levels greater than 20 mb above the trade inversion the cooling rates were calculated for 50 mb increments.

The calculated heating rates as a function of pressure are shown in Fig. 6 for model I.1 and II.1. It should be noted that in spite of the linear functions of temperature and moisture used in the transfer calculations, the cooling rates exhibit fluctuations of $\approx .5°C\ day^{-1}$ over a 20 mb layer. These small-scale fluctuations may be at least partially due to the computational inaccuracies of the transfer calculation since for a 5 mb layer a variation of .3 Wm^{-2} results in a variation in the heating of $.5°C\ day^{-1}$. In this analysis it is desirable to obtain an average cooling rate for the mixed layer and the cloud layer and to further divide the cloud layer cooling into upper and lower cloud layer cooling. Since these layers are typically greater than 20 mb in thickness, the "noise" which appears in the cooling profiles should not significantly affect the cooling rates averaged over these layers.

The average heating rate from the inversion top to the surface is approximately the same for the two cooling rate profiles shown in

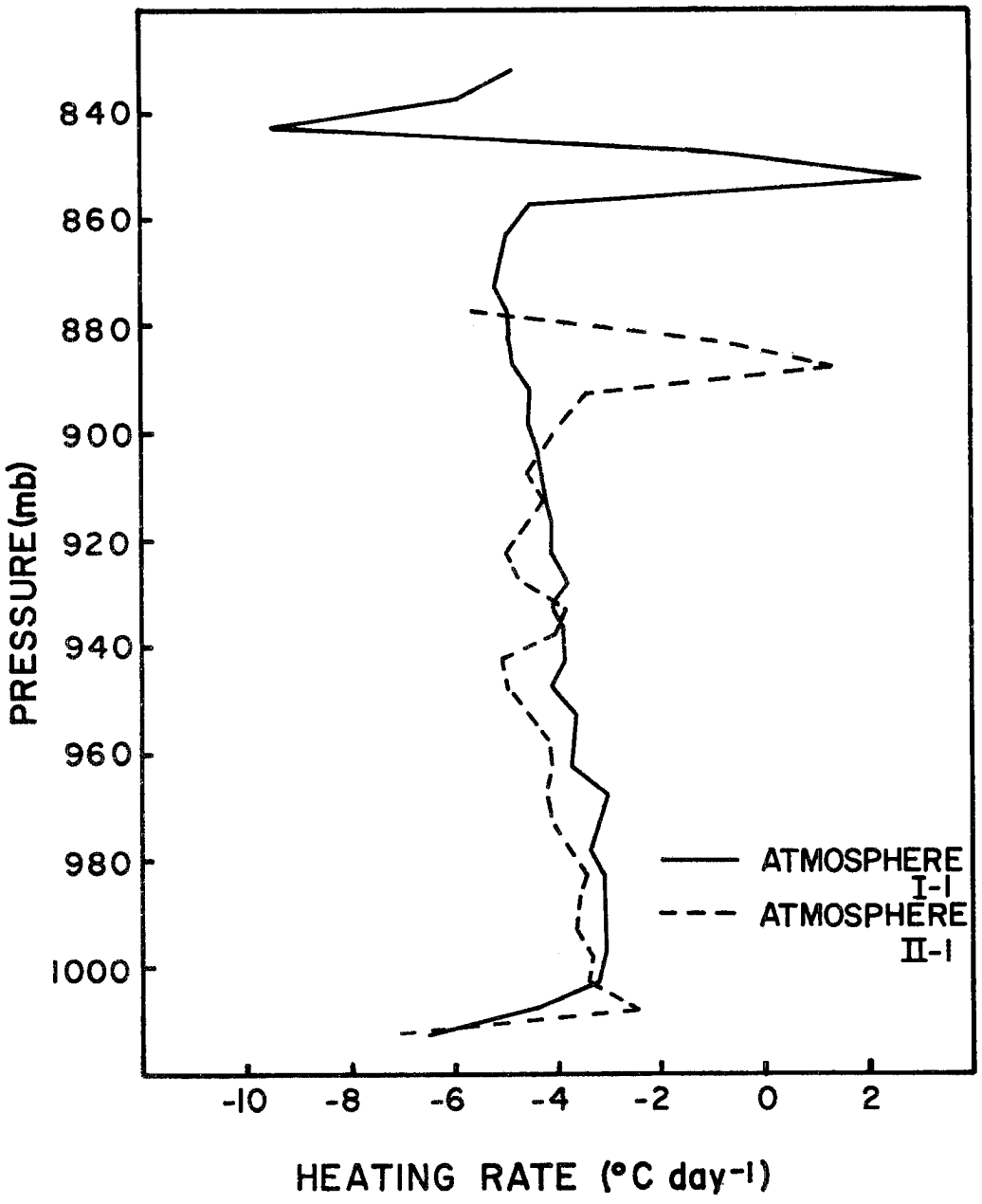

Figure 6. A comparison of longwave heating rates calculated for model atmosphere I and II.

Fig. 6. Similarly both profiles show the same qualitative features. The sharp discontinuity in the cooling rates at the trade inversion reflect the tendency of the radiation to weaken the inversion with relative warming below the inversion and cooling above the inversion. Staley (1965) noted a similar radiative effect for middle-tropospheric inversions. The average heating in the cloud layer is approximately the same for model I and II if the levels immediately below the inversion are ignored. For the shallower boundary layer, however, the infrared cooling tends to stabilize the cloud layer while the infrared cooling processes in the cloud layer of model I is a destabilizing process. The average subcloud layer cooling for model II is approximately 1°C day^{-1} greater than that for model I.

Heating rates calculated for the model atmospheres summarized in Table I were used to determine the variations in boundary layer heating. As stated above it is only necessary to determine average heating rates for the entire boundary layer, subcloud layer, cloud layer and top and bottom half of the cloud layer in order to specify the fluxes in the model. The cooling rates shown in Fig. 6, however, have large vertical variations near the trade inversion, the transition layer, and near the surface. The initial motivation for assuming an infinitesimally thin layer for the inversions at the top of the subcloud layer and at the top of the cloud layer was to eliminate the need to consider the physical details of these layers. Consequently, although the discontinuities in the radiative heating in the vicinity of the trade inversion extend approximately 5 mb below the inversion, these discontinuities are not included in the computation of the average cooling for the cloud layer. Similarly, the transition layer

and the 5 mb layer near the surface are not included in heating rates averaged over a particular layer.

A summary of the calculated heating averaged through the entire boundary layer, $(Q_L)_o^{CLR}$, is given in Table II for the model atmospheres described in Table I. $(Q_L)_o^{CLR}$ is defined as the mass averaged cloud layer heating, $(Q_L)_C^{CLR}$, and subcloud layer heating rate, $(Q_L)_M^{CLR}$, so that

$$(Q_L)_o^{CLR} = \frac{(Q_L)_C^{CLR}\ \delta\hat{p} + (Q_L)_M^{CLR}\ \hat{p}_B}{(\delta\hat{p} + \hat{p}_B)}$$

The values of $(Q_L)_o^{CLR}$ which are given in Table II are given as a function of the boundary layer precipitable water which is defined as

$$(\Delta u)_M = \frac{1}{\rho_w g} \int_0^{\hat{p}_I} \bar{q}\, d\hat{p}$$

where ρ_w is the density of water.

The results given in Table II show that $(Q_L)_o^{CLR}$ is virtually independent of boundary layer temperature and moisture variations. The average calculated heating rate is $\simeq -4.0°C\ day^{-1}$. As shown by Cox (1973) a significant portion of the boundary layer infrared cooling rate may be due to continuum absorption. Unfortunately, although relatively large cooling rates have been reported by Cox (1969) from radiometersonde measurements, the effect of continuum cooling has not been satisfactorily

MODEL ATMOSPHERE	$(\Delta\mu)_M$ (cm)	$(Q_L)_o^{CLR}$ (°C day^{-1})
I-0	2.06	-4.03
I-1	2.00	-4.04
I-2	1.94	-4.05
I-3	1.88	-4.04
II-0	1.58	-4.05
II-1	1.56	-4.05
II-2	1.54	-4.04
II-3	1.51	-4.04
IA-1	2.42	-4.46
IIA-1	1.61	-4.10
IIA-3	1.56	-4.11
IB-1	2.00	-4.20
IB-3	1.88	-4.18
IIB-1	1.56	-4.11
IIB-3	1.51	-4.11

TABLE II. The average boundary layer heating, $(Q_L)_o^{CLR}$, as a function of boundary layer precipitable water, $(\Delta u)_m$.

documented from measurements. In the model results given in Chapter V the sensitivity of the model to the specification of $(Q_L)_o^{CLR}$ will be determined since this cooling rate, as shown by Starr (1976), may also be sensitive to the cloud cover and to the quantity of moisture above the boundary layer. The important feature illustrated by the results given in Table II is that the average cooling rates calculated for the entire boundary layer are relatively insensitive to variations in the temperature and moisture structure of the boundary layer itself.

Although the longwave heating rates averaged through the entire boundary layer do not change significantly with the moisture variations, the vertical distribution of the cooling rates does change with the moisture variations. These variations are illustrated in Fig. 7 where heating rates calculated for model I with $\gamma_q = 0.0$ and $\gamma_q = -.05$ g kg^{-1} mb^{-1} are shown. These results show that the drier atmosphere results in the cooling maximum being displaced lower in the atmosphere so that the subcloud layer cooling increases as the cloud layer moisture decreases.

As the cloud layer becomes drier the radiative cooling tends to stabilize the layer while the more moist atmosphere results in a destabilization of the layer. Cox (1973) demonstrated a similar coupling of the radiative fluxes to the moisture distribution. His results indicated that this change in the vertical structure of the heating profile was due to the effect of continuum absorption. Cox (1973) showed that as the atmosphere becomes more moist the continuum absorption results in the maximum cooling being displaced higher in the atmosphere. This effect is also apparent in the heating rates calculated from the model atmospheres described above.

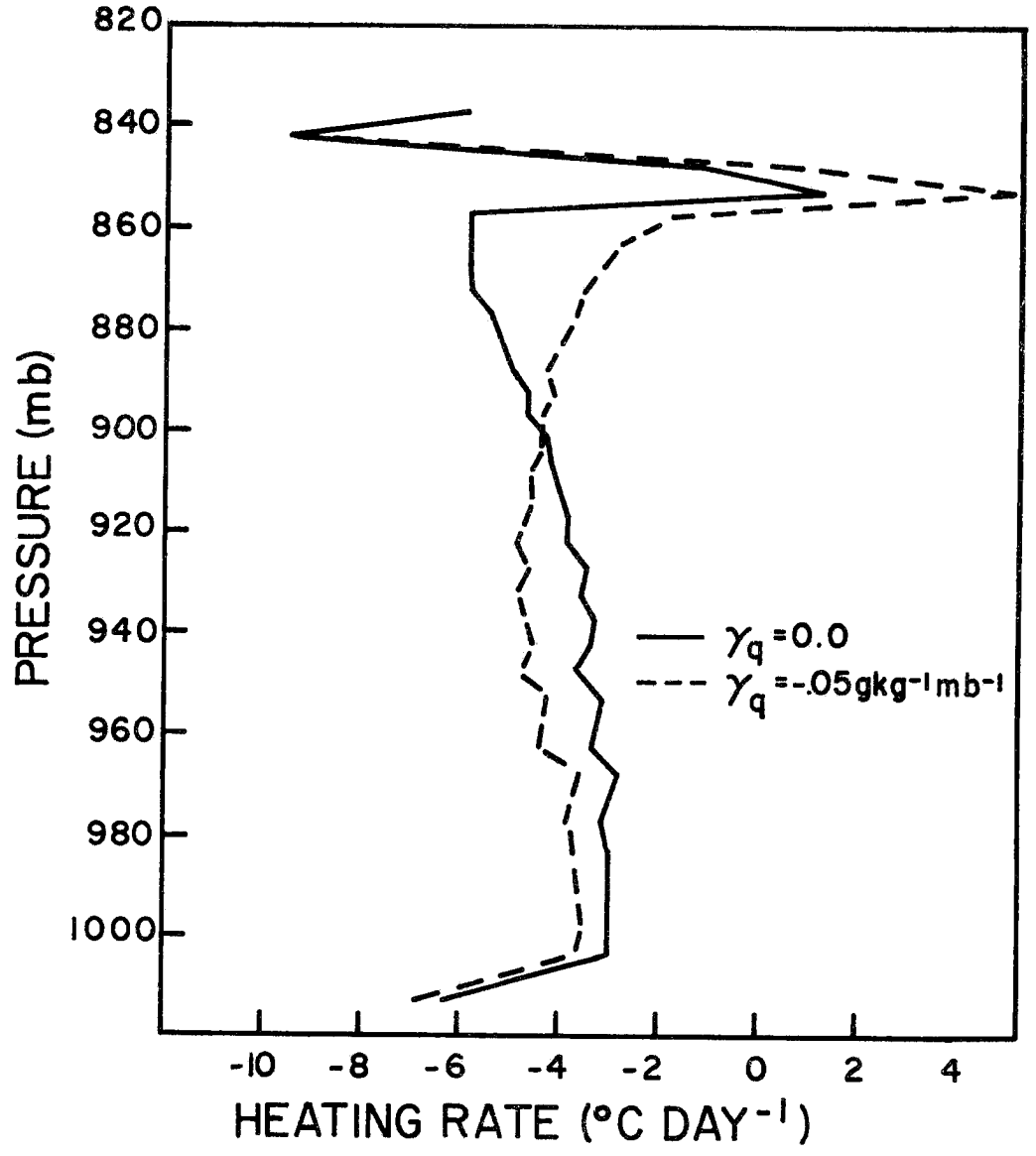

Figure 7. A comparison of longwave heating rates calculated with model atmosphere I temperature structure and a cloud layer lapse-rate of moisture of γ_q = 0 and γ_q = -.05 gkg^{-1} mb^{-1}.

The difference between the average cloud layer heating and the averaged mixed layer heating is shown in Fig. 8 as a function of the average cloud-layer moisture. These results show a nearly linear increase in the absolute value of the difference as the cloud layer moisture increases. For model I-1 which closely resembles the ATEX profiles this difference is $\simeq -1°C\ day^{-1}$. The calculations shown in Fig. 8 show that the effect of temperature is minimal in changing the difference between cloud layer and subcloud layer cooling.

The stabilizing-destabilizing effect in the cloud layer is a feature of the heating rates calculated for the model atmospheres. This effect may be represented as a difference between the radiative heating of the upper half of the cloud layer, $(Q_L)_{CT}^{CLR}$, and the lower half, $(Q_L)_{CB}^{CLR}$. This difference is shown in Fig. 9 as a function of q_A. These results clearly show a trend for destabilization as the cloud layer becomes more moist. This effect also depends on the temperature lapse rate with the destabilizing effect decreasing as the layer becomes more unstable.

The effect of the vertical detail in the heating rates will be evaluated in Chapter V. This will be accomplished by comparing results obtained by specifying the boundary layer cooling to be uniform within the layer to results obtained with the vertical variation described above. For this purpose the results shown in Fig. 8 and 9 are represented empirically as

$$(Q_L)_M^{CLR} = (Q_L)_C^{CLR} \quad -6.43 + .684\ q_A \qquad \text{(IV.1)}$$

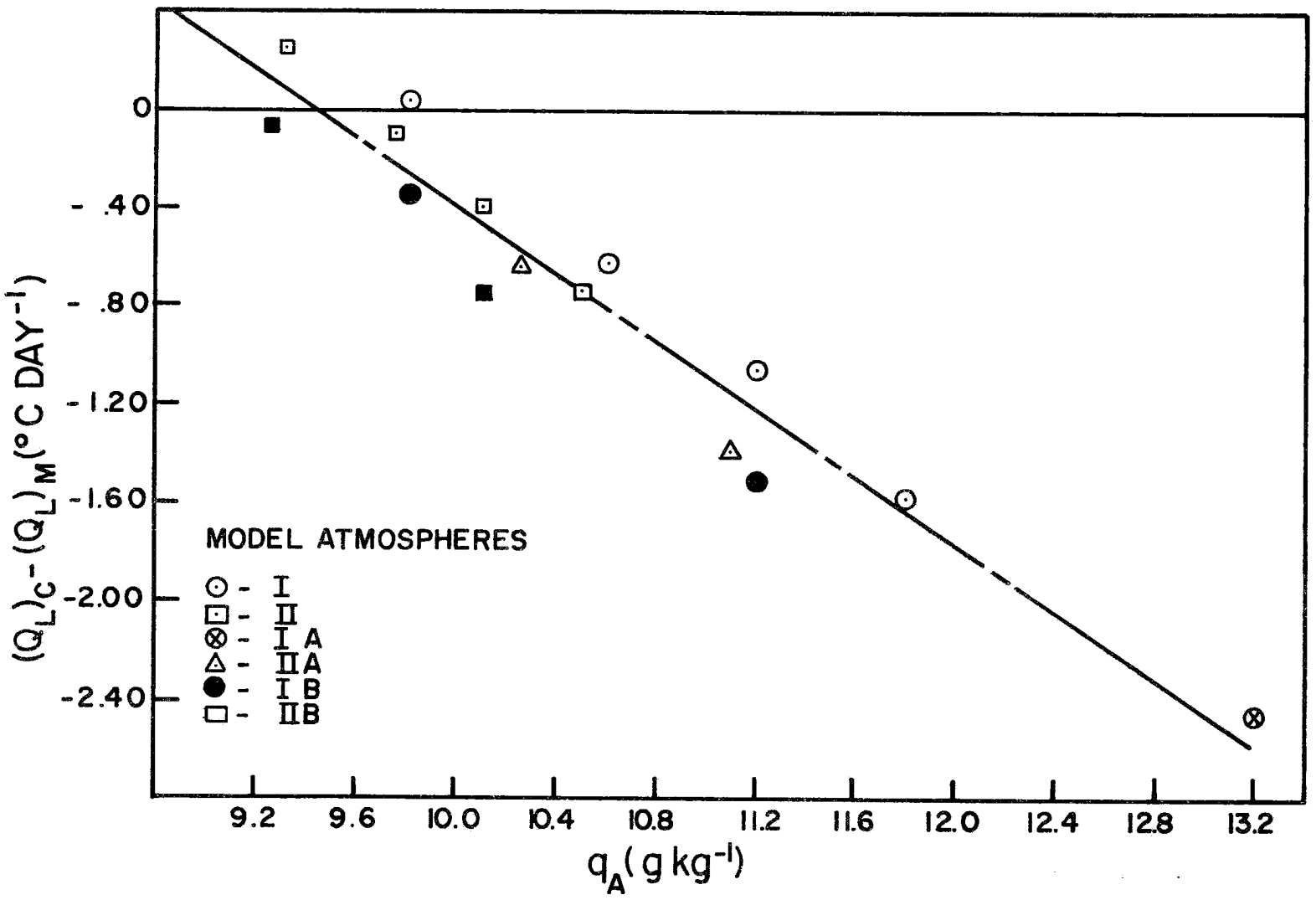

Figure 8. Difference between the calculated cloud and subcloud layer averaged longwave heating rates for various temperature and moisture distribution. See Table I for details on these distributions.

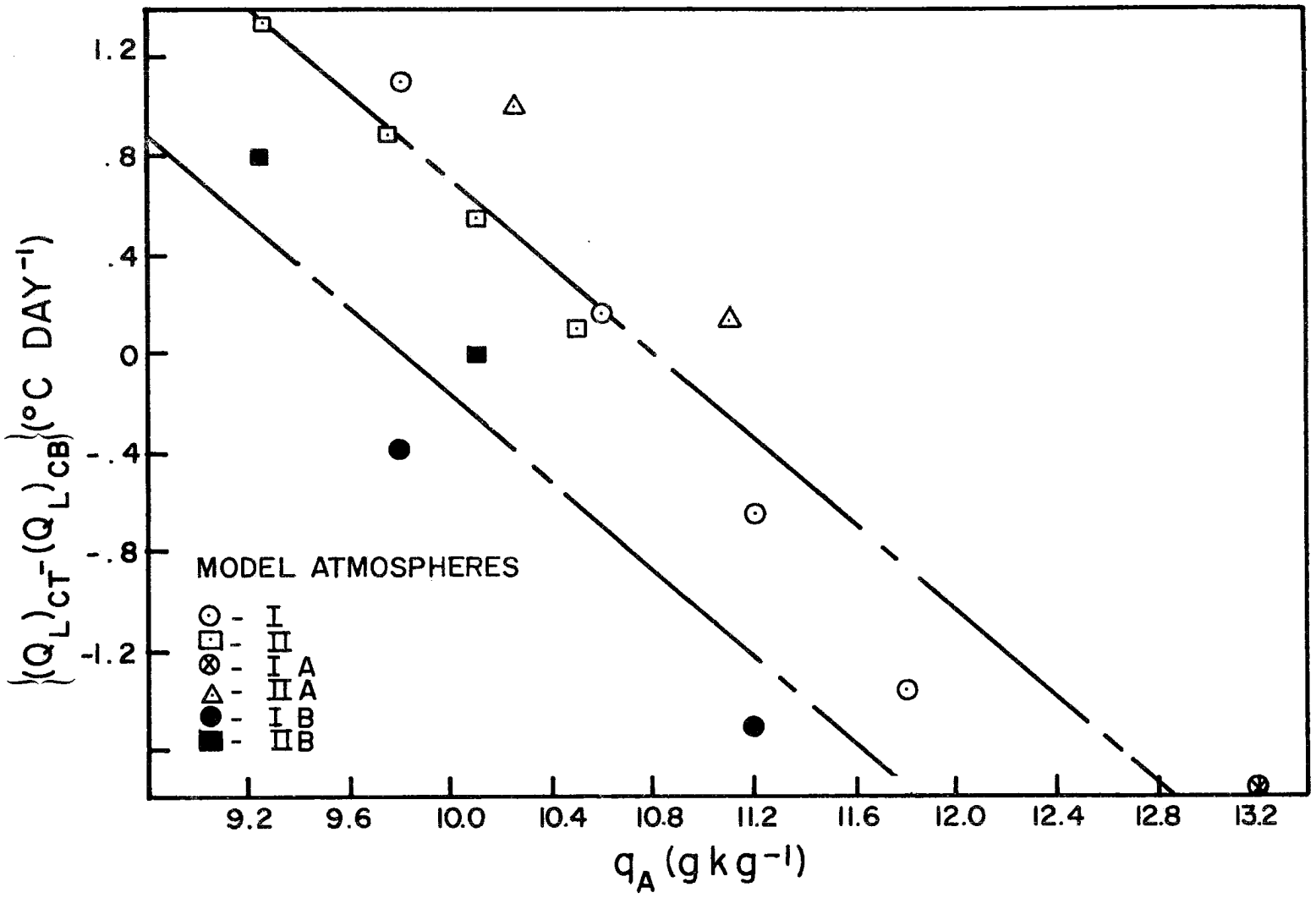

Figure 9. Difference between the calculated clear sky longwave heating rates averaged over the top and those averaged over the bottom of the cloud layer.

where q_A is given in g kg^{-1} and

$$(Q_L)_{CT}^{CLR} = (Q_L)_{CB}^{CLR} + 7.67 - 2.71 \times 10^2 \gamma_T - .88\, q_A \qquad \text{(IV.2)}$$

where γ_T is the lapse rate of T in °C mb^{-1}. The heating rates given by IV.1 and IV.2 are in °C d^{-1}.

The longwave cooling within clouds was determined by considering a horizontally infinite cloud. The effect due to all cloud elements is simply assumed to be proportional to the fractional area, σ_R, covered by these clouds. The basic method of computing the in cloud fluxes is similar to the method described by Griffith (1977). In this method the broadband emissivity, ε_c, within the cloud is formulated in the exponential form suggested by Paltridge (1974). This form is given as

$$\varepsilon_c(h) = 1 - \exp\,[-a_o w(h)] \qquad \text{(IV.3)}$$

where h is the distance from the cloud boundary to some point within the cloud and a_o is interpreted as a mass absorption coefficient. The parameter w in (IV.3) is the liquid water path and is defined as

$$w = \int_o^h \text{LWC}\; dz$$

where LWC is the liquid water content of the cloud and may be a function of height. The emissivity as given by (IV.3) is incorporated into the clear sky radiative transfer calculation described by Cox (1973). The details of this calculation are given by Griffith (1977). A similar method is described by Feigel'son (1973).

The use of (IV.3) in the transfer calculation requires that the LWC and a_o be specified. In the calculations presented below a_o is assumed to be a constant given as 500 $g^{-1}cm^2$. The aircraft measurements presented by Paltridge (1974) indicate that $a_o \simeq 300$ cm^2g^{-1} with an uncertainty of approximately the same magnitude. The theoretical calculations of in-cloud absorption given by Yamamoto et al., (1970), however, would suggest an a_o value significantly larger than those given by Paltridge. Although the choice of $a_o = 500$ $g^{-1}cm^2$ is somewhat arbitrary, it is important to note that a precise knowledge of the liquid water content of the active and dying clouds which are being considered is not available. Since a_o and w appear as a product in the expression for the emissivity, it is arbitrary to which parameter is held constant in determining the sensitivity of the calculated fluxes to these parameters.

In the calculations presented below the liquid water content of the clouds is assumed to increase linearly with height with a liquid water content of zero at cloud base. Above the inversion base the liquid water content decreases linearly to a value of zero at the top of the inversion. Longwave fluxes were calculated for cloud models with the temperature and water vapor structure specified for model I and with a LWC averaged through the cloud layer of .5 gm^{-3} and .25 gm^{-3}. A third calculation was made with model II structure and an average LWC of

.25 gm^{-3}. The net longwave flux for model atmosphere I with $\overline{LWC}$ = .5 gm^{-3} and $\overline{LWC}$ = .25 gm^{-3} are shown in Fig. 10. (Warner (1955) measured the water content of small cumulus to be ≃ .5 gm^{-3}.) These results show that the calculated fluxes are relatively insensitive to the specification of the liquid water content. One could similarly assume that the calculation is equally insensitive to the specification of a_o. Since the cooling rate is proportional to the vertical derivative of the net flux it is apparent that the most significant feature of the fluxes given in Fig. 10 is the strong cooling that occurs at cloud top. Nearly 90% of the cloud layer cooling occurs in the top 10 mb of the cloud layer. Near the cloud base there is slight warming, while in the subcloud layer the infrared heating average through the layer is almost zero.

The average cooling for the entire boundary layer from the inversion top to 5 mb above the surface for the three model atmospheres considered is given in Table III. $(Q_L)_o^{CLD}$ as shown in Table III is not extremely sensitive to the model structure that is assumed. The cooling for model II is slightly enhanced since the cloud top in this case is at a slightly warmer temperature than the cloud considered for model I. It is significant to note that the average boundary layer cooling is approximately equivalent to the average cooling calculated for the clear sky atmospheres. The cloud and subcloud layer heating rates, however, are significantly different than those calculated for the clear sky. In the boundary layer the average heating below the inversion is nearly negligible. In the cloud layer the top 10 mb of the layer are assumed to be a part of the inversion layer. With this assumption the cloud layer heating rate is ≃ 1.4°C day^{-1}. The magnitude of the cloud layer heating,

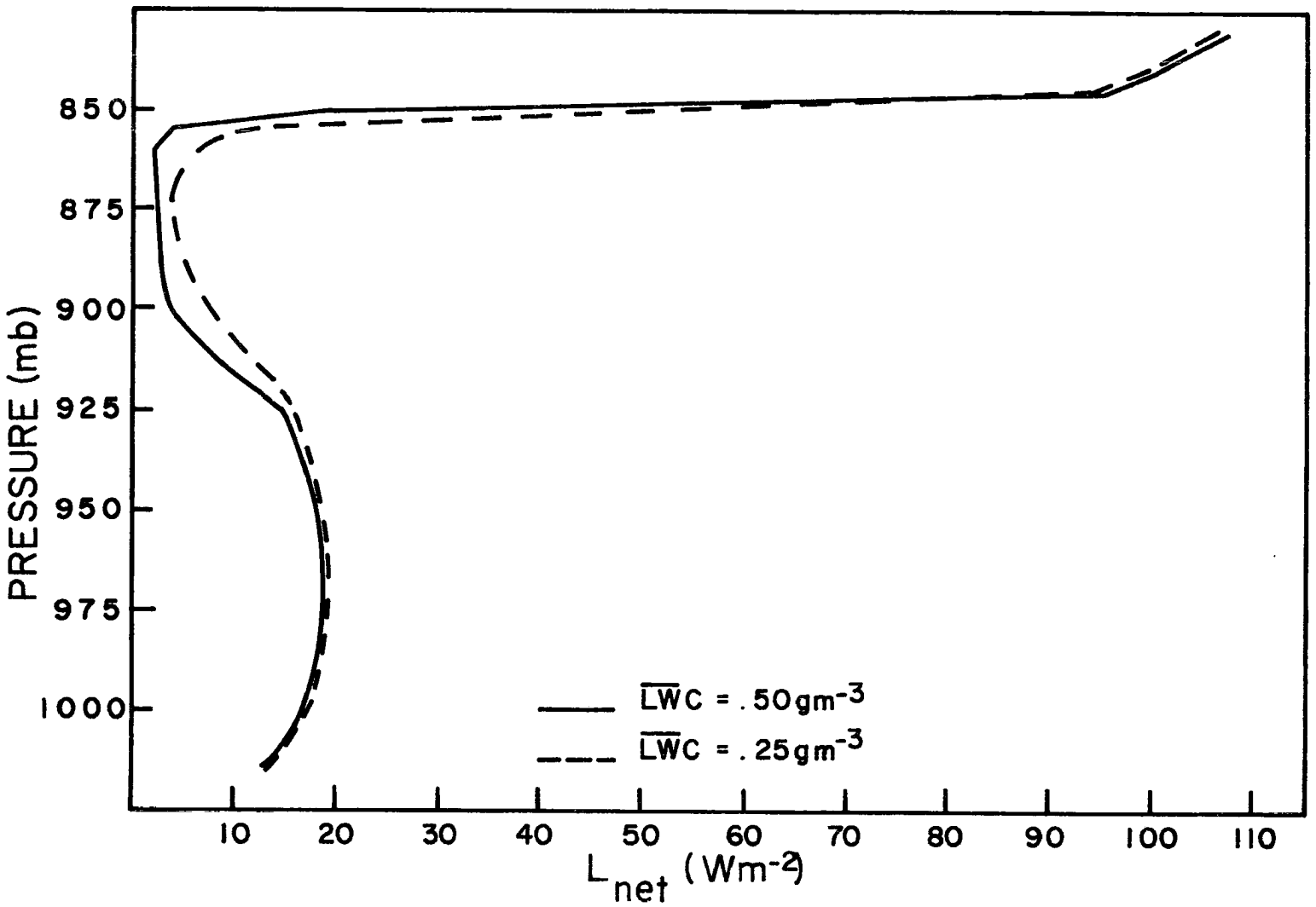

Figure 10. The net longwave fluxes calculated for horizontally infinite clouds having mean liquid water contents of .5 and .25 gm^{-3} and model I temperature structure.

CLOUD DESCRIPTION	$(Q_L)_o^{CLR}$ (°C day^{-1})	$(Q_L)_C^{CLD}$ (°C day^{-1})	$(Q_L)_M^{CLD}$ (°C day^{-1})
ATMOS I $\overline{LWC}$-.5gm^{-3}	-4.11	1.59	-.08
ATMOS I $\overline{LWC}$-.25gm^{-3}	-4.03	1.11	.21
ATMOS II $\overline{LWC}$-.25gm^{-3}	-4.59	1.41	-.25

TABLE III. Layer averaged cooling rates for various model atmospheres and model clouds.

however, is very sensitive to the specification of the inversion base since the net flux is nearly discontinuous at this level. The results shown in Fig. 10 also show a slight destabilization within the cloud itself due principally to the warming at cloud base. No attempt will be made in this paper to parameterize this in-cloud destabilization.

A principal characteristic of the calculated infrared heating rates given above is the relative insensitivity of the heating averaged through the boundary layer to fluctuations in temperature, moisture and cloudiness. However, the vertical distribution of the heating varies significantly with the amount of boundary layer cloudiness. For clear sky conditions the cooling in the boundary layer is distributed nearly uniformly through the boundary layer. For a cloudy atmosphere, however, the entire cooling is confined to a very thin layer at cloud top. Aircraft measurements of infrared radiation made during the GARP[1] Atlantic Tropical Experiment (GATE), 1974, were evaluated in order to demonstrate the dependence of boundary layer infrared heating rates on the amount of boundary layer cloudiness. The particular data analyzed was obtained from an NCAR Sabreliner flight made on September 11, 1974 approximately 200 km northwest of Dakar, Senegal. During this flight, measurements were made in a region which was characterized by clear-sky conditions over the northern 40 km of the flight path and 10-30% coverage by shallow cumulus over the southern 40 km of the path. The infrared measurements made during this flight were obtained with upward and downward facing Eppley pyrgeometers. A description of these instruments and procedures for maximizing their performance is given by Albrecht et al., (1974) and Albrecht and Cox (1977). The method used to log the data obtained during

[1]Global Atmospheric Research Program

this flight and the data reduction procedures are outlined by Albrecht and Cox (1976).

The flight pattern in the boundary layer consisted of constant pressure level legs at ≈ 1012, 978, 928, and 846 mb. In the region of trade cumulus the 978 mb level was slightly below cloud base while the 928 mb level was just at cloud top. The data collected during the boundary layer portion of this flight were stratified into data collected in clear sky conditions and those obtained with a 10-30% coverage by trade cumulus. Data collected where cloud cover was less than 10% but greater than 0 were not included in the analysis. Observer notes, a side-looking time-lapse camera, and the measured upward and downward shortwave irradiance were used to subjectively make the stratification described above. The stratification as a function of time is given in Table IV. The legs at 928 and 978 mb were longer and were duplicated resulting in greater amounts of data collected at the 846 and 1012 mb levels than the other two levels. In both the clear and partly cloudy cases the upper boundary of the boundary layer was defined by a temperature and moisture discontinuity at ≈ 930 mb.

The upward and downward irradiance averaged for the times given in Table III are shown in Fig. 11 for the clear sky case and in Fig. 12 for the trade cumulus case. It is interesting to note that the upward irradiance does not change significantly between the clear and partly cloudy case. Above the cloud the upward irradiance in the clear case is slightly greater than that obtained for the cloud case. The downward irradiance at the surface and at cloud base, however, is significantly larger for the cloud case than the clear case. Physically one would expect this result since the clouds are nearly "black" in the infrared and have an

Pressure (mb)	Clear	Trade Cu 10-30%
846	12:24:00 - 12:25:59	12:27:00 - 12:28:59
928	12:35:00 - 12:35:59	12:31:00 - 12:33:59
	12:59:00 - 13:05:59	13:10:00 - 13:12:59
978	12:52:00 - 12:55:59	13:14:30 - 13:17:59
1012	12:48:00 - 12:49:59	12:44:30 - 12:46:59

TABLE IV. Data analyzed for clear and 10-30% trade cumulus conditions for September 11, 1974 Sabreliner Flight.

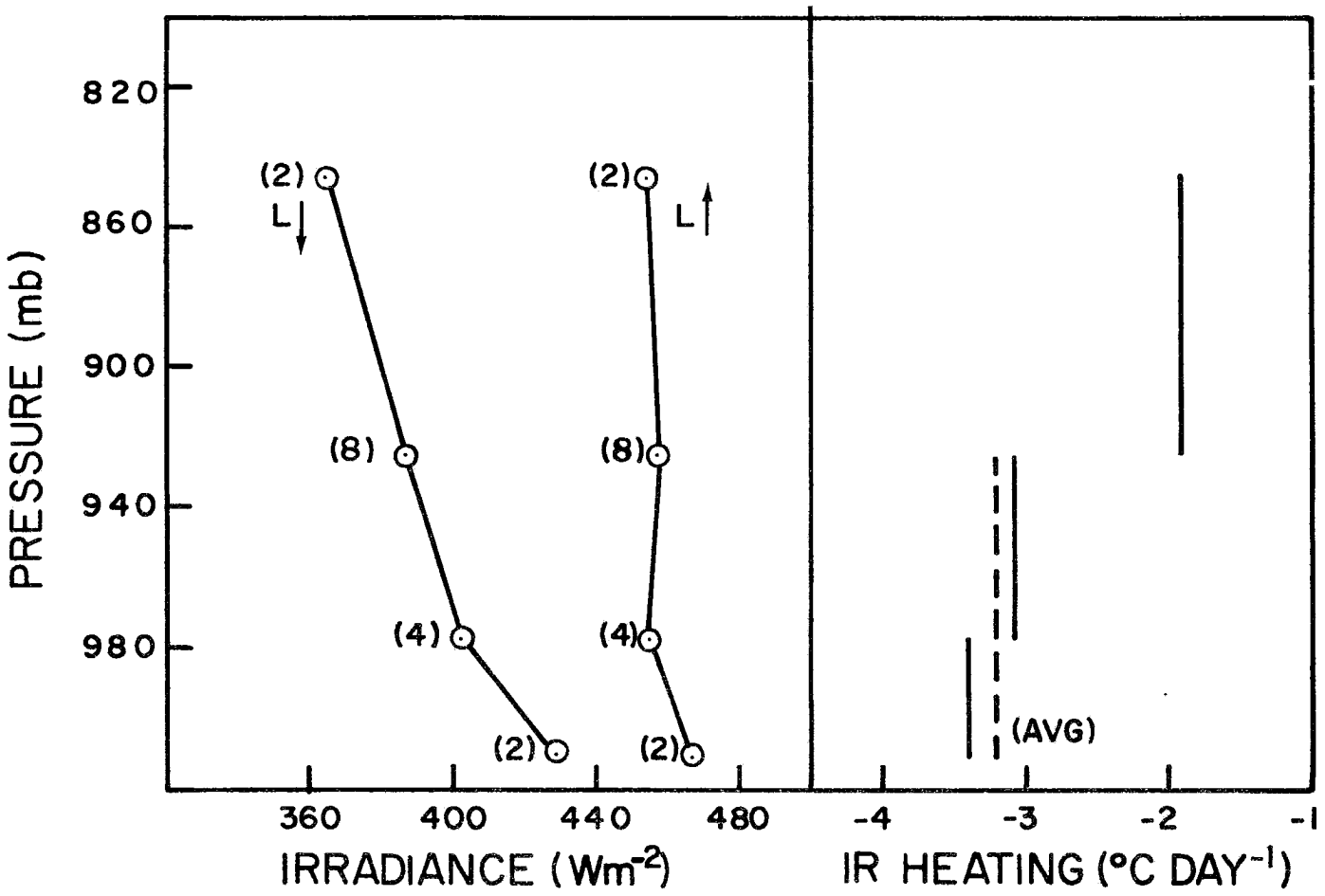

Figure 11. Observed upward and downward longwave fluxes and heating rates calculated from these fluxes for clear sky conditions. Measurements were made from the NCAR Sabreliner, September 11, 1974. The numbers in the brackets indicate the number of minutes of data used to calculate the fluxes at a given level.

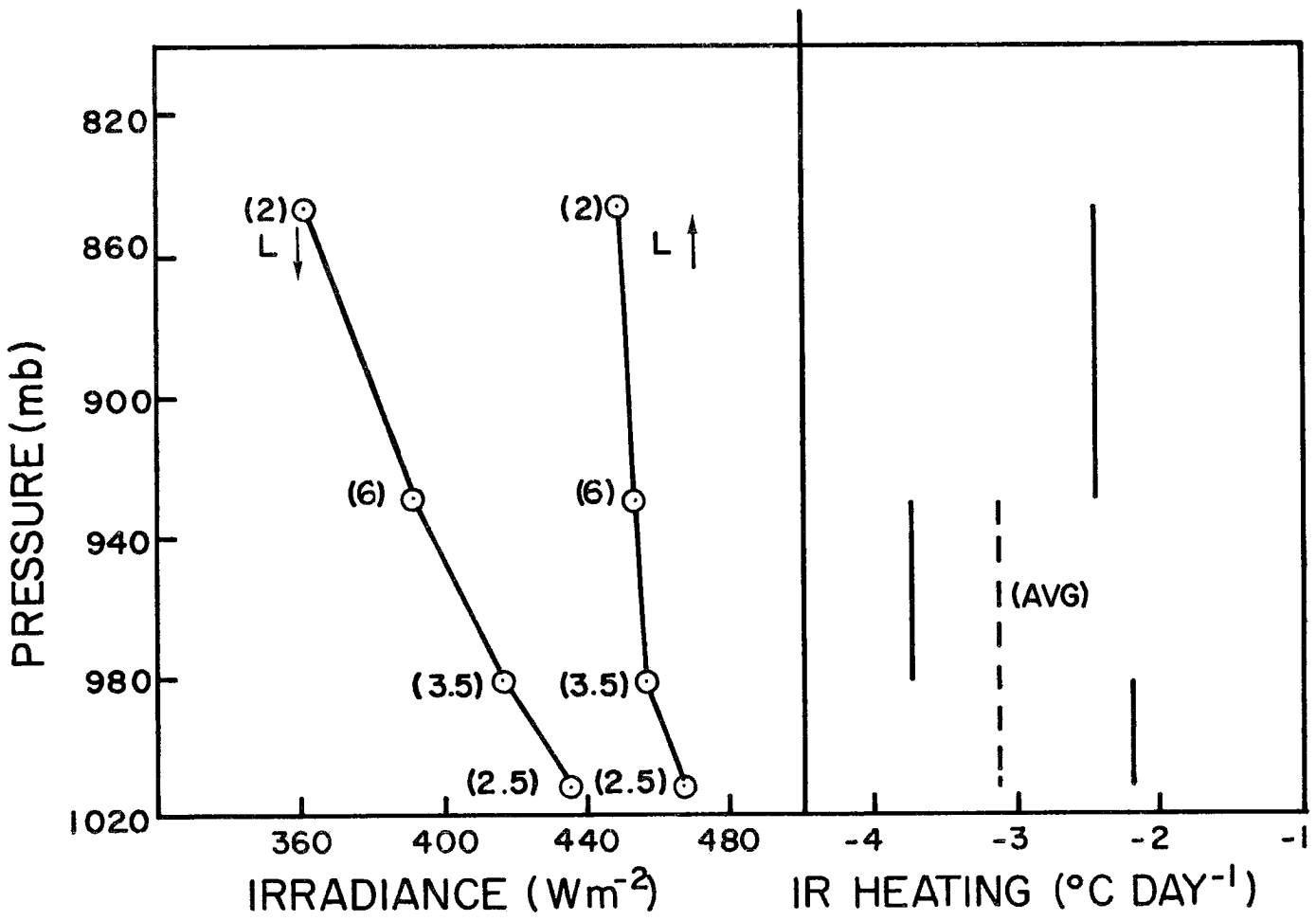

Figure 12. Same as Figure 11 but for a cloud cover of 10-30% trade cumulus.

equivalent blackbody temperature which is much higher than that of the clear sky constituents. The downward irradiance at cloud top in the cloud case is also slightly greater than the clear case due to the aircraft penetration of the tops of a few cumulus at this level.

The cooling rates calculated for each layer are also shown in Fig. 11 and 12 and reflect the qualitative description of the fluxes given above. In the clear-sky case the infrared cooling is approximately uniform throughout the boundary layer with the average being $\simeq 3.20°C\ day^{-1}$. In the cloudy case, however, the subcloud-layer cooling is suppressed and the cloud layer cooling is enhanced which is consistent with the calculated fluxes presented above. Furthermore, the average cooling through the boundary layer is approximately that obtained for the clear sky case. The cooling in the layer above the cloud layer in the cloudy case is slightly greater than that of the clear sky case. The difference in the cooling noted in this layer may be at least partially due to the fact that a few clouds extended above the 920 mb flight level. Unfortunately, the measurements described here are not suitable to verify the detailed cooling rate structure which exists in the cloud layer itself.

B. Shortwave Heating Rates

The clear sky boundary layer heating due to the absorption of solar radiation by water vapor, carbon dioxide, and ozone is estimated from a broadband solar irradiance calculation. The computational procedure and absorptivity values used in the model are basically those outlined by Manabe and Möller (1961) and Manabe and Strickler (1964). A complete description of the shortwave calculation used is given by Starr (1976).

The temperature and moisture profiles described for model I and II above were used in the shortwave calculation. The heating rate averaged through the boundary layer due to shortwave absorption is shown in Fig. 13 for model atmosphere I and II as a function of time. The difference between these calculated fluxes is less than .1°C day^{-1} at all times. Additional calculations made with γ_q = -.05 gkg^{-1} indicated the same insensitivity of the calculated heating rates to variations in the moisture distribution. The vertically averaged boundary layer heating shown in Fig. 13 averaged over a 24 hr period is ≃ .8°C day^{-1}.

The solar heating does not vary significantly in the vertical. For the model I calculation, for example, the cloud layer heating $(Q_s)_C^{CLR}$, averaged over the entire day is ≃ .90°C day^{-1} while the mixed layer heating $(Q_s)_M^{CLR}$ is ≃ .70°C day^{-1}. The difference in the heating rate of the top half of the cloud layer and the bottom half is ≃ .20°C day^{-1} which represents a slight stabilization. Since the vertical variations in the solar heating are small, they will be neglected in the model calculations given below.

In the numerical results presented below for a diurnally varying shortwave heating the results shown in Fig. 13 are represented as

$$(Q_s)_o^{CLR} = \max \begin{Bmatrix} -8.92 + 1.92\ t - .08t^2 \\ 0 \end{Bmatrix} \qquad \text{(IV.4)}$$

where $(Q_s)_o^{CLR}$ is in °C day^{-1} and t is local time in hours.

There is some evidence that aerosols may result in larger heating rates than those calculated for a simple gaseous atmosphere (Reynolds

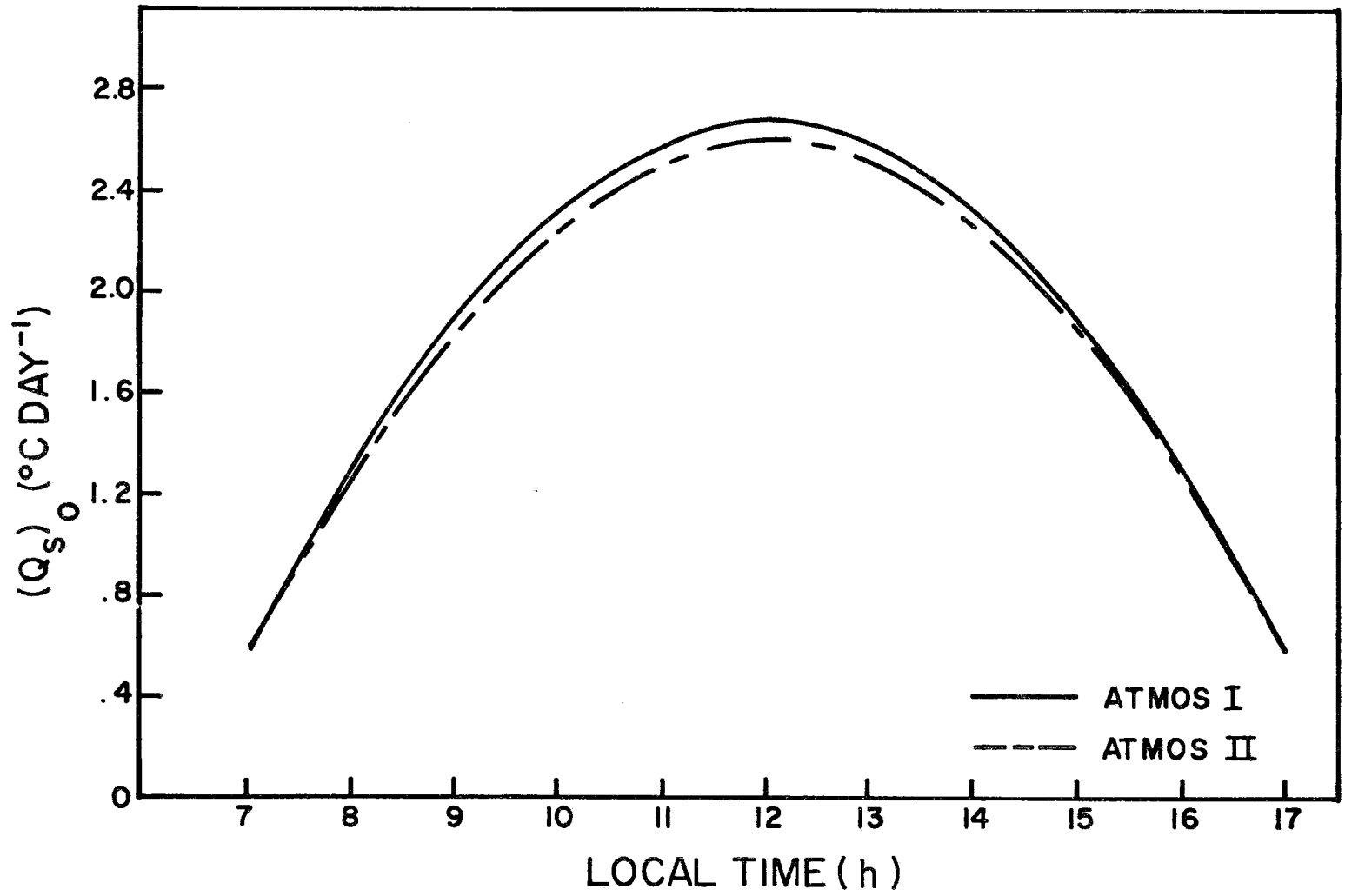

Figure 13. Calculated clear sky solar heating as a function of time for model atmosphere I and II.

et al., 1975; Kondratyev et al., 1976). No attempt is made here, however, to quantify this effect. The sensitivity of the predicted boundary layer structure to the specification of the radiative heating will be determined in Chapter V.

The absorption of solar radiation by clouds is a process which has not been satisfactorily quantified. There are very few direct measurements of the solar absorption by clouds and those measurements do not agree with theoretical calculations. Reynolds et al. (1975) used radiation data collected during the Barbados Oceanographic and Meteorological Experiment (BOMEX), 1969, from single and multiple aircraft missions to calculate the solar absorption by various cloud types. For stratocumulus clouds they found the absorption to be 12-36%. The absorptivity of clouds has also been computed theoretically for clouds of infinite horizontal extent. Liou (1976) calculated the solar absorption for clouds having the cloud drop size distribution observed for fair weather cumulus. His results show an absorption of 6-9% depending on the solar elevation. Twomey (1976) found the absorption calculated for clouds having maritime characteristics to be 9-17%. Both Liou and Twomey have suggested that the absorption of solar radiation by aerosols may account for the large absorption reported by Reynolds.

For simplicity it is assumed here that the solar absorption in the boundary layer is the same for both cloud and clear conditions. In the cloud case, however, this absorption occurs in a thin layer at cloud top while in the clear case it is uniformly distributed. This assumption results in an absorption which is not significantly different than that predicted by Liou (1976). In the results presented below, unless

specifically noted otherwise, the solar heating will be included as a value integrated over the entire day.

C. Parameterization for Numerical Experiments

In the numerical results given in Chapter V, the longwave cooling will be parameterized using two different schemes. The first scheme, designated as RADI, assumes that the radiation has no effect on the stability of the layer. The second scheme, designated as RADII, represents the stability changes due to radiation in terms of the moisture and temperature lapse rates as given by (IV.1) and (IV.2). In the next chapter the boundary layer structure predicted using RADI will be compared with that predicted using RADII parameterization.

In the RADI longwave parameterization, the longwave cooling averaged over the depth of the boundary layer for clear sky conditions is specified as a constant, $(Q_L)_o^{CLR}$. In the clear regions the cooling is uniform throughout the boundary layer so that $(Q_L)_C^{CLR} = (Q_L)_M^{CLR} = (Q_L)_{CT}^{CLR} = (Q_L)_{CE}^{CLR} = (Q_L)_o^{CLR}$. In the cloudy regions it is also assumed that the cooling averaged through the depth of the boundary layer is constant and equal to the clear sky cooling (i.e. $(Q_L)_o^{CLD} = (Q_L)_o^{CLR}$). The cooling is, however, confined to a thin layer at cloud top so that there is no cooling below the inversion, which gives $(Q_L)_C^{CLD} = (Q_L)_M^{CLD} = (Q_L)_{CT}^{CLD} = (Q_L)_{CE}^{CLD} = 0$.

The RADII parameterization is identical to RADI except that clear sky cooling rates are not distributed uniformly throughout the boundary layer. In this scheme, the cloud layer and subcloud layer cooling rates in $^{\circ}C\,c^{-1}$ are given from (IV.1) and (IV.2) as

$$(Q_L)_C^{CLR} = (Q_L)_O^{CLR} + (6.43 - 6.84 \times 10^3 \, q_A) \frac{\hat{p}_B}{\hat{p}_I} \qquad \text{(IV.5)}$$

and $$(Q_L)_M^{CLR} = (Q_L)_C^{CLR} - 6.43 + 6.84 \times 10^3 \, q_A \qquad \text{(IV.6)}$$

The difference between the cooling of the top and bottom half of the cloud layer is given as

$$(Q_L)_{CT}^{CLR} - (Q_L)_{CB}^{CLR} = 7.67 - 2.71 \times 10^2 \, \gamma_T - .88 \times 10^3 \, q_A \qquad \text{(IV.7)}$$

where γ_T is given in °C mb^{-1}.

In the results presented below the clear sky shortwave heating rates (the average over a day) are specified to be constant and uniform in the vertical. If the heating rate averaged through the boundary layer is specified to be $(Q_s)_o^{CLR}$, the heating rates below the inversion may be written as $(Q_s)_M^{CLR} = (Q_s)_C^{CLR} = (Q_s)_{CT}^{CLR} = (Q_s)_{CB}^{CLR} = (Q_s)_o^{CLR}$. In the cloudy regions the average heating, $(Q_s)_o^{CLD}$, is assumed to be constant and equal to that of the clear sky heating. There is, however, no heating below the thin inversion layer so that $(Q_s)_M^{CLD} = (Q_s)_C^{CLD} = (Q_s)_{CB}^{CLD} = (Q_s)_{CT}^{CLD} = 0$. The same parameterization is used if a diurnal shortwave heating is considered although in this case

$$(Q_s)_o^{CLR} = (Q_s)_o^{CLD} = \max \begin{Bmatrix} -8.92 + 1.92\ t - .08t^2 \\ 0 \end{Bmatrix} \qquad \text{(IV.8)}$$

where t is local time in hours and the heating rate is in °C day^{-1}.

The budget equations derived in Chapter II express the time rate of change of the boundary layer structure in terms of the radiative fluxes. These fluxes are easily obtained from the heating rates since the heating rates are the derivatives of the fluxes. Using this procedure the fluxes at the various levels may be expressed in terms of the visible cloud cover, σ_R, and the heating rates described above as

$$(F_R)_o = (F_R)_{I+} + \frac{c_p}{g} [(1-\sigma_R)\ (Q_R)_o^{CLR} + \sigma_R\ (Q_R)_o^{CLD}]\ \hat{p}_I \qquad \text{(IV.9)}$$

$$(F_R)_B = (F_R)_{I+} + \frac{c_p}{g} [(1-\sigma_R)\ (Q_R)_o^{CLR} + \sigma_R\ (Q_R)_o^{CLD}]\ \hat{p}_I$$

$$- \frac{c_p}{g} [(1-\sigma_R)\ (Q_R)_M^{CLR} + \sigma_R\ (Q_R)_M^{CLD}]\ \hat{p}_B \qquad \text{(IV.10)}$$

$$(F_R)_A = \frac{c_p}{g} \left\{ [(Q_R)_{CT}^{CLR} - (Q_R)_{CB}^{CLR}]\ (1-\sigma_R) + [(Q_R)_{CT}^{CLD} \right.$$

$$\left. - (Q_R)_{CB}^{CLR}]\ \sigma_R \right\} \frac{\delta\hat{p}}{4.0} + \frac{[(F_R)_{I-} + (F_R)_B]}{2.0} \qquad \text{(IV.11)}$$

$$(F_R)_{I-} = (F_R)_{I+} + \frac{c_p}{g}\sigma_R(Q_R)_0^{CLD}\,\hat{p}_I$$

$$- \frac{c_p}{g}\sigma_R\left[(Q_R)_M^{CLD}\,\hat{p}_B + (Q_R)_C^{CLD}\,\delta\hat{p}\right] \qquad \text{(IV.12)}$$

where the specification of $(F_R)_{I+}$ is arbitrary and $(Q_R)_o^{CLR} = (Q_L)_o^{CLR} + (Q_S)_o^{CLR}$, etc. A complete derivation of (IV.9) - (IV.12) is given in Appendix E.

C. Summary

The results presented above demonstrate a remarkable variation of the vertical structure of the boundary layer radiative heating rates with the amount of cloudiness. For a cloud-free boundary layer, for example, the longwave cooling is distributed rather uniformly within the boundary layer. For a completely cloudy situation the cooling is confined to a thin layer near cloud top. The cooling averaged over the entire boundary layer, however, does not vary significantly with variations of temperature, moisture or cloudiness within the boundary layer.

The results given above show some variation in the structure of the heating below the inversion. In the clear sky case a coupling of the radiative fluxes to the moisture distribution is noted. These results show that the radiative processes may either stabilize or destabilize the cloud layer depending on the moisture distribution. As illustrated by Cox (1973), this effect is due primarily to the continuum cooling. Unfortunately, the stabilizing-destabilizing processes predicted by the calculations presented above are difficult to verify experimentally.

Consequently, as stated previously, the approach that is adopted here is to determine the sensitivity of the structure predicted by the boundary layer model to specified heating rate profiles. Using this approach, the importance of the various radiative processes may be evaluated.

V. MODEL RESULTS

In this chapter the convective and radiative fluxes formulated in Chapter III and IV are combined with the predictive equations derived in Chapter II. The resulting equations are integrated numerically to determine the boundary-layer structure as a function of time. This procedure is shown schematically in Fig. 14. The various assumptions used to specify the convective and radiative fluxes are summarized in this figure. This organization of the model is similar to the more general depiction shown in Fig. 3 of the interaction of the various processes. In the numerical results presented below, however, the direct interaction between convective and radiative processes will not be considered. Consequently, visible cloud cover will be specified rather than determined as a function of other model parameters.

A summary of unknowns, specified physical parameters, and specified closure parameters is given in Table V. The equations which are used to determine the model unknowns are given in Tables VI, VII, and VIII. The predictive equations derived in Chapter II are summarized in Table VI and express the time variation of the boundary layer structure in terms of the convective and radiative fluxes. These fluxes, which are defined in Chapter III and IV and summarized in Tables VII and VIII, are formulated in terms of the large-scale thermodynamic structure and specified parameters. With this specification of the fluxes the predictive equations shown in Table VI may be integrated numerically. In the model results given in this paper a fourth order Runge-Kutta scheme (Conte, 1965) is used to solve the first order differential equations shown in Table VI. The details of this numerical method are given in Appendix F.

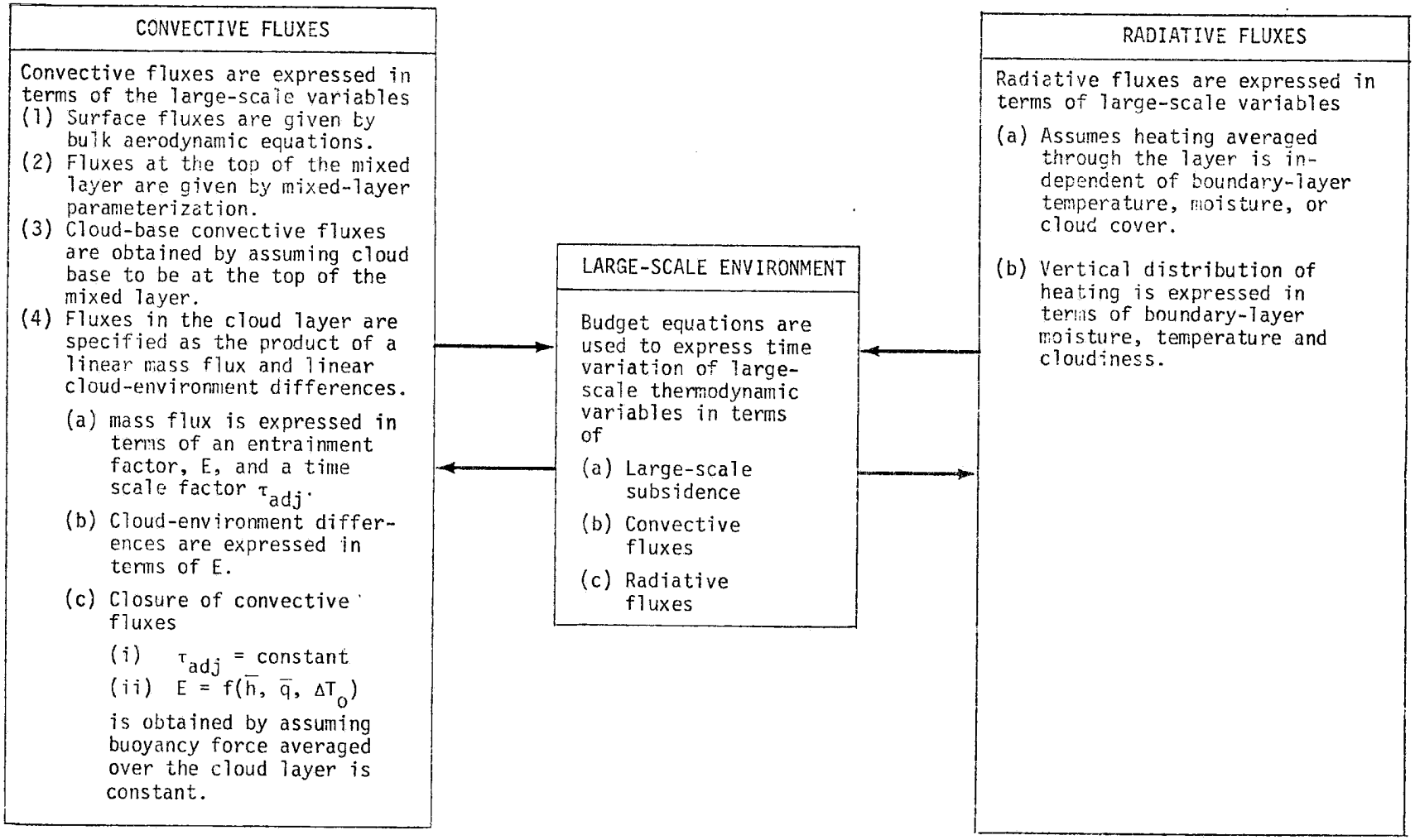

Figure 14. A schematic of the computational structure of the model.

Unknowns	Physical Parameters	Closure Parameters
q_M, h_M, q_A, h_A,	T_o, V_o, $\overline{D}$, σ_R, $q(\hat{p})$, $h(\hat{p})$,	C_T, C_q, k, δq,
γ_q, γ_h, $\hat{p}_B$, $\hat{p}_I$,	$(Q_L)_o^{CLR}$, $(Q_L)_o^{CLD}$, $(Q_s)_o^{CLR}$,	τ_{adj}, ΔT_o
$(F_q)_o$, $(F_h)_o$, $(F_R)_o$,	$(Q_s)_o^{CLD}$	
$(F_q)_{B-}$, $(F_h)_{B-}$, $(F_R)_B$,		
$(F_{q+\ell})_{B+}$, $(F_h)_{B+}$,		
$(F_{q+\ell})_A$, $(F_h)_A$, $(F_R)_A$,		
$(F_{q+\ell})_{I-}$, $(F_h)_{I-}$,		
$(F_R)_{I-}$, $(F_R)_{I+}$		

Table V. A summary of unknowns, specified physical parameters, and specified closure parameters used in the model.

$$\frac{\partial h_M}{\partial t} = -g\left[(F_h)_{B-} - (F_h)_o\right]/\hat{p}_B - g\left[(F_R)_B - (F_R)_o\right]/\hat{p}_B$$

$$\frac{\partial q_M}{\partial t} = -g\left[(F_q)_{B-} - (F_q)_o\right]/\hat{p}_B$$

$$\frac{\partial \hat{p}_B}{\partial t} = \hat{\omega}_B + g\left[(F_h)_{B+} - (F_h)_{B-}\right]/(\Delta h)_I$$

$$\frac{\partial \hat{p}_I}{\partial t} = \hat{\omega}_I - g(F_h)_I/(\Delta h)_I + g\left[(F_R)_{I+} - (F_R)_{I-}\right]/(\Delta h)_I$$

$$\frac{\partial h_A}{\partial t} = \gamma_h \left(\frac{\partial \hat{p}_A}{\partial t} - \hat{\omega}_A\right) - g\left[(F_h)_{I-} - (F_h)_{B+}\right]/\delta\hat{p} - g\left[(F_R)_{I-} - (F_R)_B\right]/\delta\hat{p}$$

$$\frac{\partial q_A}{\partial t} = \gamma_q \left(\frac{\partial \hat{p}_A}{\partial t} - \hat{\omega}_A\right) - g\left[(F_{q+\ell})_{I-} - (F_{q+\ell})_{B+}\right]/\delta\hat{p}$$

$$\frac{\partial \gamma_h}{\partial t} = \overline{D}\,\gamma_h - 4\left[g\,(F_h)_{I-} - 2(F_h)_A + (F_h)_{B+}\right]/\delta\hat{p}^2 - 4\,g\left[(F_R)_{I-} - 2(F_R)_A + (F_R)_B\right]/\delta\hat{p}^2$$

$$\frac{\partial \gamma_q}{\partial t} = \overline{D}\,\gamma_q - 4\,g\left[(F_{q+\ell})_{I-} - 2\,(F_{q+\ell})_A + (F_{q+\ell})_{B+}\right]/\delta\hat{p}^2$$

where $$\frac{\partial \hat{p}_A}{\partial t} = \left[\frac{\partial \hat{p}_B}{\partial t} + \frac{\partial \hat{p}_I}{\partial t}\right]/2$$

$$\hat{\omega}_A = (\hat{\omega}_B + \hat{\omega}_I)/2$$

$$\delta\hat{p} = \hat{p}_I - \hat{p}_B$$

Table VI. A summary of the predictive equations used in the boundary layer model.

Surface Fluxes

$$(F_h)_o = \rho_o C_T V_o(s_o - s_M) + \rho_o C_q V_o L(q_o - q_M)$$

$$(F_q)_o = \rho_o C_q V_o(q_o - q_M)$$

Top of subcloud layer fluxes

$$(F_q)_{B-} = \frac{k(\Delta q)_B}{(\Delta s_v)_B}(F_{sv})_o$$

$$(F_h)_{B-} = \frac{k(\Delta h)_B}{(\Delta s_v)_B}(F_{sv})_o.$$

where

$$(F_{sv})_o = (F_h)_o - (1 - \delta\epsilon) L(F_q)_o$$

Cloud-base Fluxes

$$(F_h)_{B+} = (F_h)_{B-} + \frac{(\Delta h)_B}{g}(\tilde{\omega}_B - \hat{\omega}_B)$$

$$(F_{q+\ell})_{B+} = (F_q)_{B-} + \frac{(\Delta q)_B}{g}(\tilde{\omega}_B - \hat{\omega}_B)$$

where

$$\tilde{\omega}_B = \{\frac{-gT^*p^* [(F_q)_{B-} - (F_q)_o]}{\hat{p}_B (T^* - \kappa T_B)(q_M + s_q)}$$

$$+ \frac{g (p_o - \hat{p}_B) T_B [(F_s)_{B-} - (F_s)_o + (F_R)_B - (F_R)_o]}{\hat{p}_B (T^* - \kappa T_B) s_M}$$

Fluxes at middle of cloud layer

$$(F_h)_A = (F_h)_{B+}(1 + \mu\delta\hat{p}/2)(1 + \lambda_h\delta\hat{p}/2),$$

$$(F_{q+\ell})_A = (F_{q+\ell})_{B+}(1 + \mu\delta\hat{p}/2)(1 + \lambda_q\delta\hat{p}/2).$$

where

$$\mu = \frac{E}{\delta\hat{p}} - \frac{1}{2\omega_B^* \tau_{adj}}(1 + \frac{2}{3}E),$$

$$\lambda_q = (\frac{\gamma_q}{(\Delta_q)_{CB}} - \frac{E}{\delta\hat{p}})(1 - \frac{E}{3}), \quad \lambda_h = (\frac{\gamma_h}{(\Delta h)_{CB}} - \frac{E}{\delta\hat{p}})(1 - \frac{E}{3})$$

and

$$\omega_B^* = \frac{-g(F_{q+\ell})_{B+}}{(\Delta q)_{CB}} = \frac{-g(F_h)_{B+}}{(\Delta h)_{CB}}$$

Fluxes at top of cloud layer

$$(F_h)_I = (F_h)_{B+}(1 + \mu\delta\hat{p})(1 + \lambda_h\delta\hat{p}) + L(F_{q+\ell})_I^{res}$$

$$(F_{q+\ell})_I = (F_{q+\ell})_{B+}(1 + \mu\delta\hat{p})(1 + \lambda_q\delta\hat{p}) + (F_{q+\ell})_I^{res}$$

See Eq. (III.64) for definition of $(F_{q+\ell})_I^{res}$

Table VII. A summary of the equations used to define the convective fluxes in the model.

Flux at Surface

$$(F_R)_o = (F_R)_{I+} + \frac{c_p}{g}\left[(1-\sigma_R)\,(Q_R)_o^{CLR} + \sigma_R\,(Q_R)_o^{CLD}\right]\hat{p}_I$$

where the specification of $(F_R)_{I+}$ is arbitrary and σ_R, is cloud cover.

Flux at top of mixed layer

$$(F_R)_B = (F_R)_{I+} + \frac{c_p}{g}\left[(1-\sigma_R)\,(Q_R)_o^{CLR} + \sigma_R\,(Q_R)_o^{CLD}\right]\hat{p}_I - \frac{c_p}{g}\left[(1-\sigma_R)\,(Q_R)_M^{CLR} + \sigma_R\,(Q_R)_M^{CLD}\right]\hat{p}_B$$

Flux at layer mid-level

$$(F_R)_A = \frac{c_p}{g}\left\{\left[(Q_R)_{CT}^{CLR} - (Q_R)_{CB}^{CLR}\right](1-\sigma_R) + \left[(Q_R)_{CT}^{CLD} - (Q_R)_{CB}^{CLD}\right]\sigma_R\,\frac{\delta\hat{p}}{4}\right\} + \frac{\left[(F_R)_{I-} + (F_R)_B\right]}{2.0}$$

Flux at top of cloud layer (below inversion)

$$(F_R)_{I-} = (F_R)_{I+} + \frac{c_p}{g}\,\sigma_R\,(Q_R)_o^{CLD}\,\hat{p}_I - \frac{c_p}{g}\,\sigma\left[(Q_R)_M^{CLD}\,\hat{p}_B + (Q_R)_c^{CLD}\,\delta\hat{p}\right]$$

where $(Q_R)_o^{CLD} = (Q_L)_o^{CLR}$ etc.

PARAMETERIZATION I (RAD I)

$(Q_L)_o^{CLR}$ = constant	$(Q_L)_o^{CLD} = (Q_L)_O^{CLR}$
$(Q_L)_M^{CLR} = (Q_L)_C^{CLR} = (Q_L)_o^{CLR}$	$(Q_L)_M^{CLD} = (Q_L)_C^{CLD} = 0$
$(Q_L)_{CT}^{CLR} - (Q_L)_{CB}^{CLR} = 0$	$(Q_L)_{CT}^{CLD} - (Q_L)_{CB}^{CLD} = 0$
$(Q_S)_o^{CLR}$ = constant	$(Q_S)_o^{CLD} = (Q_S)_o^{CLR}$
$(Q_S)_M^{CLR} = (Q_S)_C^{CLR} = (Q_S)_o^{CLR}$	$(Q_S)_M^{CLD} = (Q_S)_C^{CLD} = 0$
$(Q_S)_{CT}^{CLR} = (Q_S)_{CB}^{CLR} = 0$	$(Q_S)_{CT}^{CLD} = (Q_S)_{CB}^{CLD} = 0$

PARAMETERIZATION II (RAD II)

Same as RAD I with the following exceptions

$$(Q_L)_C^{CLR} = (Q_L)_o^{CLR} + (6.43 - 6.84\times10^3\,q_A)\,\hat{p}_B/\hat{p}_I$$

$$(Q_L)_M^{CLR} = (Q_L)_C^{CLR} - 6.43 + 6.84\times10^3\,q_A$$

$$(Q_L)_{CT}^{CLR} = (Q_L)_{CB}^{CLR} = 7.67 - 2.71\times10^2\,\gamma_T - .88\times10^3\,q_A$$

Table VIII. A summary of the equations used to define the radiative fluxes in the model. See text for appropriate units in RAD II parameterizations.

A. Comparison of Steady-State Model Results with Observations

In this section a set of basic parameters, initial conditions and boundary conditions will be specified. The model results obtained with these basic parameters will be compared to the thermodynamic structure observed from the ship Planet from February 7-12, 1969. Although the model is formulated in terms of q and h, the results given below will be given in terms of q and s, since the vertical profiles of q and h are generally quite similar in appearance.

The thermodynamic structure assumed above the inversion is shown in Fig. 15. In the results presented in this paper, these profiles are assumed to be invariant with time. Above $\hat{p}$ = 200 mb the profiles assumed above the inversion are the same as those observed for the Planet. In the lowest 90 mb the profiles assumed above the inversion are drier and cooler than the observed profiles. From 90-200 mb the specified profiles are slightly warmer and drier than that observed during ATEX. The specified atmospheric structure is similar to that observed in the wake of disturbed conditions (Betts, 1976a; Sequin and Garstang, 1976).

The initial conditions used for the model runs are also shown in Fig. 15 and consist of a mixed layer 40 mb in depth with q_M = 12 g·Kg^{-1} and h_M = 325.4 kJ·kg^{-1} (s_M = 296 kJ·kg^{-1}). The cloud layer structure is only considered when the condition

$$q_M + \delta q \geq \frac{\varepsilon \; e_s \; (T_B + \delta T)}{p_o - \hat{p}_B - e_s \; (T_B + \delta T)} \; , \qquad (V.1)$$

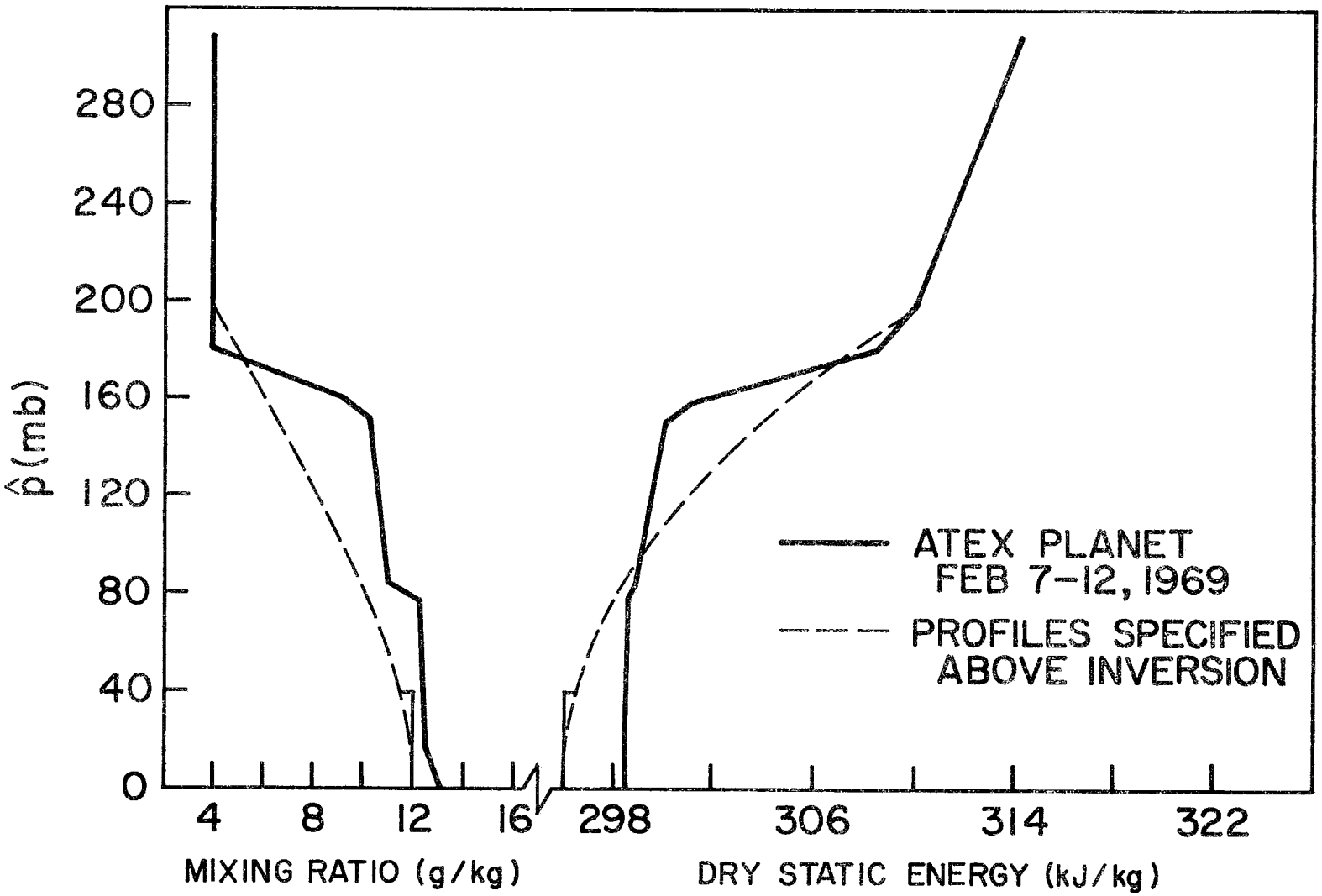

Figure 15. Initial boundary layer structure assumed for the model and profiles of s and q assumed above the boundary layer compared with structure observed from Planet, Feb. 7-12, 1969.

is satisfied. Before (V.1) is satisfied the model is basically a dry mixed layer model and only q_M, h_M and $\hat{p}_B$ are predicted. When (V.1) is satisfied and the cloud layer begins to form, the cloud layer is assumed to have an initial depth of 5 mb and the initial values of q and h at cloud base are assumed to have the value of the specified profile (see Fig. 15) at that level. The initial lapse rates of q and h are specified to be the Planet lapse rates shown in Fig. 15. The surface wind speed, V_o, the sea surface temperature, T_o, and the mean divergence, $\bar{D}$, are specified from the observations made during ATEX. The variables V_o and T_o were specified from the Planet ship observations averaged from February 7-12, 1969 (Augstein et al., 1973). These averages give V_o = 7 ms^{-1} and T_o = 24.9°C. The large-scale divergence profile determined by Augstein et al., gives $\bar{D} = 5.7X10^{-6}$ sec^{-1}.

The radiative fluxes in this simulation are obtained by using the RAD I parameterization with $(Q_L)_o^{CLR} = (Q_L)_o^{CLD} = -4°C\ day^{-1}$ and $(Q_s)_o^{CLR} = (Q_s)_o^{CLD} = .8°C\ day^{-1}$. A visible cloud cover of 50% is assumed so that $\sigma_R = .50$. The convective flux parameters are specified as $\Delta T_o = .5°C$ and τ_{adj} = 1/3 day, k = .25 and $\delta q = .4\ g \cdot kg^{-1}$. A summary of the structure specified above the inversion; initial conditions; and large-scale, radiative, and convective parameters is given in Table IX.

The model structure was predicted using the parameters specified above. The predicted structure becomes nearly steady-state after 48 hours and absolutely steady after 70 hours of integration. The steady-state structure is compared with the ATEX Planet observations in Fig. 16. In general, the agreement is good although the structure predicted by the model is approximately 1/2 $g \cdot kg^{-1}$ more moist and 1°C warmer than the observed values. In the cloud layer the predicted average moisture

INITIAL CONDITIONS

a) Before Clouds

i) $q_M = 12.0\ g \cdot kg^{-1}$

ii) $h_M = 325.44\ kJ \cdot kg^{-1}$

iii) $\hat{p}_B = 4.0\ kPa$ (40 mb)

b) After Clouds

i) $q_A = q(\hat{p}_B) + \gamma_q(\hat{p}_I - \hat{p}_B)/2$

ii) $h_A = h(\hat{p}_B) + \gamma_h(\hat{p}_I - \hat{p}_B)/2$

iii) $\gamma_q = -.1335\ g \cdot kg^{-1}\ kPa^{-1}$

iv) $\gamma_h = -.0857 J \cdot kg^{-1}\ Pa^{-1}$

v) $\hat{p}_I = \hat{p}_B + 0.5\ kPa$

BOUNDARY CONDITIONS

a) Surface Parameters

i) $p_o = 101.46\ kPa$ (1014.6 mb)

ii) $T_o = 298.°K$

iii) $V_o = 7.0\ ms^{-1}$

b) Profiles Specified Above Inversion

i) for $0 < \hat{p} < 20$ kPa

$q(\hat{p}) = 12.0\ (g \cdot kg^{-1})\ X$

$\exp\ [-(\hat{p}/19.081)^2]$

for $\hat{p} > 20$ kPa

$q(\hat{p}) = 4.0\ (g \cdot kg^{-1})$

ii) for $0 < \hat{p} < 20$ kPa

$h(\hat{p}) = 296.0\ (kJ \cdot kg^{-1})X$
$\exp\ [-(\hat{p}/92.482)^2] + Lq\ (\hat{p})$

for $\hat{p} > 20.0$ kPa

$h(\hat{p}) = 312.5\ (kJ \cdot kg^{-1}) +$
$.374\ (kJ \cdot kg^{-1} \cdot kPa^{-1})\ \hat{p} + Lq\ (\hat{p})$

SPECIFIED PARAMETERS

a) Large-Scale Parameters

$\bar{D} = 5.7X10^{-6} \cdot s^{-1}$

b) Convective Parameters

i) $k = .25$

ii) $\delta q = .4\ g \cdot kg^{-1}$

iii) $\Delta T_o = .5°C$

iv) $\tau_{adj} = 1/3$ day

c) Radiative Parameters

i) $\sigma_R = .50$

ii) $(Q_L)_o^{CLR} = -4°C\ d^{-1}$

iii) $(Q_S)_o^{CLR} = .8°C\ d^{-1}$

Table IX. A summary of boundary conditions, initial conditions, large-scale parameters and radiative and convective parameters assumed for basic model runs.

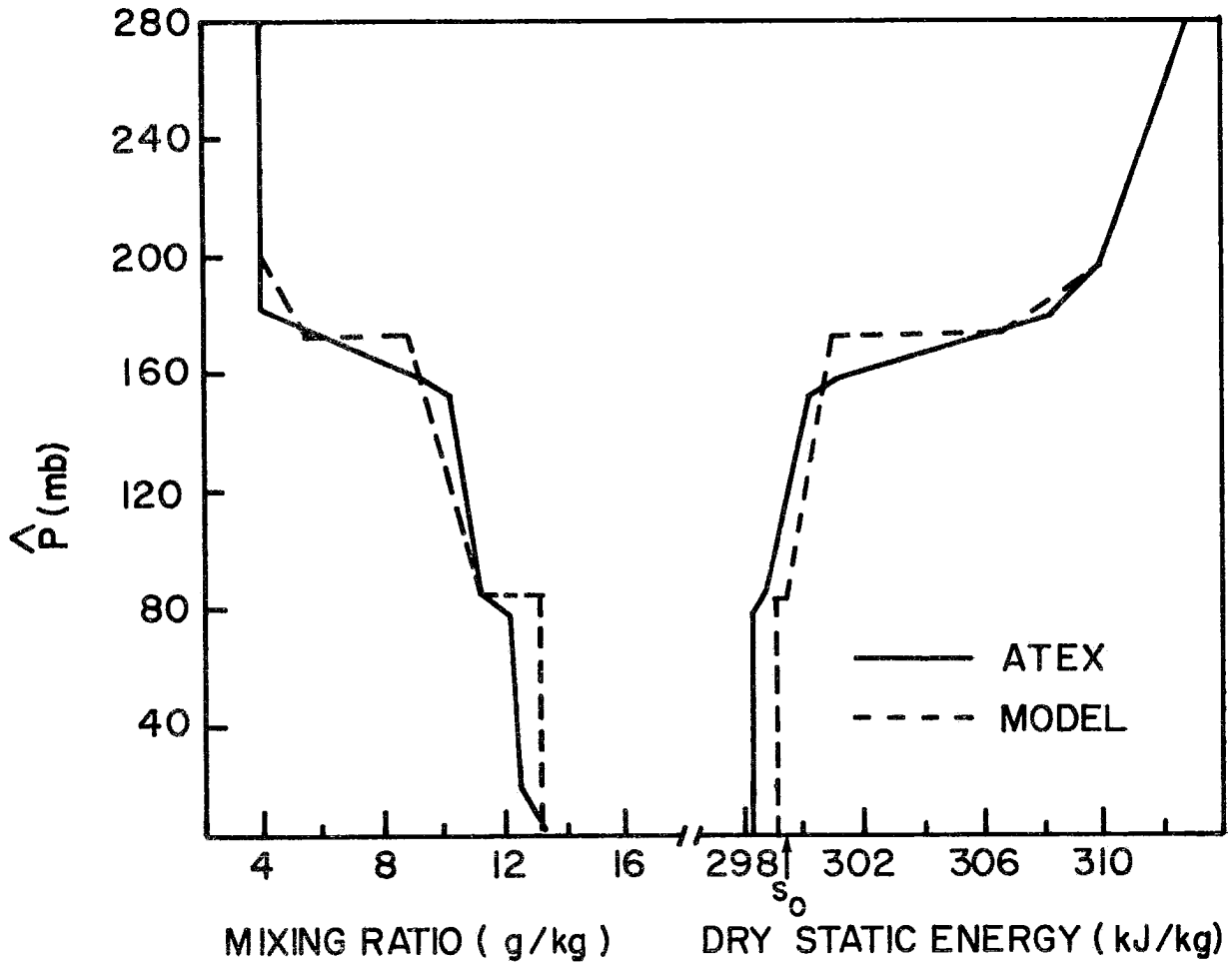

Figure 16. A comparison between steady-state model solution and the thermodynamic structure observed from the Planet, Feb. 7-12, 1969.

agrees well with the observations while the predicted dry static energy is greater than that observed. The predicted lapse rate of q is greater than is observed while the dry static energy profile indicates that the predicted cloud layer stability is slightly less than the observed stability.

The model fluxes corresponding to the steady-state structure shown in Fig. 16 are shown in Fig. 17 and illustrate the balance between the radiative, convective, and large-scale processes. Since the fluxes shown in Fig. 17 are for steady-state conditions, the moisture flux in the subcloud layer is constant with height. In the cloud layer the convective moistening balances the drying due to large-scale subsidence. The fluxes shown in Fig. 17 indicate that the radiative cooling in both the mixed layer and the cloud layer is approximately balanced by the convective heating. This balance is consistent with the diagnostic results given by Betts (1975). The discontinuity in the radiative fluxes at the trade inversion is approximately the same magnitude as the discontinuity in $F_{s\ell}$. In Betts (1975) the cooling due to convection dominated the processes within the inversion. The radiative heating profile used in his study, however, had a minimum in the longwave cooling at the trade inversion.

The neglect of horizontal advection may at least partially account for the discrepancies between the predicted and observed boundary layer structure. During BOMEX, for example, the time change of moisture due to horizontal advection was approximately 1 $g \cdot kg^{-1}$ day^{-1} in the subcloud layer (Holland and Rasmusson, 1973). The results given by Augstein et al. (1973) also show a significant downstream transport of moisture and dry static energy in the cloud and subcloud layer. The effect of

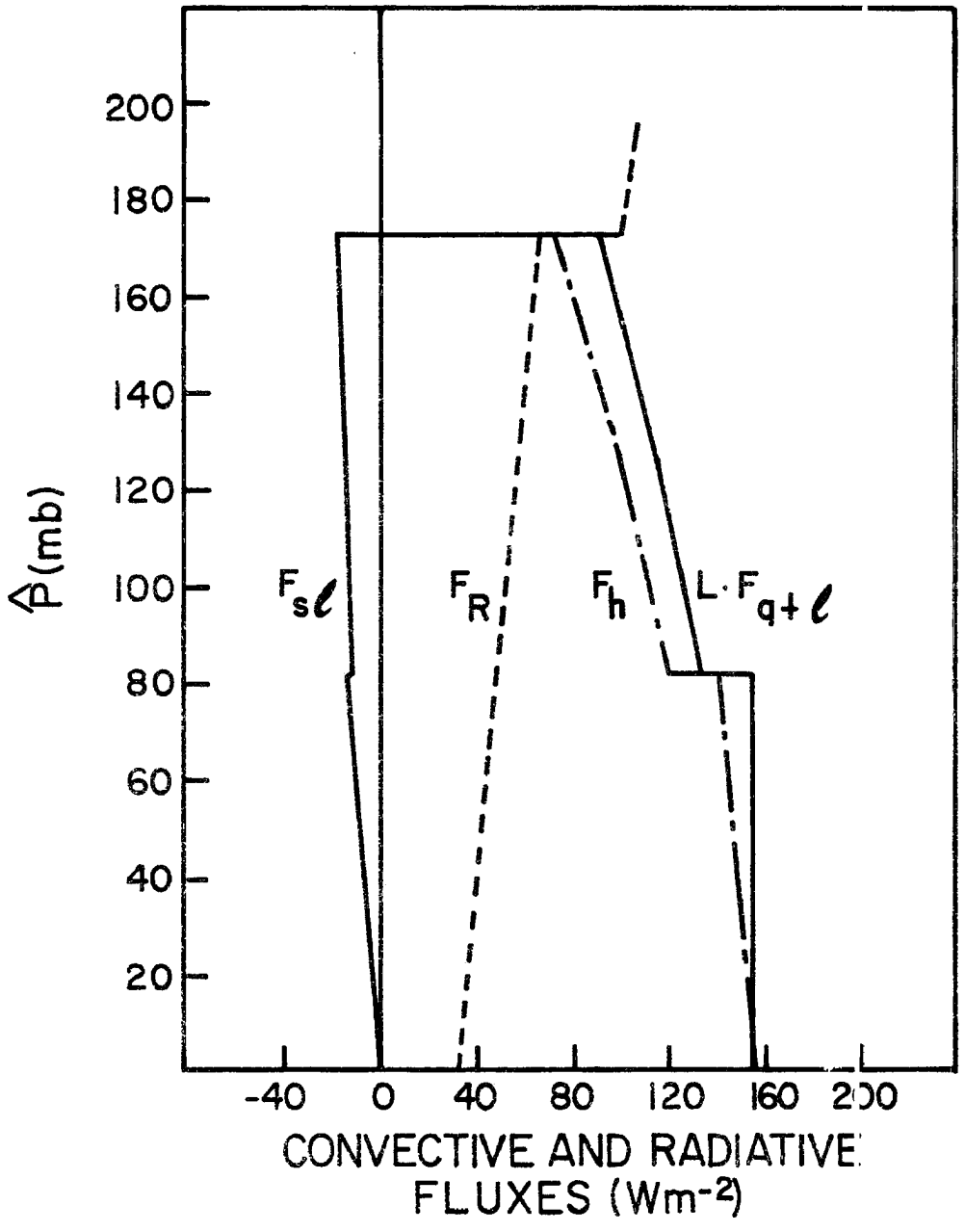

Figure 17. Convective and radiative model fluxes for steady-state structure shown in Figure 16.

advection is most easily evaluated quantitatively by considering the variation of the thermodynamic structure along an idealized surface air trajectory. This is relatively easy to perform with the model if it is assumed that the movement of air along the trajectory is uniform in the vertical. With this assumption the time variable in the model may be replaced by distance according to the relationship $x = V_o t$. The sea surface temperature may then be specified as a function of distance.

The integration of the model along a trajectory was used to evaluate the effect of advection on the predicted structure. For this calculation the horizontal gradient of sea surface temperature was assumed to be

$$\frac{\partial T_o}{\partial x} = 1.5 \times 10^{-6} \text{ °C m}^{-1}.$$

This approximately corresponds to the sea surface temperature gradient observed from the ship Planet as it drifted with the winds from February 7-12, 1969. The observations of Riehl et al. (1951) along a surface trajectory in the Pacific also indicate a gradient in the sea surface temperature of $\approx 1.5 \times 10^{-6}$ °C m^{-1}. The calculation was performed by initializing the integration with the conditions shown in Fig. 16 and integrating the model for 24 h with a constant sea surface temperature of 296.5K. All other parameters for this calculation were identical to those specified in Table IX. After 24 h the sea surface temperature was varied to simulate the movement of the structure downstream at the rate of $V_o = 7$ ms^{-1}.

The structure obtained at the point downstream where the sea surface temperature was equivalent to the Planet sea surface temperature is shown in Fig. 18. The difference between the steady-state results and the observations shown in Fig. 16 are almost completely eliminated by simulating the effect of advection. The fluxes corresponding to the model structure shown in Fig. 18 are compared to the fluxes deduced for the ATEX triangle during the period from February 7-12, 1969 (Augstein et al. 1973) in Fig. 19. The magnitude and the vertical distribution of the calculated and the observationally determined fluxes are in good agreement. The observed fluxes show slightly more moistening in the subcloud layer than is indicated by the model fluxes. This feature is also evident in the BOMEX fluxes (Betts, 1975) which are also shown in Fig. 19. This moistening may balance the drying due to the large-scale subsidence and the fact that the observed moisture distribution in the subcloud layer is not entirely mixed.

It is important to note, however, that the agreement between the model and observed fluxes is quite good in both the magnitude and in the vertical distribution. The discontinuity in the fluxes at cloud base would probably not be discernable from observations unless special care was taken in the averaging process. The BOMEX fluxes at the inversion are not sharply defined since no attempt was made to normalize the averaged data with respect to the inversion height.

B. Sensitivity of the Model Results to Specified Parameters

There are two types of parameters which are specified in the model which may affect the predicted structure. Some parameters such as ΔT_o and τ_{adj} result from the assumptions used to close the parameterization of the convective fluxes. While these parameters may have some

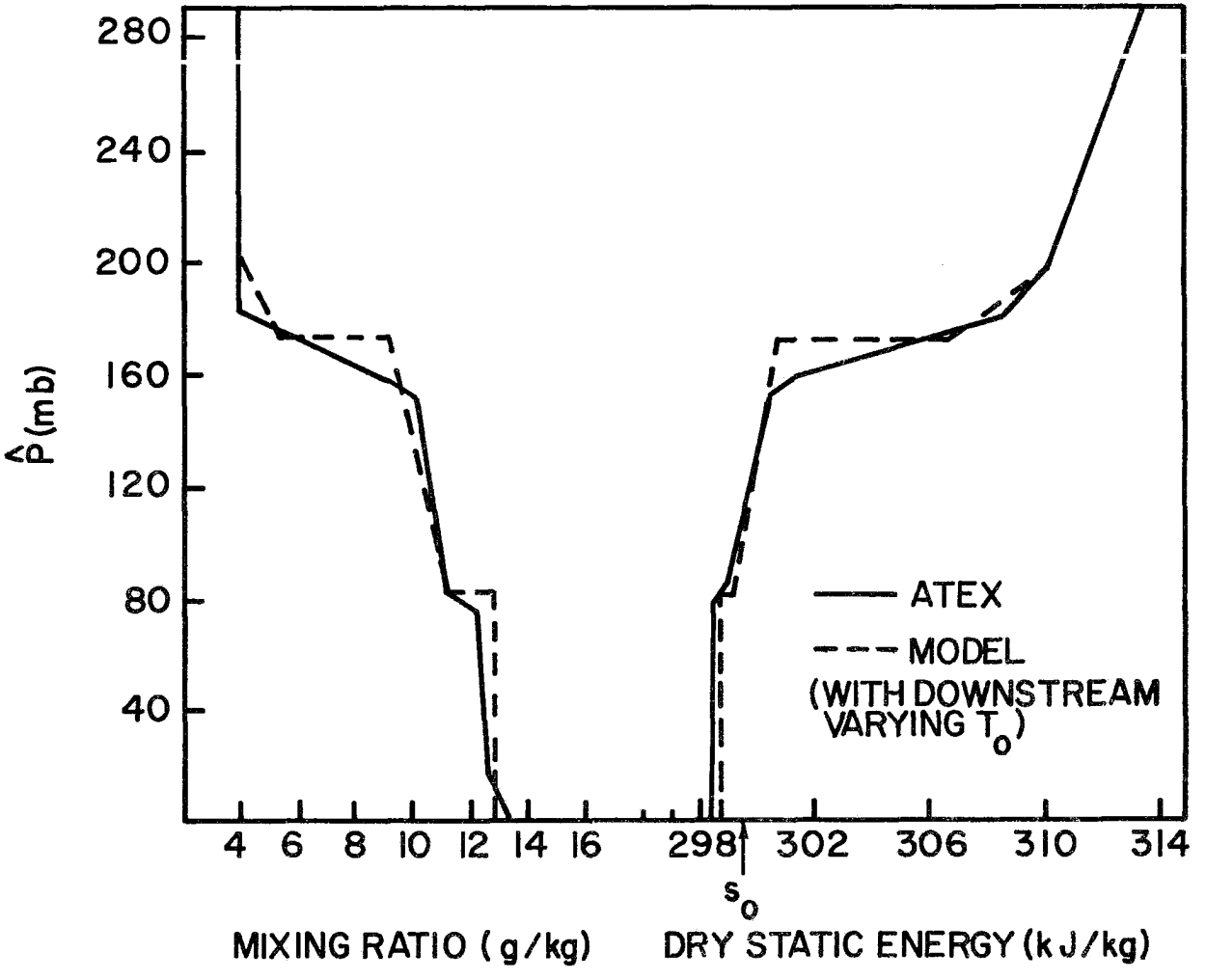

Figure 18. A comparison of model results obtained by a downstream integration to the observed Planet thermodynamic structure.

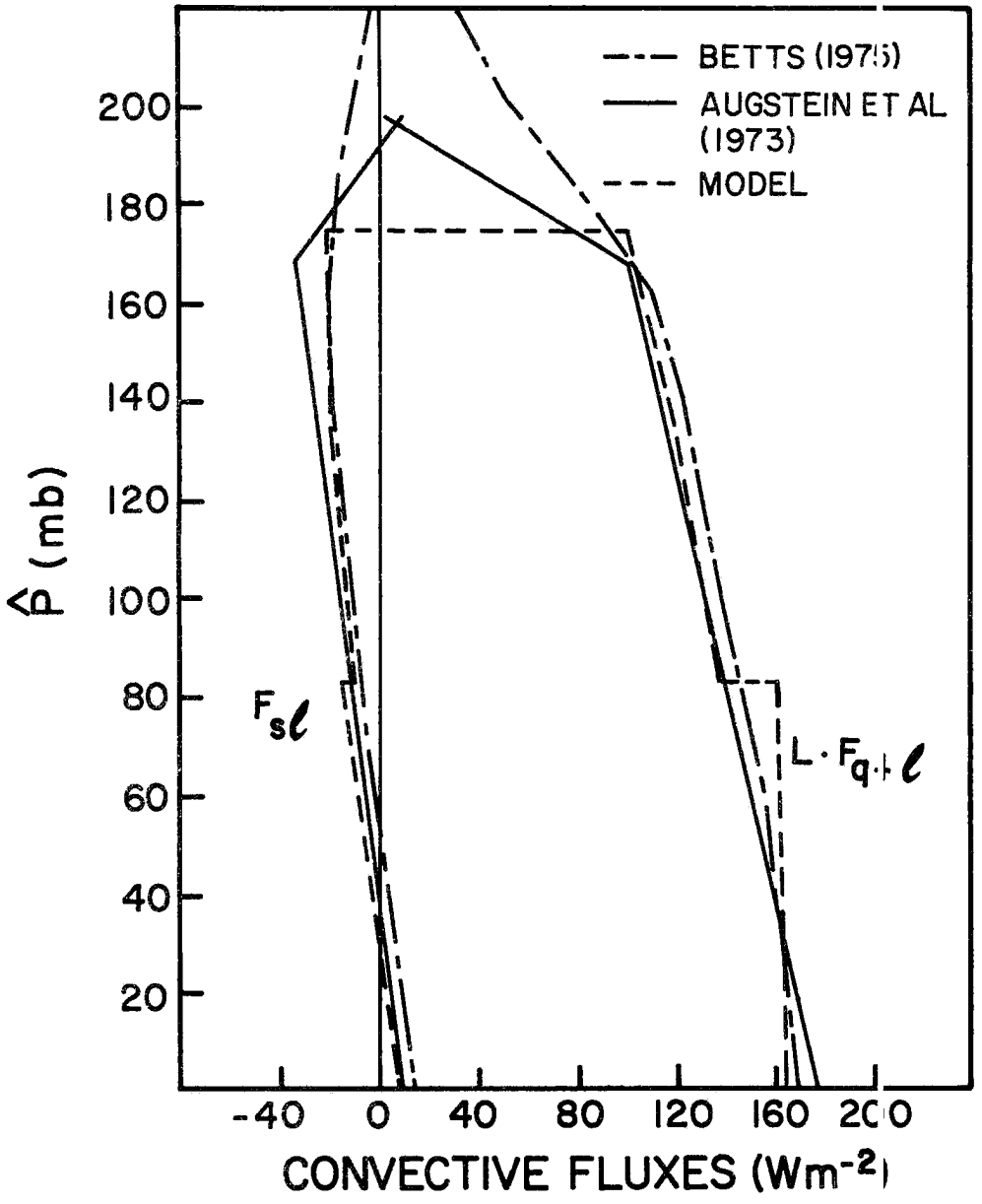

Figure 19. A comparison of the model convective fluxes obtained by a downstream integration and the fluxes obtained from BOMEX (Betts, 1975) and ATEX (Augstein et al., 1973).

conceptual physical interpretation, they may be difficult to define from observations. Consequently, it is hoped that the model results will be relatively insensitive to these parameters. Other specified parameters such as T_o, V_o, $\bar{D}$, σ_R, and $(Q_L)_o^{CLR}$ are physical parameters which may vary in the real atmosphere. The sensitivity of the model to these parameters provides information which may result in a better understanding of the role of various processes which alter the boundary layer structure.

In this chapter the sensitivity of the steady-state solutions of the model to various disposable and physical parameters will be determined. The initial conditions, boundary conditions and external parameters specified in Table IX will be used unless specifically noted otherwise.

The steady-state predicted for τ_{adj} = 1/4 day and τ_{adj} = 1/2 day are shown in Fig. 20. In the mixed layer the differences between these two model runs are very small. The structure predicted with an adjustment time of 1/2 day results in a cloud layer which is $\simeq$ .50 $g \cdot kg^{-1}$ drier and $\simeq$ .5°C cooler than that predicted with an adjustment time of 1/4 day. The height of the inversion is approximately the same for both calculations. The slope of q and s in the cloud layer do not vary significantly between the two calculations although the jump in q at cloud base is somewhat sensitive to the specification of this parameter. The effect of increasing the adjustment time is equivalent to allowing the atmosphere to dry and warm slightly more due to the large-scale subsidence field.

The model results for ΔT_o = 0.5 and ΔT_o = 0.0°C are shown in Fig. 21. The principal effect of altering this parameter is to alter the

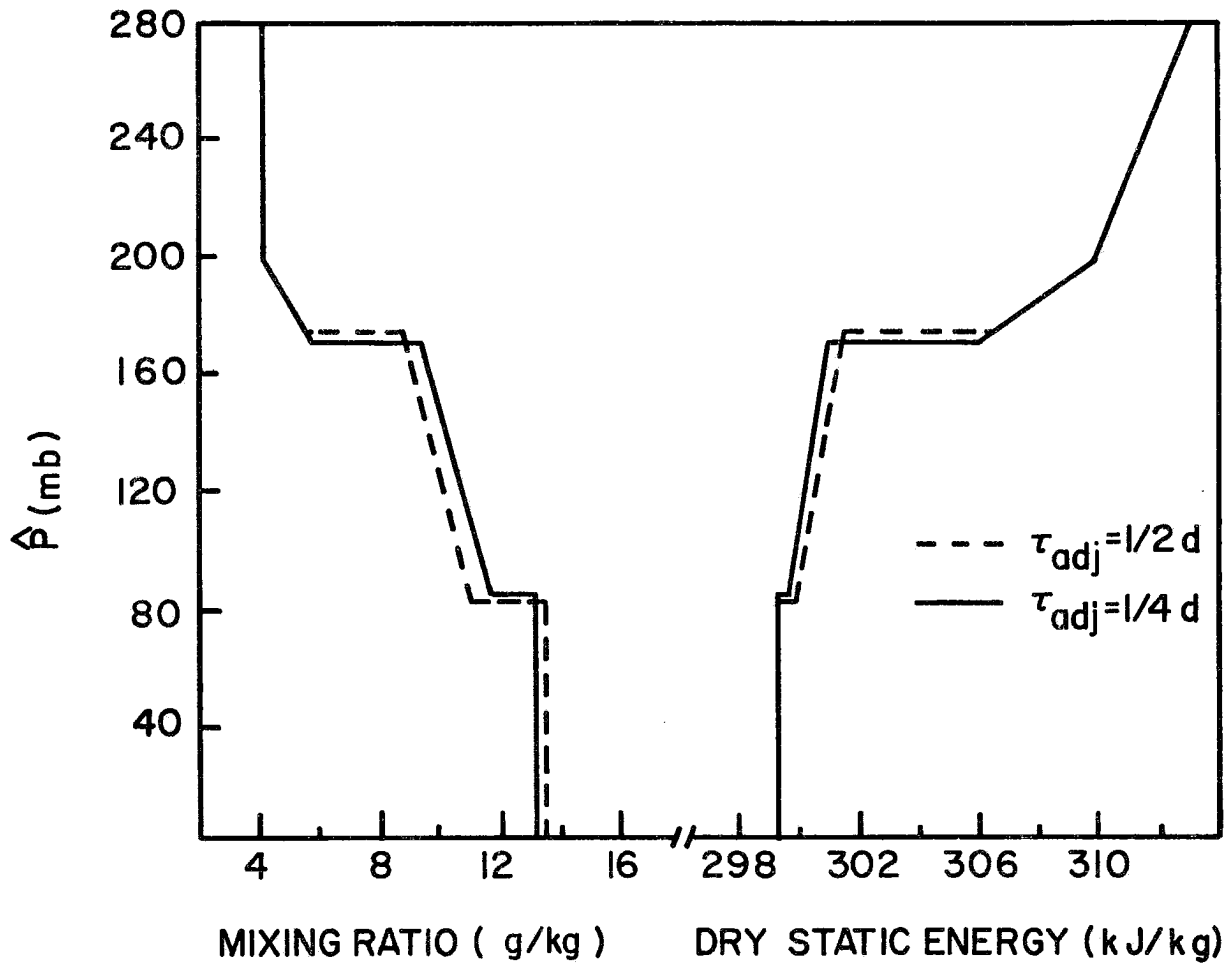

Figure 20. Steady-state model structure for τ_{adj} of 1/4 and 1/2 day.

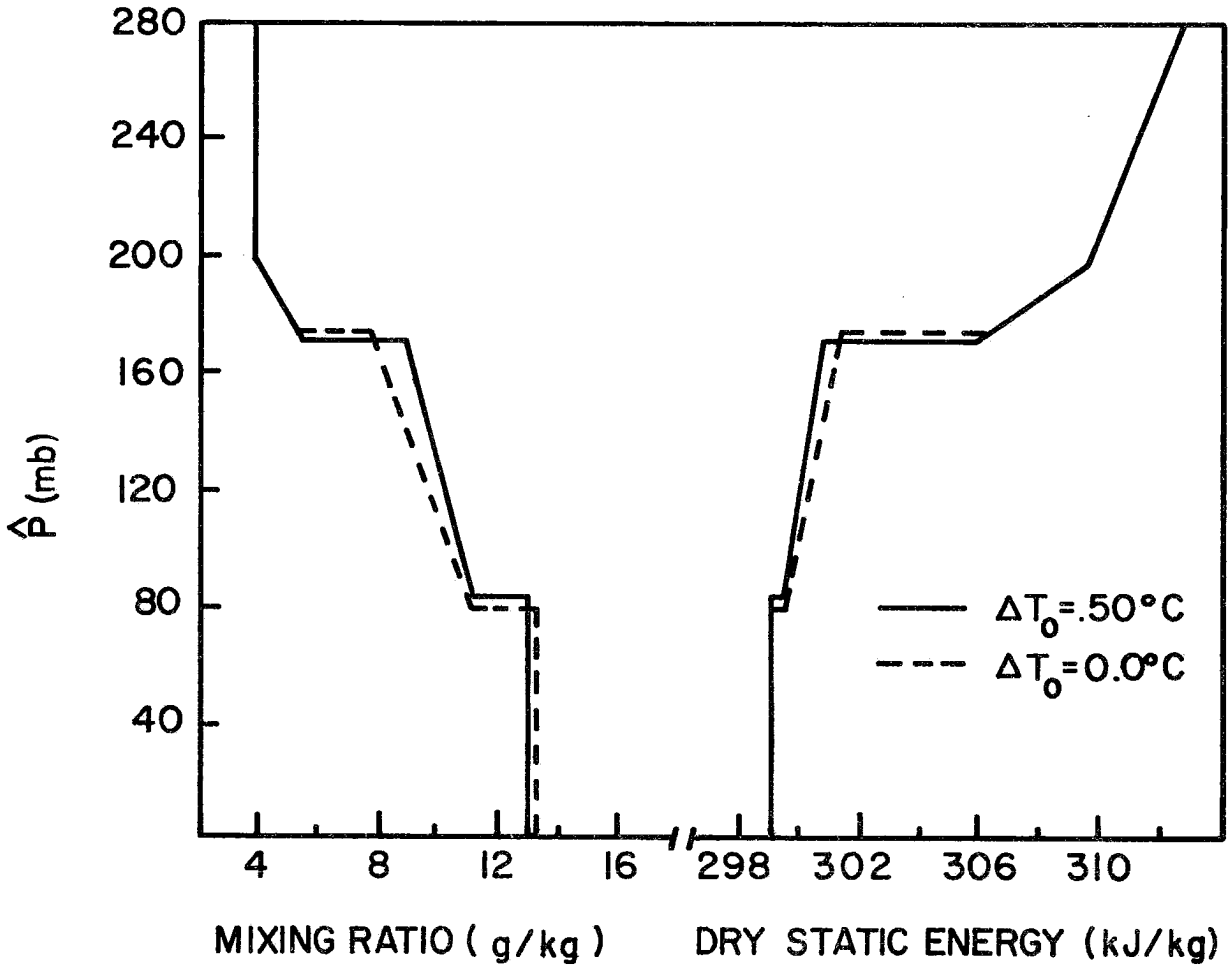

Figure 21. Steady-state model structure for ΔT_0 of 0.5°C and 0.0°C.

lapse rates of q and s in the cloud layer. The larger ΔT_o results in the layer becoming more unstable. This result is consistent with the qualitative results discussed in Chapter III. It is interesting to note that the results obtained with ΔT_o = 0.0°C more closely resemble those obtained with τ_{adj} = 1/2 day. This suggests the possibility that these closure parameters may not be independent of each other. The results presented here, however, indicate that the steady-state solutions are not extremely sensitive to the specification of either τ_{adj} or ΔT_o. The rate of growth of the boundary layer is equally insensitive to these parameters.

Additional runs were also made to determine the sensitivity of the model results to the specification of k and δq. The structures predicted for k = .40 and for k = .10 are shown in Fig. 22. Since typical values assumed for k range from .2 - .3 the sensitivity of the model results to this parameter are indeed small. The structure for δq = 0 and δq = .40 $g \cdot kg^{-1}$ is shown in Fig. 23. The specification of this parameter results in a slight difference in the height of cloud base and of the inversion. It is interesting to note, however, that δ_T, which is derived from the model results, is $\simeq$ -.1°C which is in good agreement with the LeMone and Pennell (1976) measurements discussed previously.

The sensitivity of the model predicted structure to physical parameters will be determined in the remainder of this chapter. The model steady-state solutions are shown in Fig. 24 for $\overline{D} = 4X10^{-6}$ sec^{-1} and $\overline{D} = 8X10^{-6}$ sec^{-1}. The principal differences between the boundary layer structure obtained with various divergence values is the height of the inversion. When the divergence is increased from $4X10^{-6}$ s^{-1} to $6X10^{-6}$ s^{-1}, the height of the inversion decreases by $\simeq$ 25 mb. As

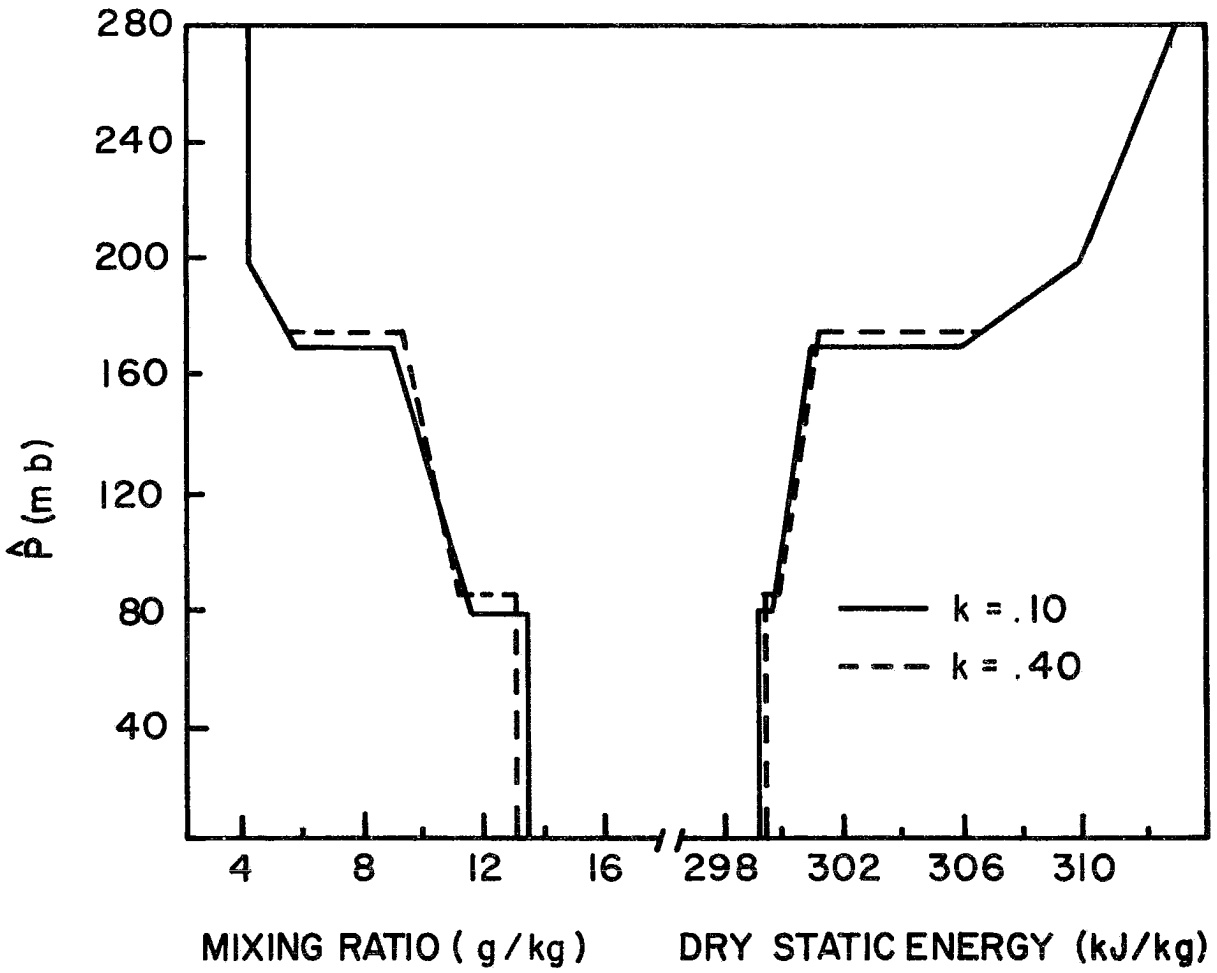

Figure 22. Steady-state model structure for k = .40 and k = .10.

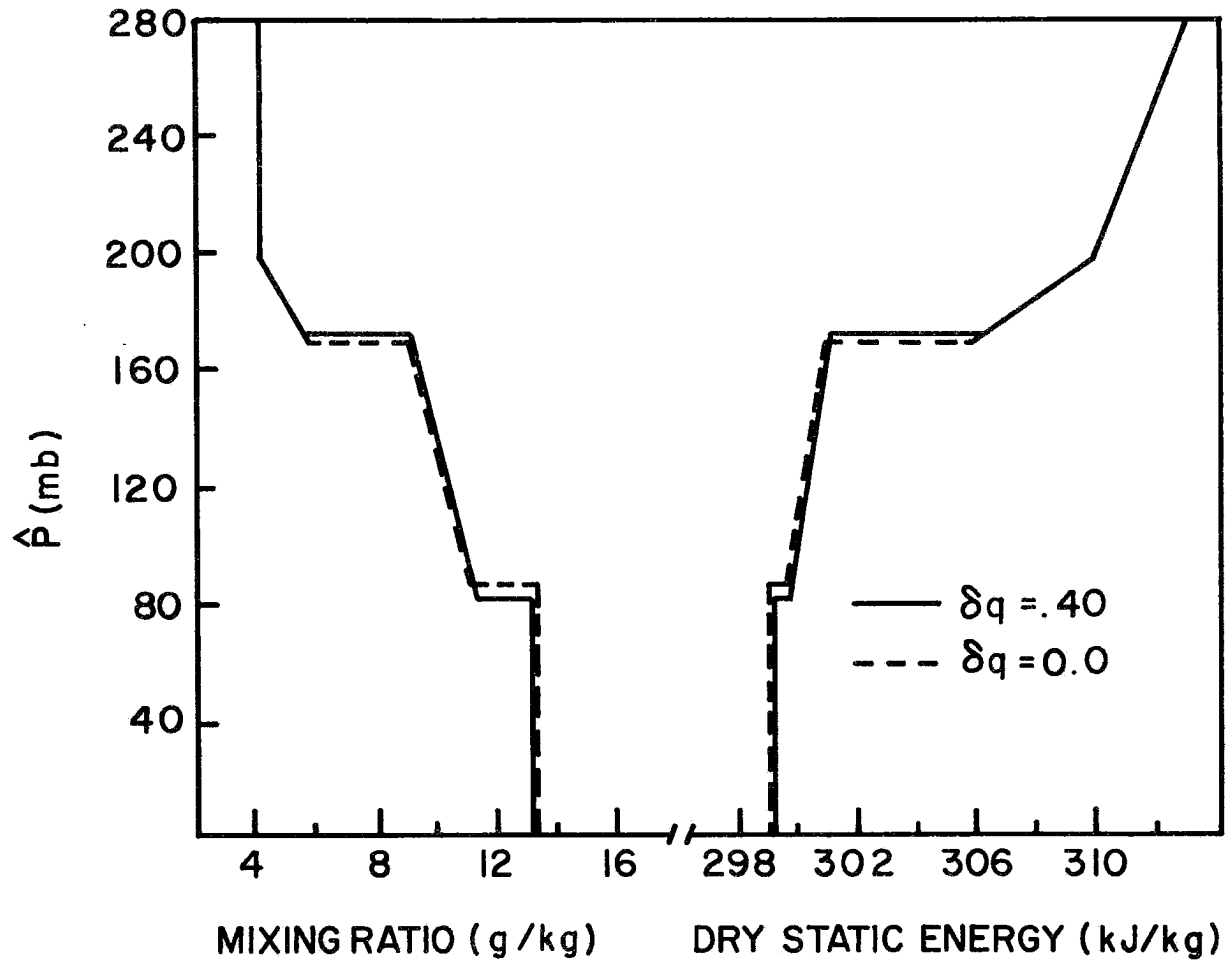

Figure 23. Steady-state model structure predicted for $\delta q = 0$ and $\delta q = .4$ gkg^{-1}.

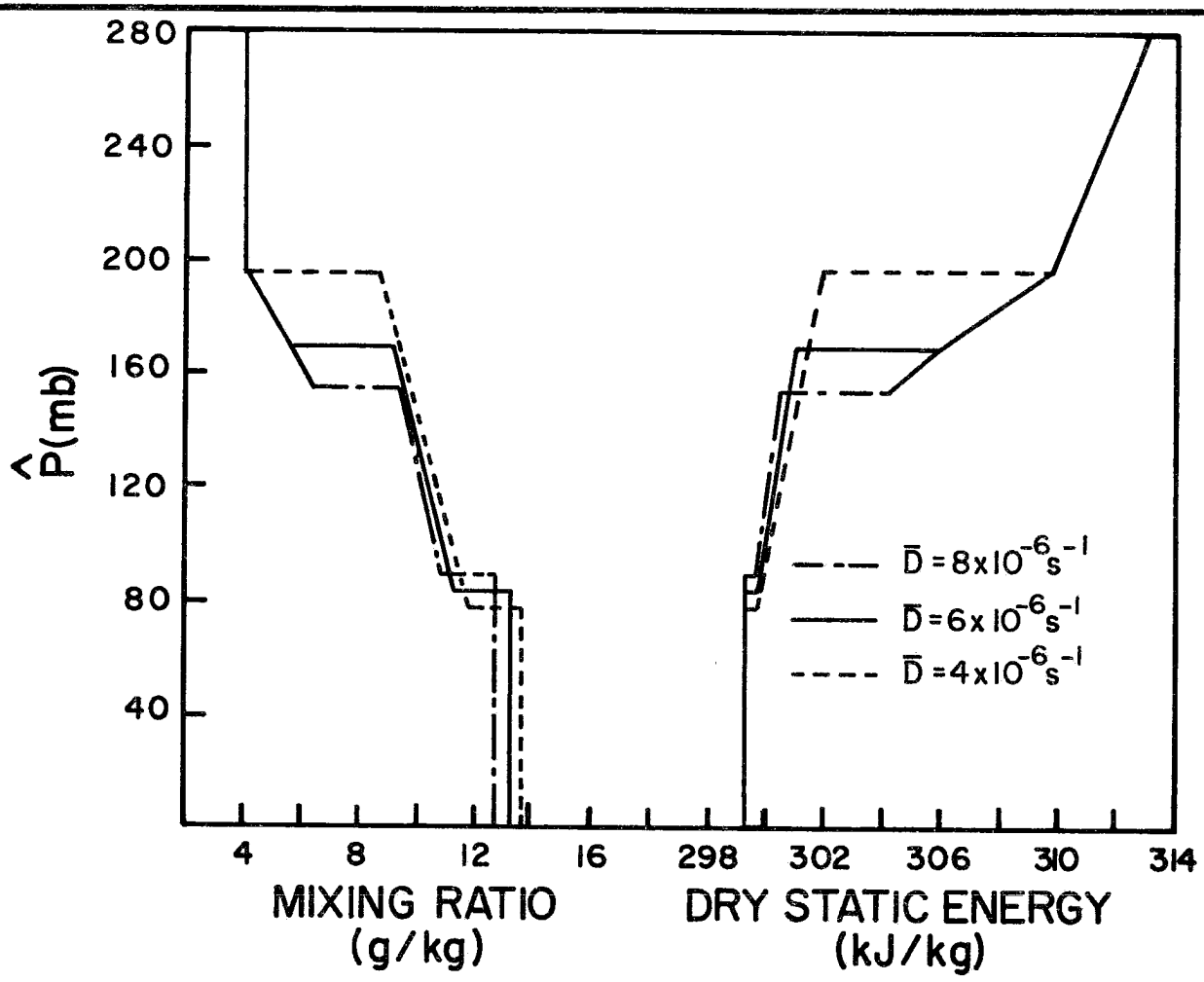

Figure 24. Steady-state model structure for large-scale divergence values of $4X10^{-6}$ sec^{-1}, $6X10^{-6}$ sec^{-1} and $8X10^{-6}$ sec^{-1}.

the divergence is increased to $8X10^{-6}$ s^{-1} the height of the inversion only decreases by ≃ 15 mb.

The sensitivity of the inversion height to variations in the divergence is qualitatively reasonable, since for steady-state conditions there is a balance between the drying due to large-scale subsidence and moistening due to moist convection. In the dry static energy profile there is a balance between the radiative and convective cooling at the trade inversion and the subsidence warming. Since the subsidence increases linearly with pressure and the convective cooling and moistening do not vary significantly with divergence, the level at which the balance described above will occur decreases as the large-scale divergence increases. The structure below the inversion does not vary significantly with divergence. The small variations in the depth of the subcloud layer are consistent with the small variations in the subcloud layer values of q and s.

Steady-state solutions obtained with a sea surface temperature of 299 K and 297 K are shown in Fig. 25. The principal differences in the structure for these two cases is in the depth of the subcloud layer, and in the vertical profile of dry static energy. The dry static energy profile obtained with a sea surface temperature of 297 K is ≃ 2 $kJ \cdot kg^{-1}$ less than that obtained with a sea surface temperature of 299 K. The cooler sea surface results in a moisture profile that is ≃ .5 $g \cdot kg^{-1}$ drier in both the cloud and subcloud layer. It should be noted that while the cooler sea surface temperature results in a lower trade inversion, cloud base is lower by an approximately equivalent amount. Consequently, the model predicts that the depth of the cloud layer does not depend significantly on the sea surface temperature. In comparison, the

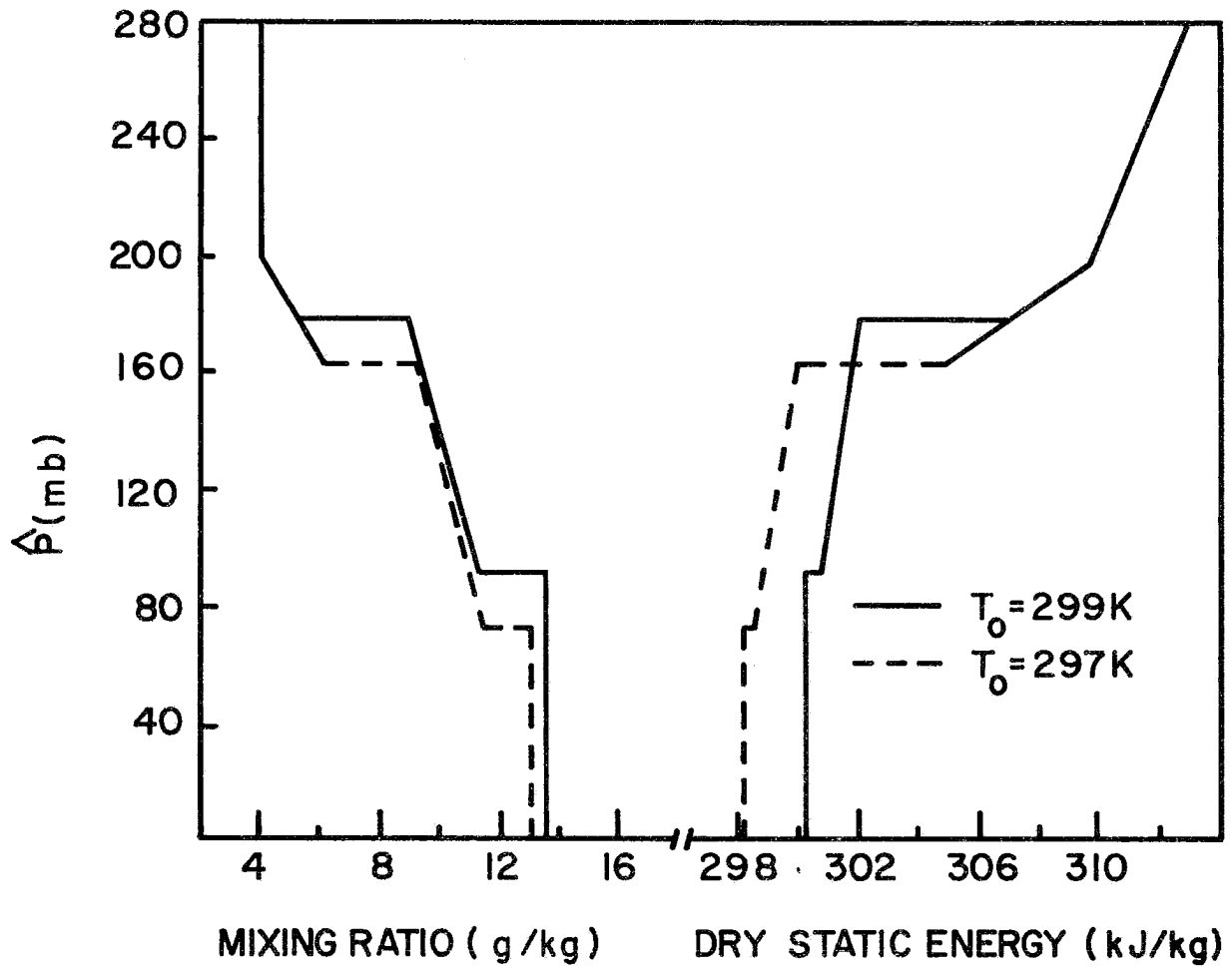

Figure 25. Same as Figure 24 but for sea surface temperature of 297 and 299 K.

results given in Fig. 24 indicate that the depth of the subcloud layer is nearly independent of the large-scale divergence while the depth of the cloud layer increases with smaller divergence values.

The trades are characterized by extremely steady winds. The wind speed, however, may be influenced by nearby disturbances, particularly in the wake of disturbed conditions. The steady-state model solutions are shown in Fig. 25 for a surface wind speed of 10 ms^{-1} and 5 ms^{-1}. This is also equivalent to varying the bulk transfer coefficients C_T and C_q. The profiles shown in Fig. 25 indicate significant variations particularly in the subcloud layer in both the temperature and moisture structure with variations in the surface wind velocity. The structure obtained with a surface wind velocity of 5 ms^{-1} indicates a significantly cooler and drier boundary layer than that obtained with V_o = 10 ms^{-1}. The smaller surface wind results in a deeper subcloud layer but a shallower cloud layer. These results indicate that variations in the surface fluxes may significantly alter the boundary layer structure.

An interesting characteristic of the results obtained by varying sea surface temperature and wind speed is illustrated in Fig. 27. This figure shows a plot of the steady-state inversion height as a function of the surface flux of moisture for various sea surface temperatures and wind speeds. These results indicate a nearly linear relationship between the height of the inversion and the surface flux of moisture. On the other hand, the change in the height of the inversion due to changes in the large-scale divergence show very little correlation with the surface fluxes.

The results given in Chapter IV indicate that the boundary layer radiative heating rates are somewhat insensitive to temperature and

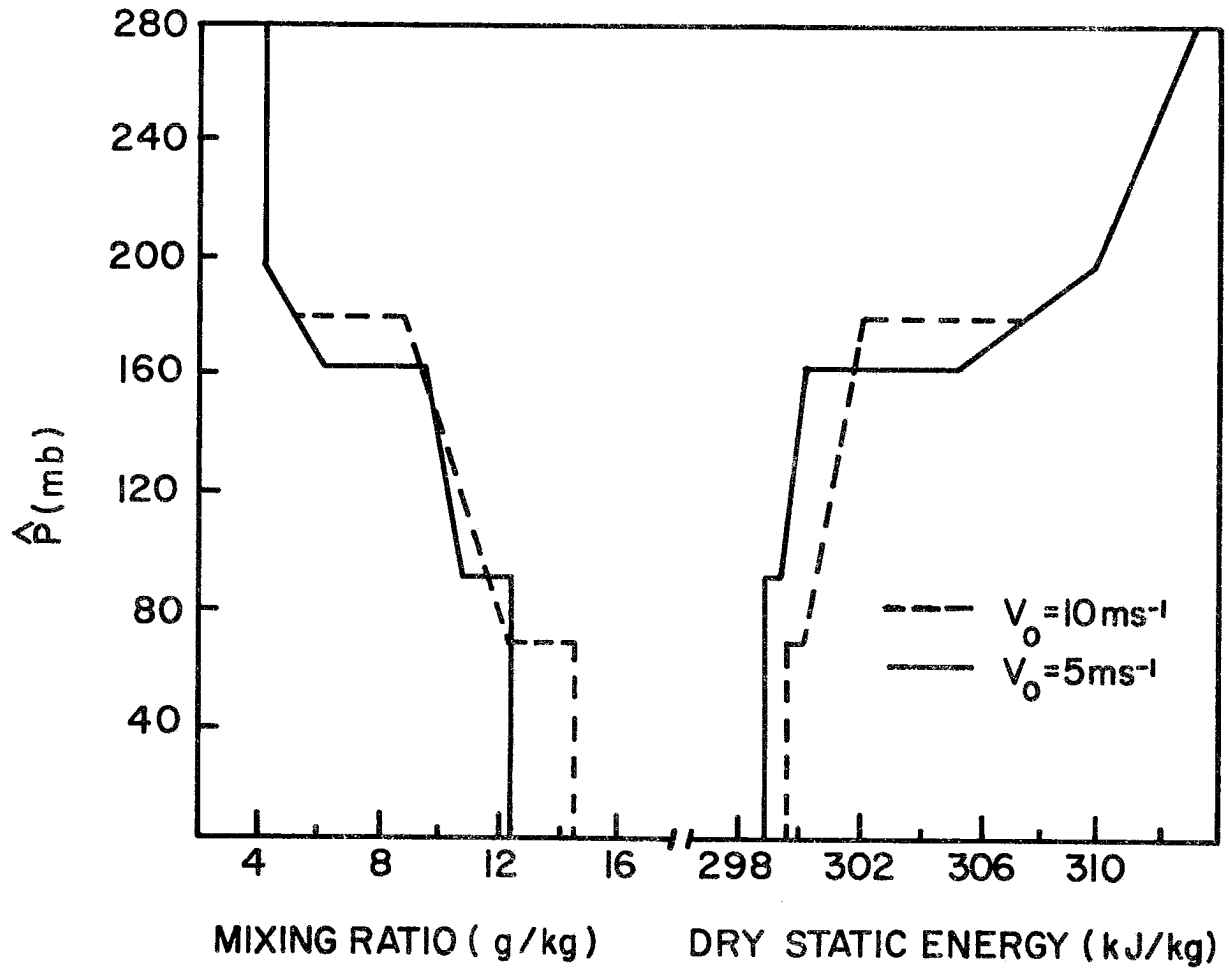

Figure 26. Same as Figure 24 but for surface wind speed of 10 ms^{-1} and 5 ms^{-1}.

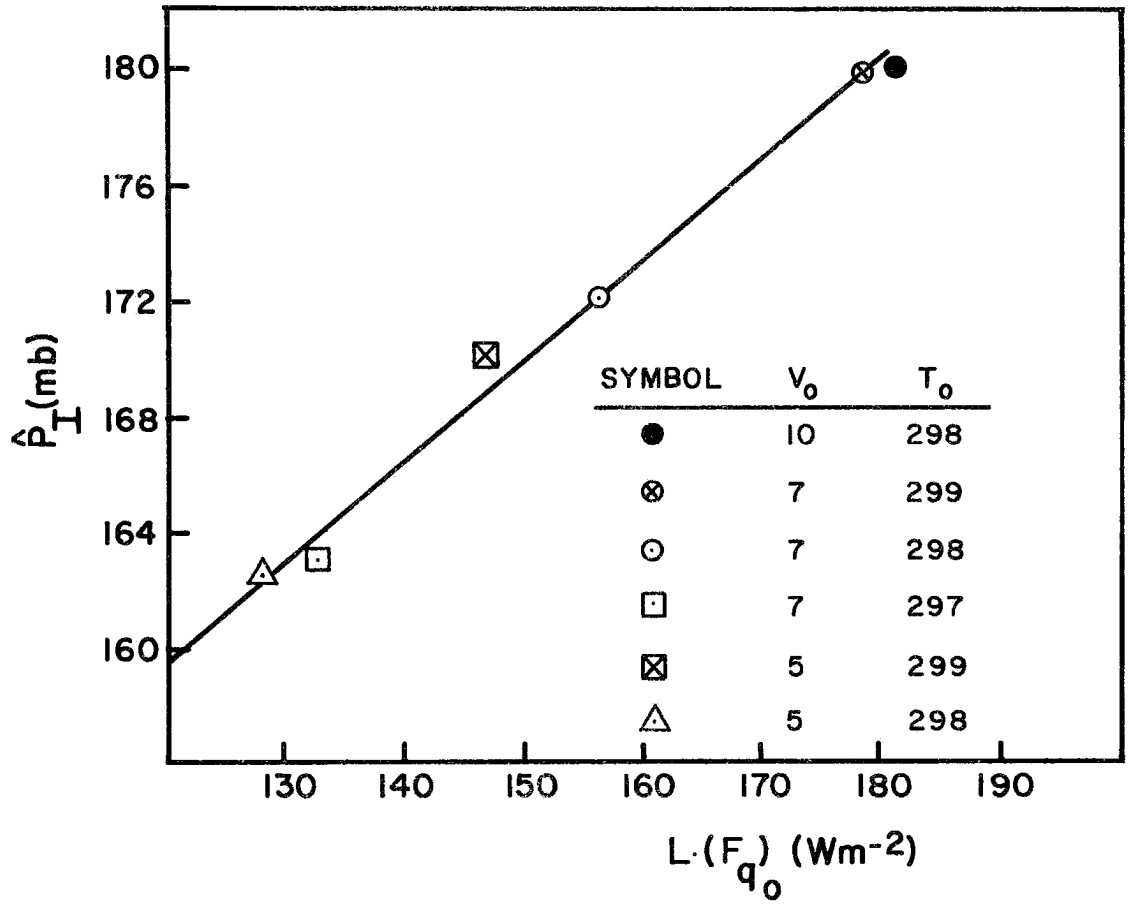

Figure 27. A plot of the steady-state height of the trade inversion as a function of the surface flux of moisture for various sea surface temperatures and wind velocities.

moisture variations within the boundary layer. The cloud cover and moisture distribution above the boundary layer, however, may affect the magnitude of both longwave and shortwave heating rates. Starr (1976), for example, has shown the boundary layer infrared heating to be sensitive to the emissivity of higher level clouds. The radiometersonde measurements made during the Line Island Experiment (Cox, 1969), indicate significant variations in boundary layer heating rates due to upper-level cloudiness. As indicated previously, there is also some uncertainty in the magnitude of heating by the direct absorption of solar radiation. The effect of variations in the average boundary layer heating rates was evaluated by varying $(Q_L)_o^{CLR}$. The steady-state model solutions are shown in Fig. 28 for $(Q_L)_o^{CLR} = -4°C\ day^{-1}$ and $(Q_L)_o = -2°C\ day^{-1}$. Since the solar heating rate integrated over the entire day is assumed to be $.8°C\ day^{-1}$, the boundary layer heating shown in Fig. 28 is for a radiative heating rate of $-3.2°C\ day^{-1}$ and $-1.2°C\ day^{-1}$. These variations in the boundary layer heating may alternately be interpreted as an increase in the solar absorption. The results shown in Fig. 28 show that the model structure predicted with suppressed longwave cooling is warmer by $\simeq .5°C$ than that obtained with $(Q_L)_o^{CLR} = -4°C\ day^{-1}$. The suppressed cooling also results in a more moist but shallower boundary layer. The height of the inversion is $\simeq$ 25 mb lower for $(Q_L)_o^{CLR} = -2°C\ day^{-1}$ than it is for $(Q_L)_o^{CLR} = -4°C\ day^{-1}$. Cloud base only differs by $\simeq$ 10 mb for these two cases.

A significant feature of the radiative processes described in Chapter IV is the variation in the vertical distribution of the longwave and shortwave heating rates due to variations in the amount of cloud cover. The observations presented by LeMone and Pennell (1976) indicate

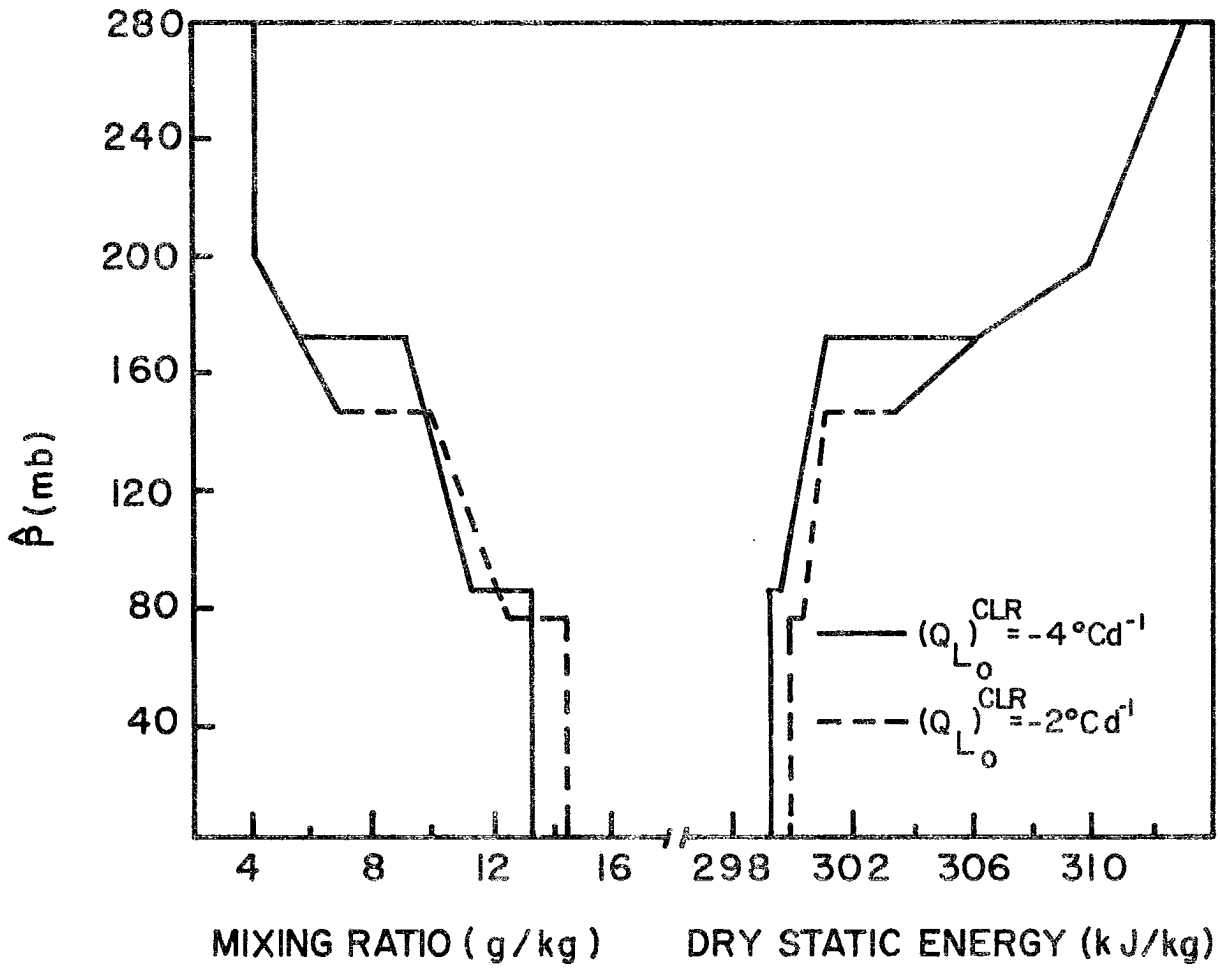

Figure 28. A steady-state model structure for values of longwave heating averaged over the entire boundary layer of -4°C day-1 and -2°C day-1.

a significant variation in the amount of trade-wind boundary-layer cloudiness. They reported cloud covers ranging from 7-70% during the aircraft measurements they made to the north of Puerto Rico. The steady-state solutions for visible cloud covers of .25 and .75 are shown in Fig. 29. The differences in the model structure are not extremely large, however, the effect of cloud top cooling on varying the height of the inversion is evident. The larger cloud cover results in the trade inversion being approximately 15 mb higher than that obtained with a cloud cover of .25. The suppressed cloud and subcloud layer heating rates associated with the .75 cloud cover result in the cloud and subcloud layer being warmer than the structure predicted with a cloud cover of .25. The moisture profiles shown in Fig. 29 show a decrease in the cloud layer moisture as the cloud cover is increased. This decrease in moisture in the cloud layer might actually result in a decrease in cloud cover in the real atmosphere. Consequently, the results given in Fig. 29 indicate that the variation in the vertical distribution of the radiative heating due to cloud cover may act as a factor which stabilizes the amount of cloud cover in the real atmosphere. These results indicate that it would be desirable to express cloud cover as a function of the large-scale thermodynamic structure. The cloud cover, however, may not have to be specified extremely accurately. In fact, the results shown in Fig. 28 indicate that the boundary layer structure may be more sensitive to high or mid-level cloudiness which may alter the average boundary layer heating. Since the large-scale divergence field may also be modulated by the radiative effect of upper-level clouds (Albrecht and Cox, 1975) it is apparent that these clouds may have a significant effect on the boundary-layer structure.

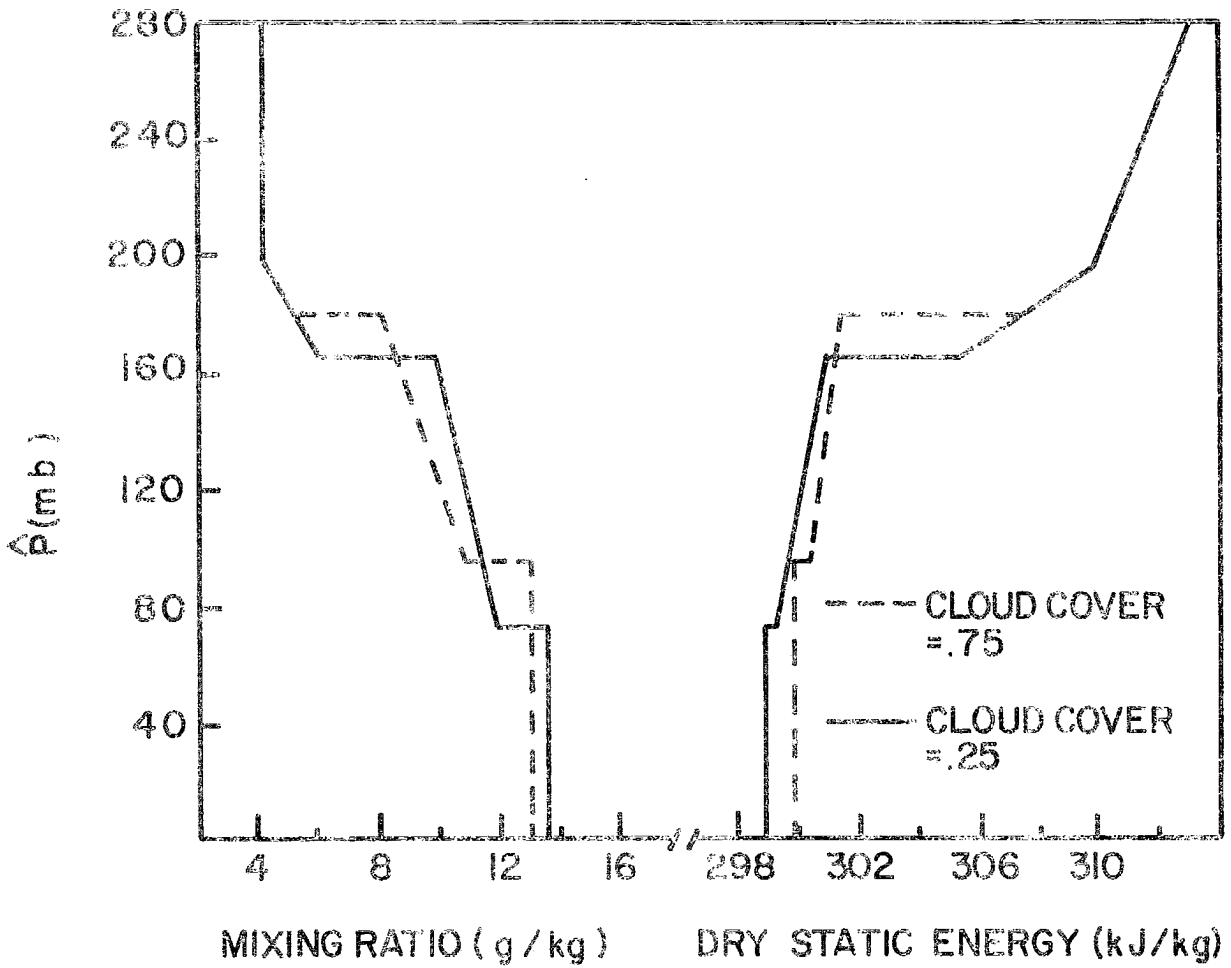

Figure 29. Same as Figure 28 but for cloud covers of .25 and .75.

The sensitivity of the model to the stabilizing-destabilizing effect of the continuum cooling is shown in Fig. 30. These steady-state solutions were calculated using the RAD I and RAD II radiation schemes outlined in Chapter IV. These results show no apparent difference in the structure for the two radiation calculations. The cloud layer moisture is such, however, that the change in stability due to radiative effects is approximately zero. Model calculations were also made to evaluate the stabilizing-destabilizing mechanism for conditions where the cloud layer is more moist. This was done by making model runs with RAD I and RAD II parameterization schemes with a sea surface temperature of 300 K. The profile of q above the inversion was increased by 2 $g \cdot kg^{-1}$ and the dry static energy was increased by 2 $kJ \cdot kg^{-1}$ for these calculations. The steady-state results obtained from this experiment are shown in Fig. 31. In this case, the destabilizing-stabilizing radiative parameterization results in a more mixed q and s profile in the cloud layer. These changes, however, are not extremely large and indicate that the convective transports dominate the control of the cloud-layer stability.

C. Formation of the Trade Inversion

The first part of this chapter concentrated on determining the sensitivity of the steady-state model solutions to the specification of various parameters. In the remainder of this chapter time varying solutions of the boundary layer model will be considered.

Prior to steady-state conditions the numerical integrations described above illustrate how the inversion might reform in the wake of disturbed conditions. The basic model structure after 2, 4, and 8 h of integration are shown in Fig. 32a for the basic model parameters

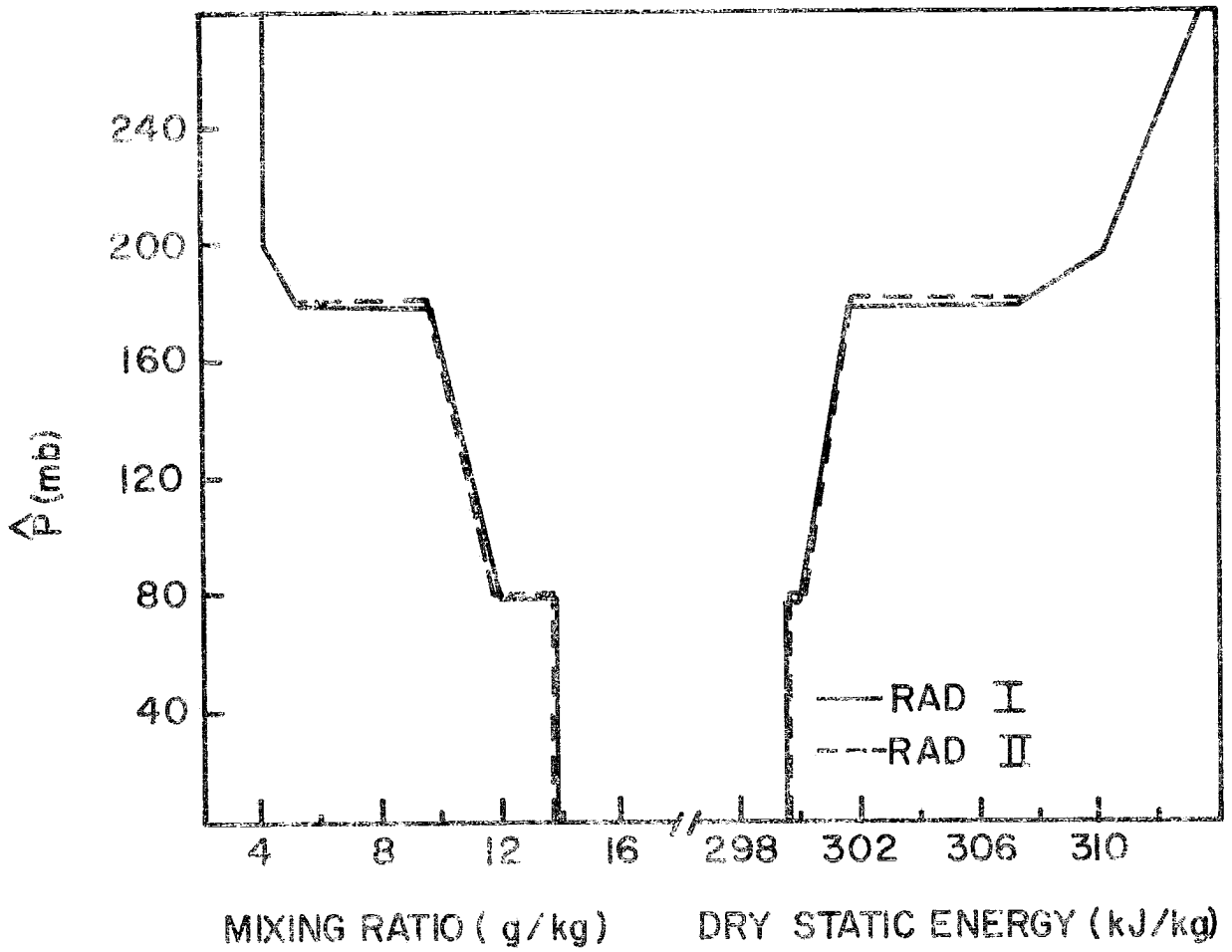

Figure 30. A comparison of steady-state model structure for radiation scheme I, uniform heating below the inversion, and radiation scheme II for non-uniform heating below the inversion.

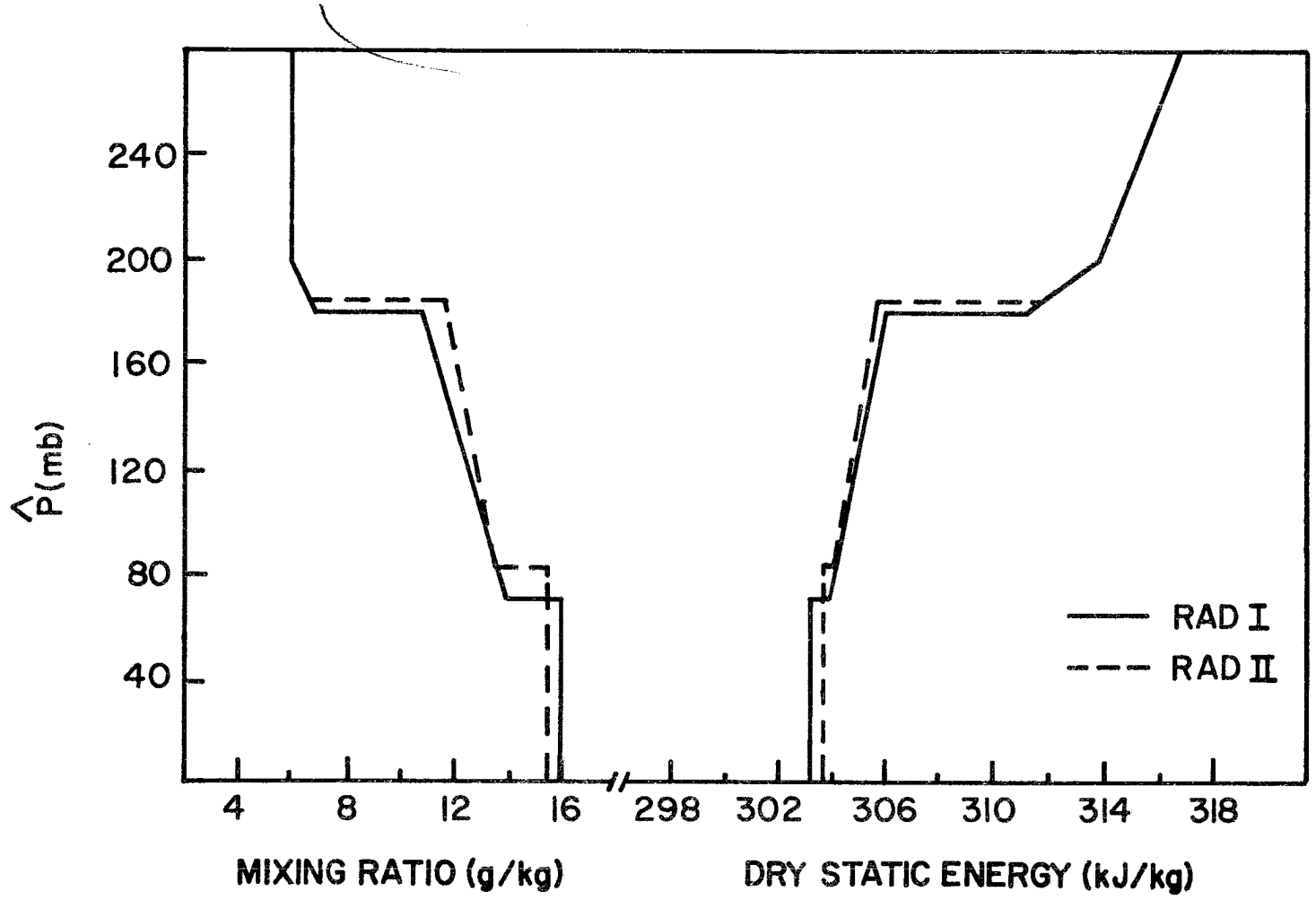

Figure 31. Same as Figure 30 but for more moist conditions.

described above. The cloud layer begins to form in the model after one hour of integration. After this the trade inversion rises quickly while cloud base also rises but much less quickly. After only 4 h the trade inversion reaches a height of ≈ 120 mb which is ≈ 70% of the steady-state height. The mixing ratio and dry static energy profiles after 8, 16, 32 and 64 h of integration are shown in Fig. 32b. After 64 h the time variation of the structure becomes very small. The variation of all variables as a function of time are shown in Fig. 33. It is important to note that the time-dependent results presented above are not intended to represent a specific case. They do, however, illustrate in general how the model may be used to predict the time variation of the boundary layer structure in the wake of disturbed conditions. While there has been some uncertainty about the origin of the trade inversion, these results indicate that the inversion can easily form from a shallow mixed layer in less than 1/2 day.

The recovery time for the reformation of the trade inversion may also depend on the specification of the various parameters discussed previously. This is illustrated in Fig. 34 where the height of the trade inversion and cloud base are shown as a function of time for a sea surface temperature of 299 and 297 K. The increased inversion height for the warmer sea surface temperature noted in the steady-state solution actually occurs during the first 6 h of the integration. A similar effect is shown in Fig. 35 for the results obtained with different surface wind velocities.

The steady-state solutions presented above show that the height of the inversion varies significantly with the large-scale divergence values. The initial growth rate, however, as shown in Fig. 36, does not

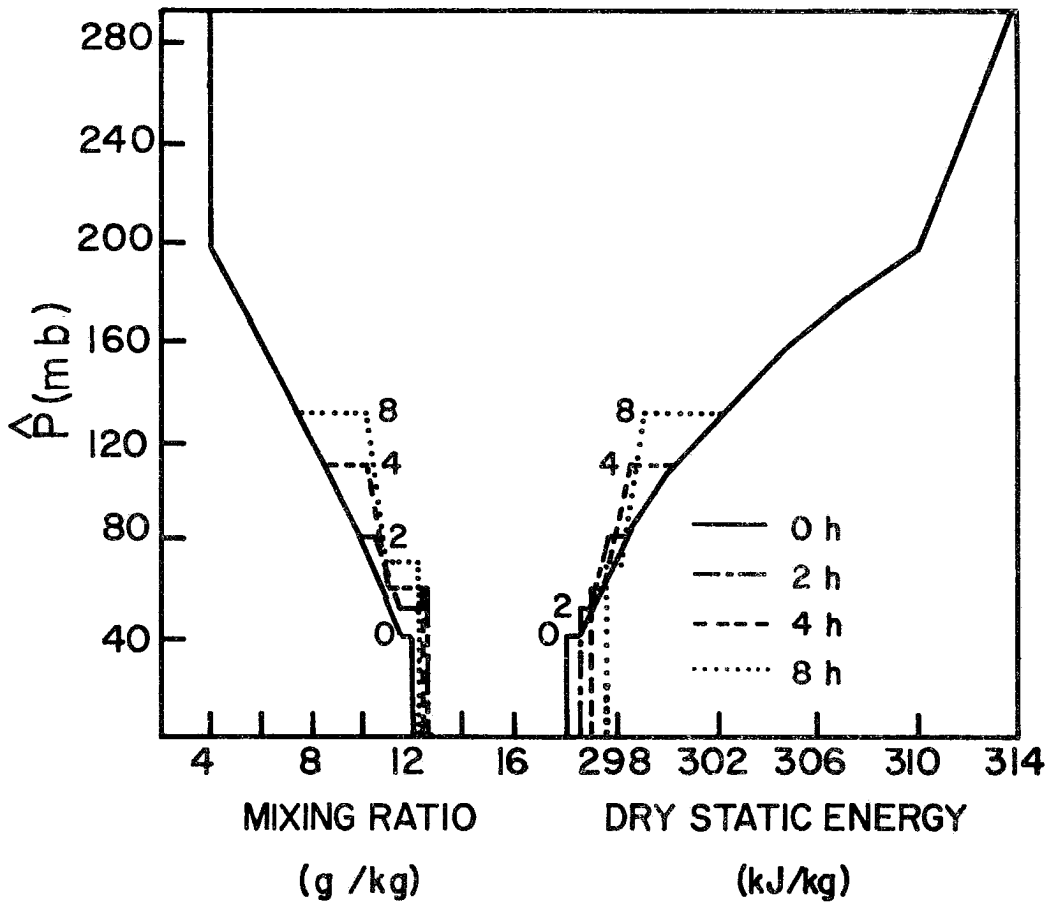

Figure 32a. Model structure obtained after (a) 0, 1, 2, 4 h of integration.

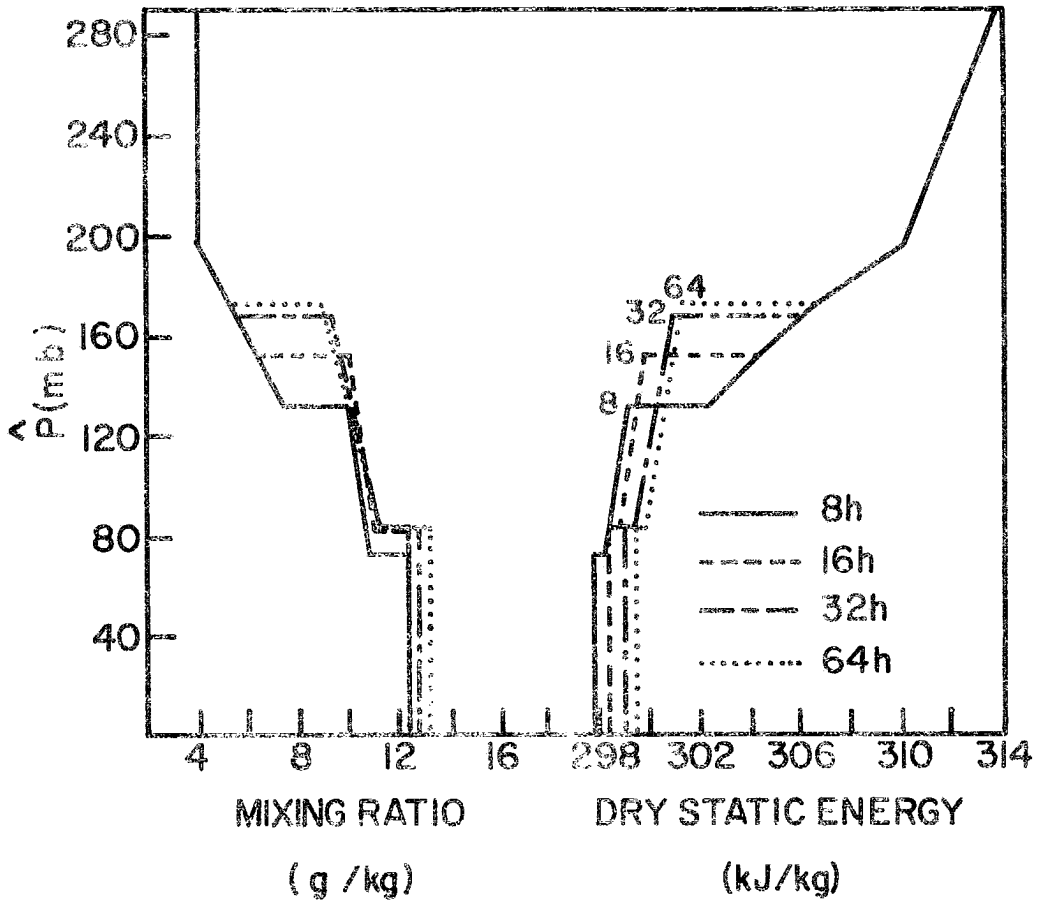

Figure 32b. Model structure obtained after (b) 8, 16, 32, and 48 h of integration.

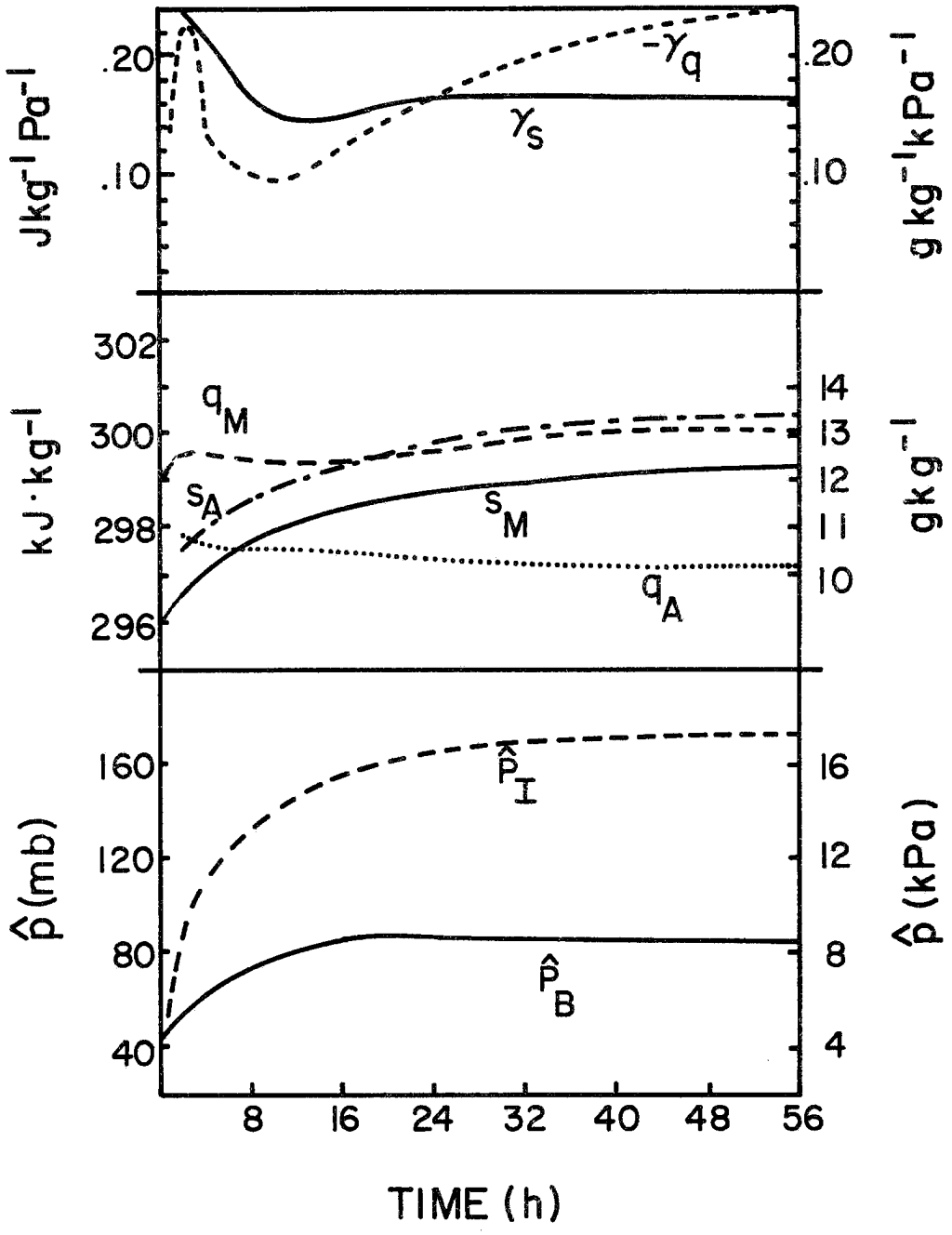

Figure 33. Variation of model variables as a function of time.

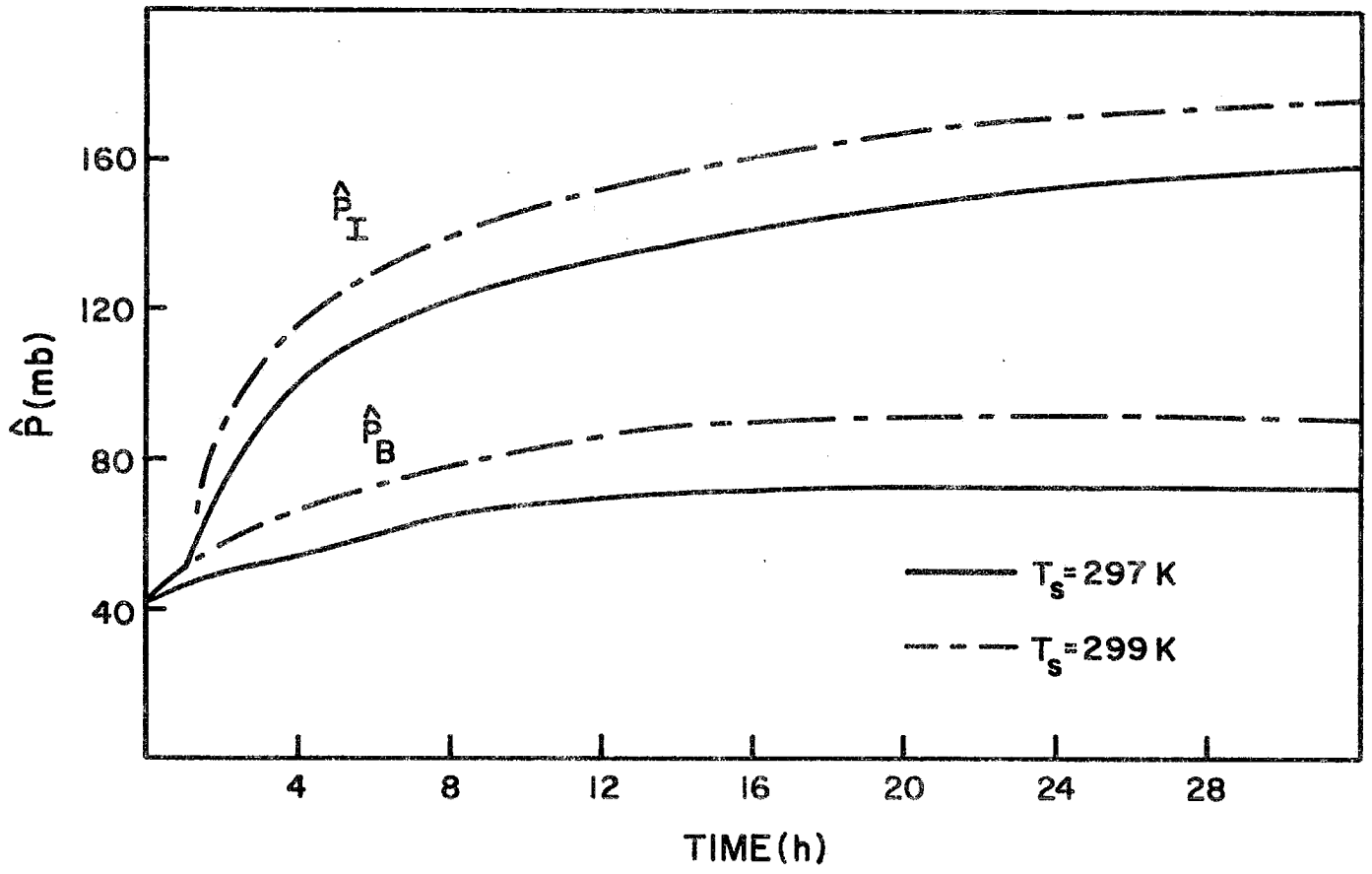

Figure 34. Inversion and cloud base height predicted as a function of time for a sea surface temperature of 297 K and 299 K.

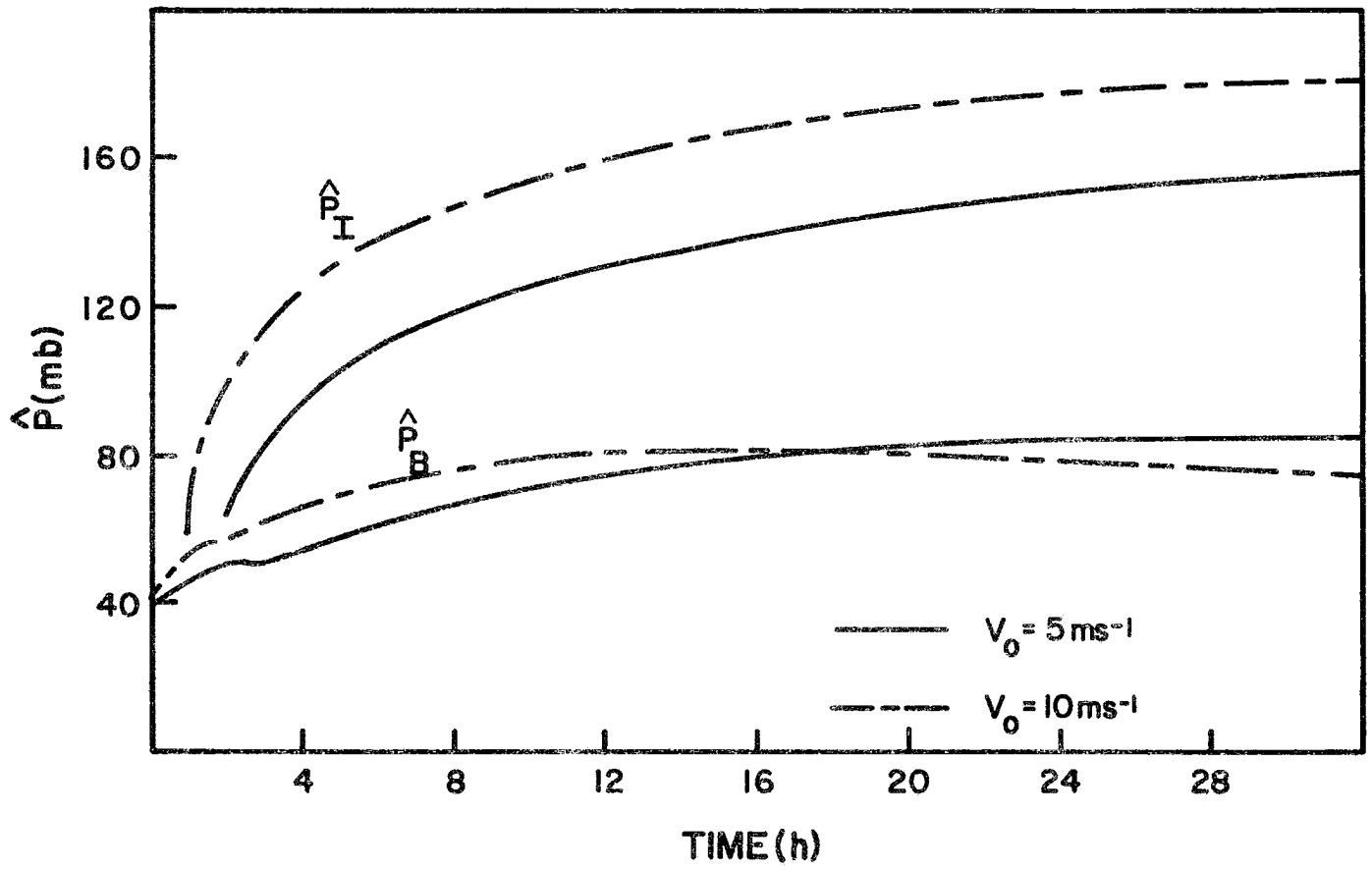

Figure 35. Same as Figure 34 but for surface wind speeds of 10 and 5 ms^{-1}.

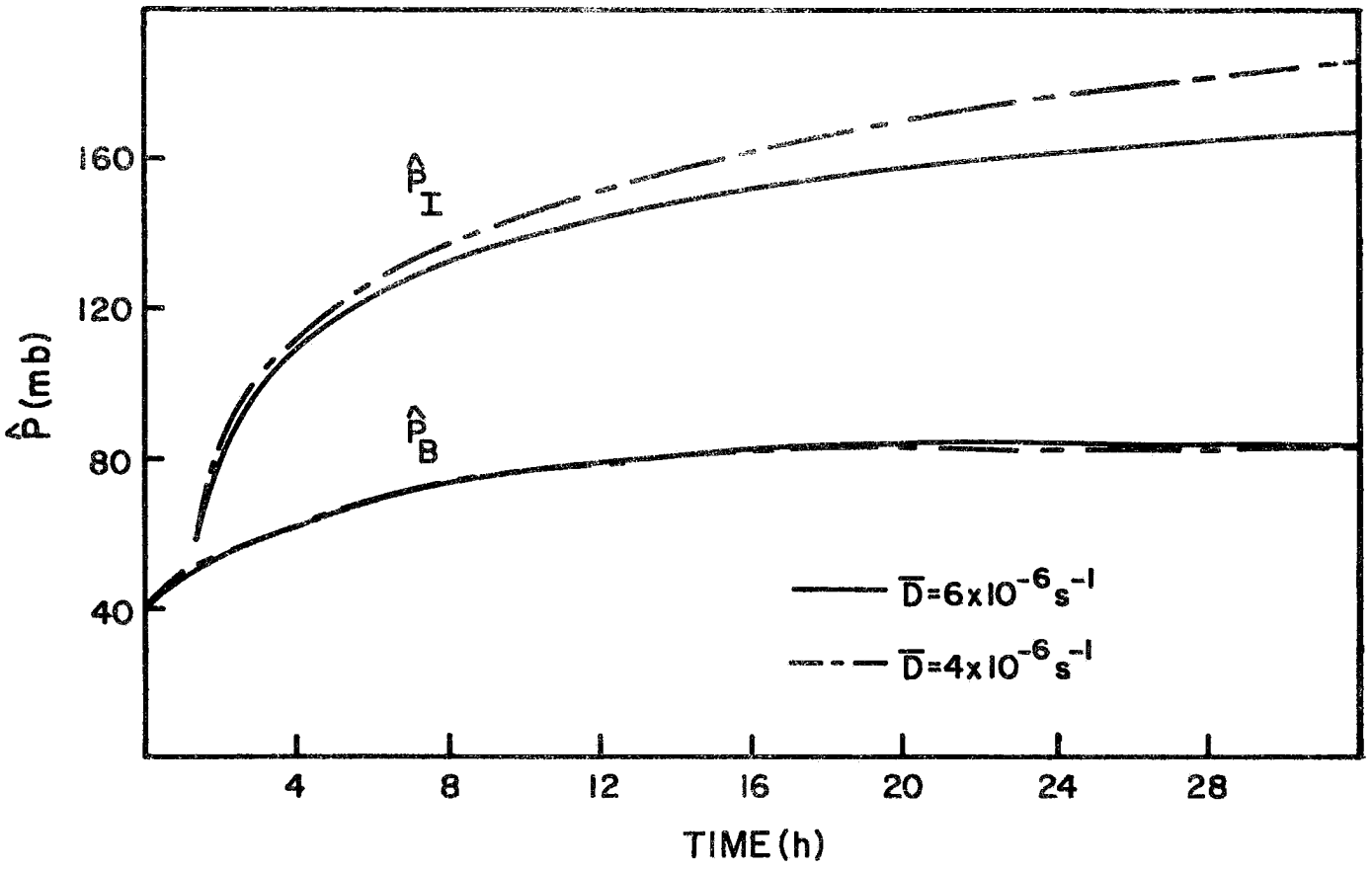

Figure 36. Same as Figure 34 but for a large-scale divergence of $4X10^{-6}$ s^{-1} and $6X10^{-6}$ s^{-1}.

very significantly with the large-scale divergence. The solutions, however, approach the steady-state solution more quickly with the larger divergence values. The time variation of cloud base and inversion height with $D = 3.5 \times 10^{-6}$ s^{-1} and $f(z) = \cos(\pi z/2h)$ are shown in Fig. 11. Initially the rise from large-scale divergence dominates and the inversion rises rapidly. Later the moistening of the boundary layer by the entrainment of the moist cloud air overcomes the drying effect of the large-scale divergence, and the inversion begins to descend slowly.

The results presented in this section illustrate that the surface fluxes strongly influence the initial growth rate of the boundary layer, but subsequently the accurate specification of cloud top entrainment, the details of atmospheric structure, and surface moisture flux are important in the realistic modelling of the boundary layer.

5. Diurnal variations

The results presented above indicate that the height of the inversion is sensitive to the boundary-layer surface moisture flux. It is therefore quite reasonable to assume that there should be a diurnal variation in the height of the inversion. However, since the height of the inversion depends on other factors, it may be difficult to observe such a diurnal variation. Augstein et al. (1974) plotted the inversion height as a function of time from all the data collected from the three ships which participated in GATE. This analysis demonstrated clear diurnal variations in the inversion height over periods of a few days. An example of these variations are shown in Fig. 12 where the height of the base of the inversion, as observed from the ship meteorological buoy, is shown as a function of time. As demonstrated by the analysis given by Augstein et al. (1974), the top of the inversion during this period moved with the same amplitude and phase. The fundamental features of the results given

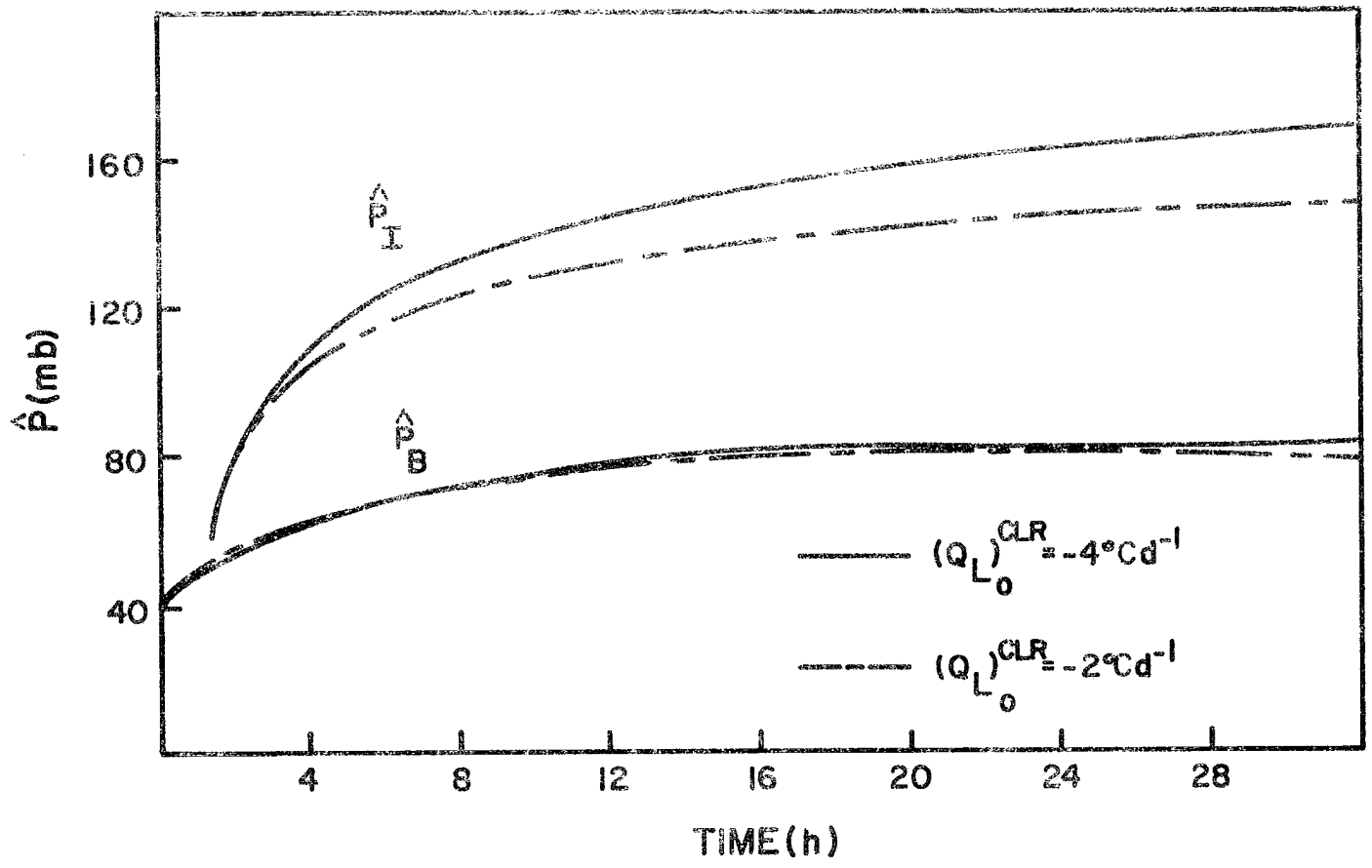

Figure 37. Same as Figure 34 but for $(Q_L)_o^{CLR}$ of -2°C day^{-1} and -4°C day^{-1}.

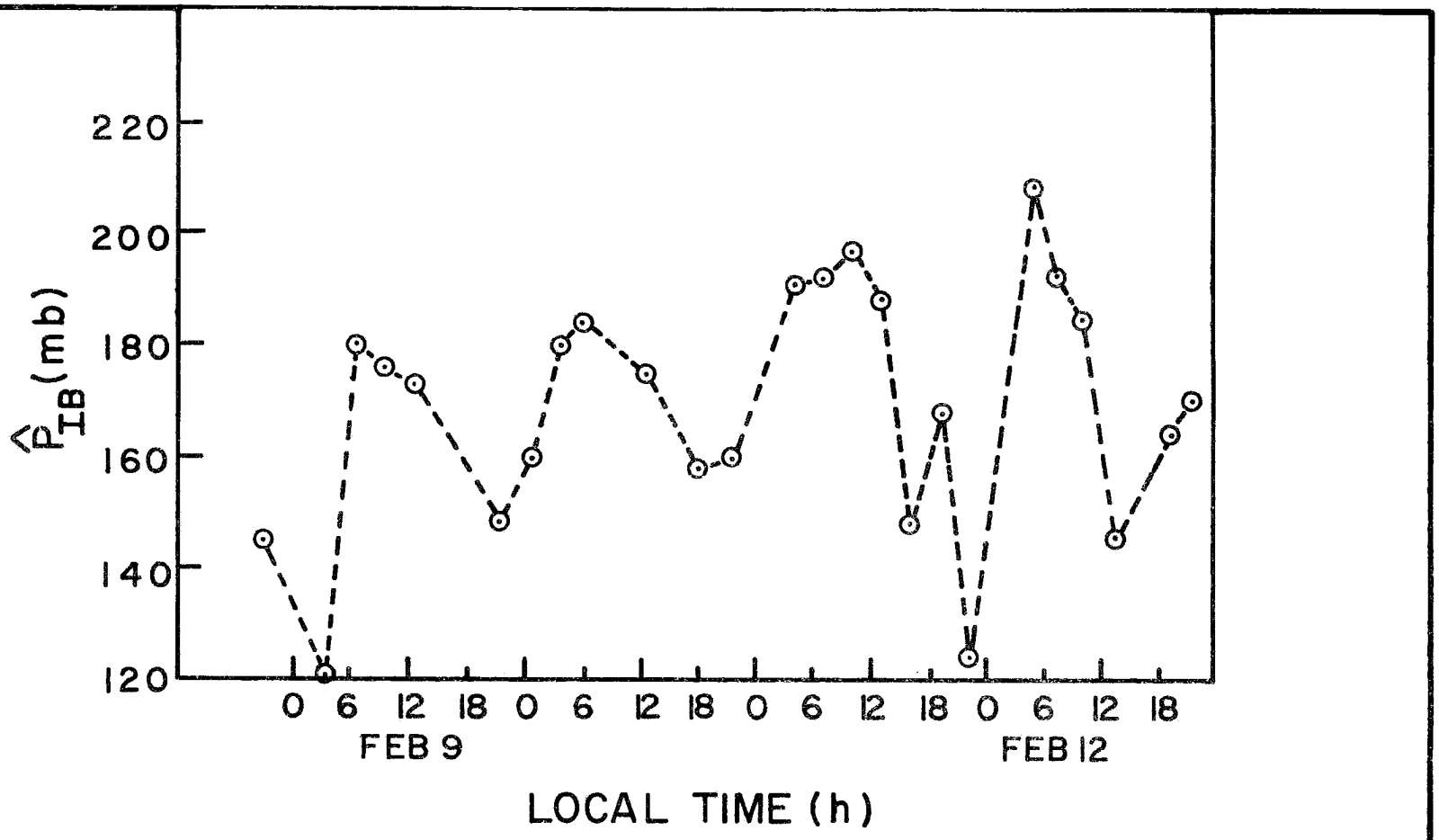

Figure 38. Time variation of the base of the trade inversion, $\hat{p}_{IB}$, observed from the ship Meteor during ATEX from Feb. 9-12, 1969.

in Fig. 38 is the obvious diurnal variation of the inversion height. The inversion has a relative maximum at 600 LT on each of the four days and an apparent minimum between 1200 and 1800 LT. The amplitude of the variation is ≈ 20 mb.

The response of the model structure to a diurnally varying solar heating rate was determined. The exact form of the heating is given by (IV.4). The same total absorption was assumed for the cloud and clear regions although the absorption in the cloud region occurs in the infinitesimally thin iversion layer. For the diurnal results presented here the model calculation was initialized with the basic model results obtained after 60 h of integration. The results given below were obtained during the period 48-72 h after the diurnal heating is initially applied. The height of the inversion and the height of cloud base are shown in Fig. 39 for the diurnally varying solar heating. The phase of the response agrees remarkably well with the observed variation. The amplitude of the variations predicted by the model, however, is 5 mb while that observed is significantly greater. It was pointed out, however, in Chapter IV that the absorption of solar radiation by clouds may in some conditions be larger than that assumed here.

The diurnal variations in the height of the inversion may also be due to a diurnal variation in the large-scale subsidence field. Nitta and Esbensen (1974) noted a significant diurnal variation in the large-scale divergence field for the BOMEX undisturbed period. The magnitude of the diurnally varying divergence field observed by Nitta and Esbensen was significantly greater than that obtained by Lindzen (1967) for the solar tide. The results of both Nitta and Esbensen and of Lindzen indicated a maximum divergence at ≈ 600 LT.

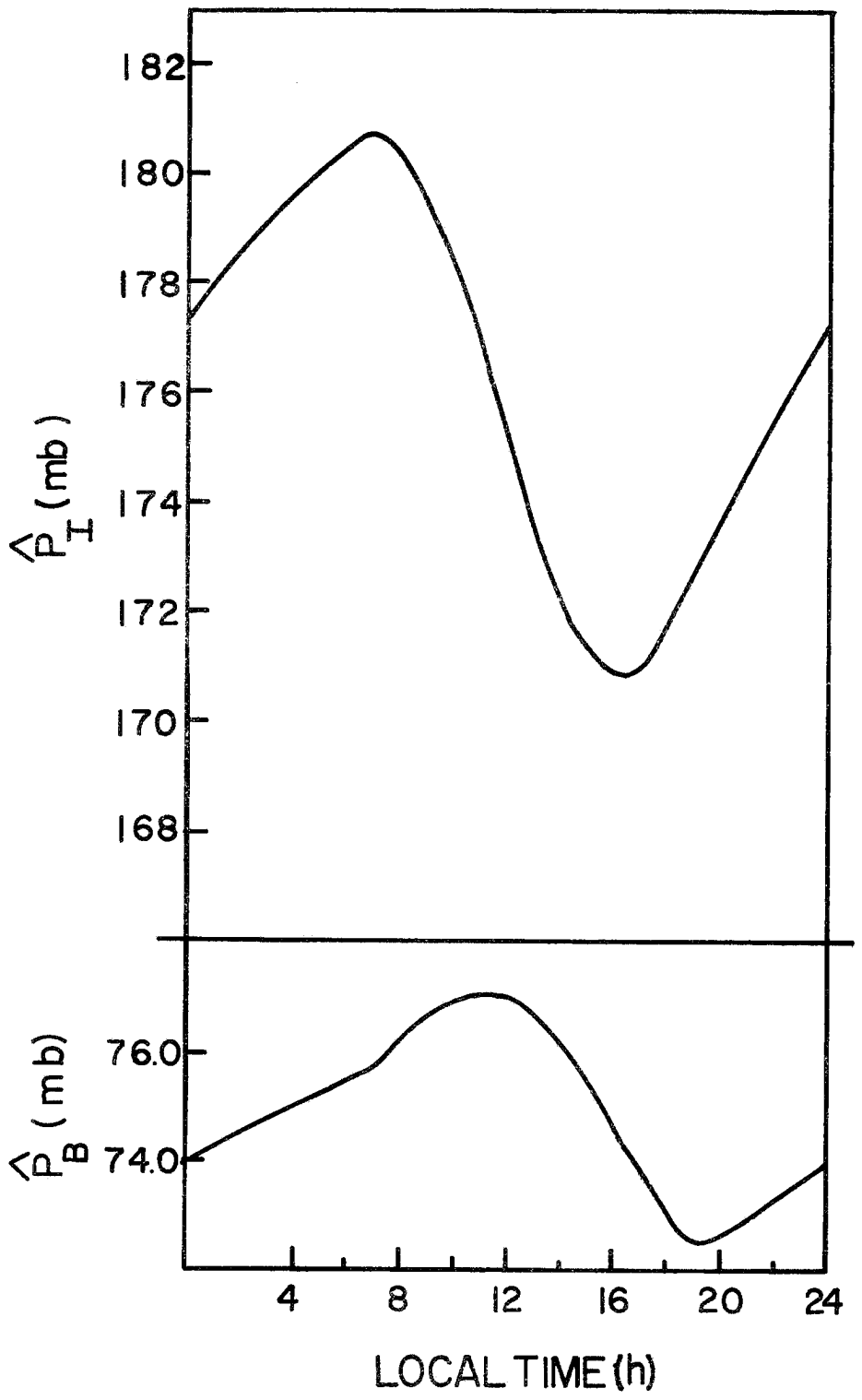

Figure 39. Time variation of the cloud base and inversion height predicted with a diurnally varying solar heating rate.

The vertical motion required to balance the solar radiation above the inversion (assuming the stability shown in Fig. 1) would require a diurnally varying divergence field with an amplitude of $\simeq 2X10^{-6}$ sec^{-1}. This amplitude is approximately the same as that determined observationally by Nitta and Esbensen. The response of the model to a diurnally varying (assumed to be sinusoidal with time) divergence field of this magnitude is shown in Fig. 40. For these results the amplitude of the sinusoidal divergence field was assumed to be $2X10^{-6}$ sec^{-1} with the maximum divergence occurring at 600 LT. The amplitude of the response is $\simeq$ 5 mb and the phase differs from that observed by 6 hours.

The possible interaction of the effect of a diurnally varying divergence field and a boundary layer heating is illustrated in Fig. 41. The hour of maximum divergence for these calculations was specified at 00, 600 and 1200 LT. The amplitude and phase of the response obtained with the maximum divergence at 1200 LT agrees reasonably well with the observations. This divergence field is, however, $\simeq$ 6 h out of phase with that given by Lindzen (1967) and Nitta and Esbensen (1974).

E. Simulation of Stratocumulus Conditions

An interesting aspect of the boundary layer model described above is that it may be used with slight modification to simulate conditions where the cloud layer is saturated. If it is assumed that the liquid water which is present in saturated conditions is carried with the large-scale motions, the budget equations developed in Chapter II actually apply to the total water, $q+\ell$. The equations for moist static energy, h, remain unchanged and the corresponding equations for dry static energy represent changes in the quantity $s-L\ell$.

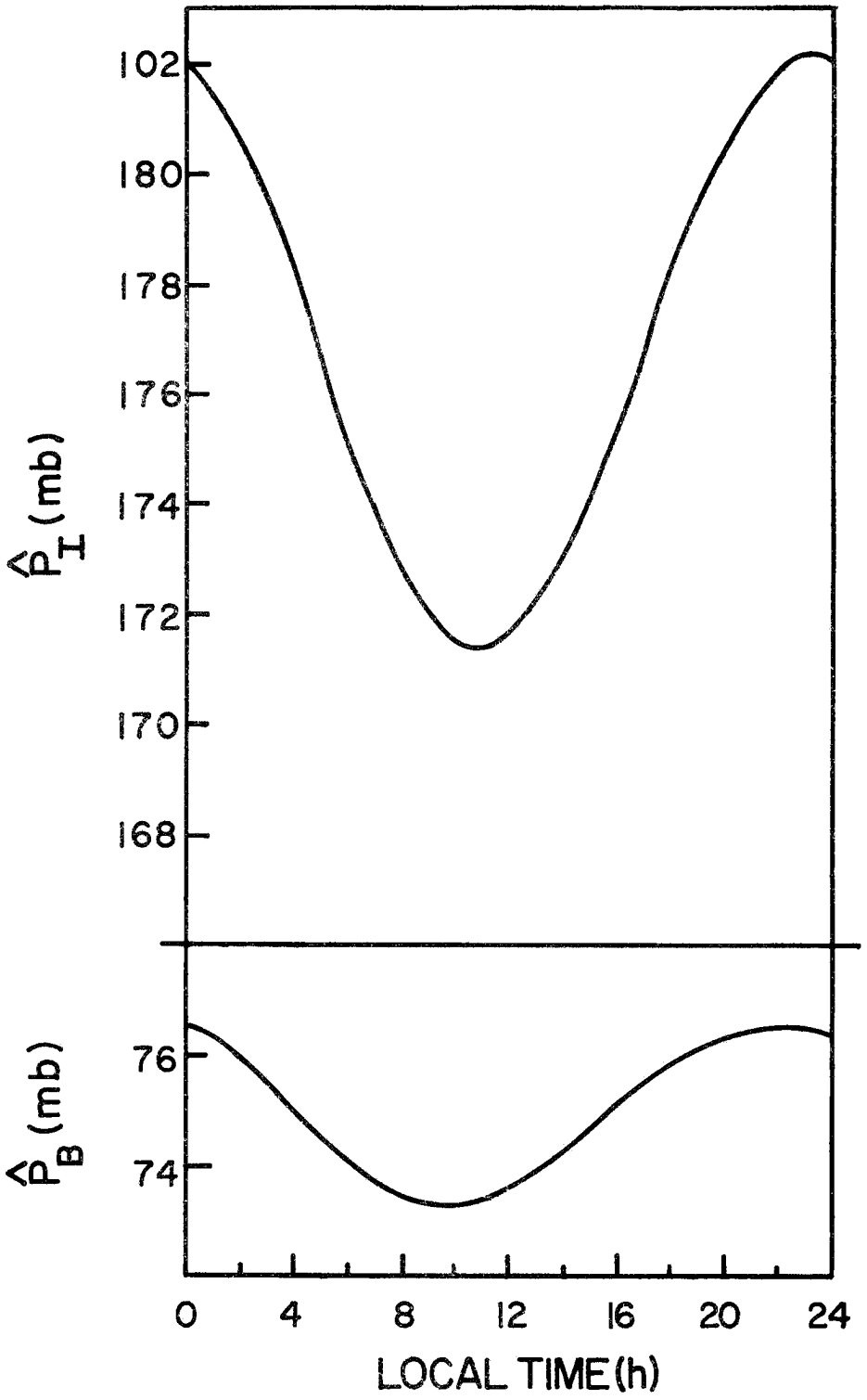

Figure 40. Same as Figure 39 but a diurnally varying divergence field where the maximum divergence occurs at 600 LT.

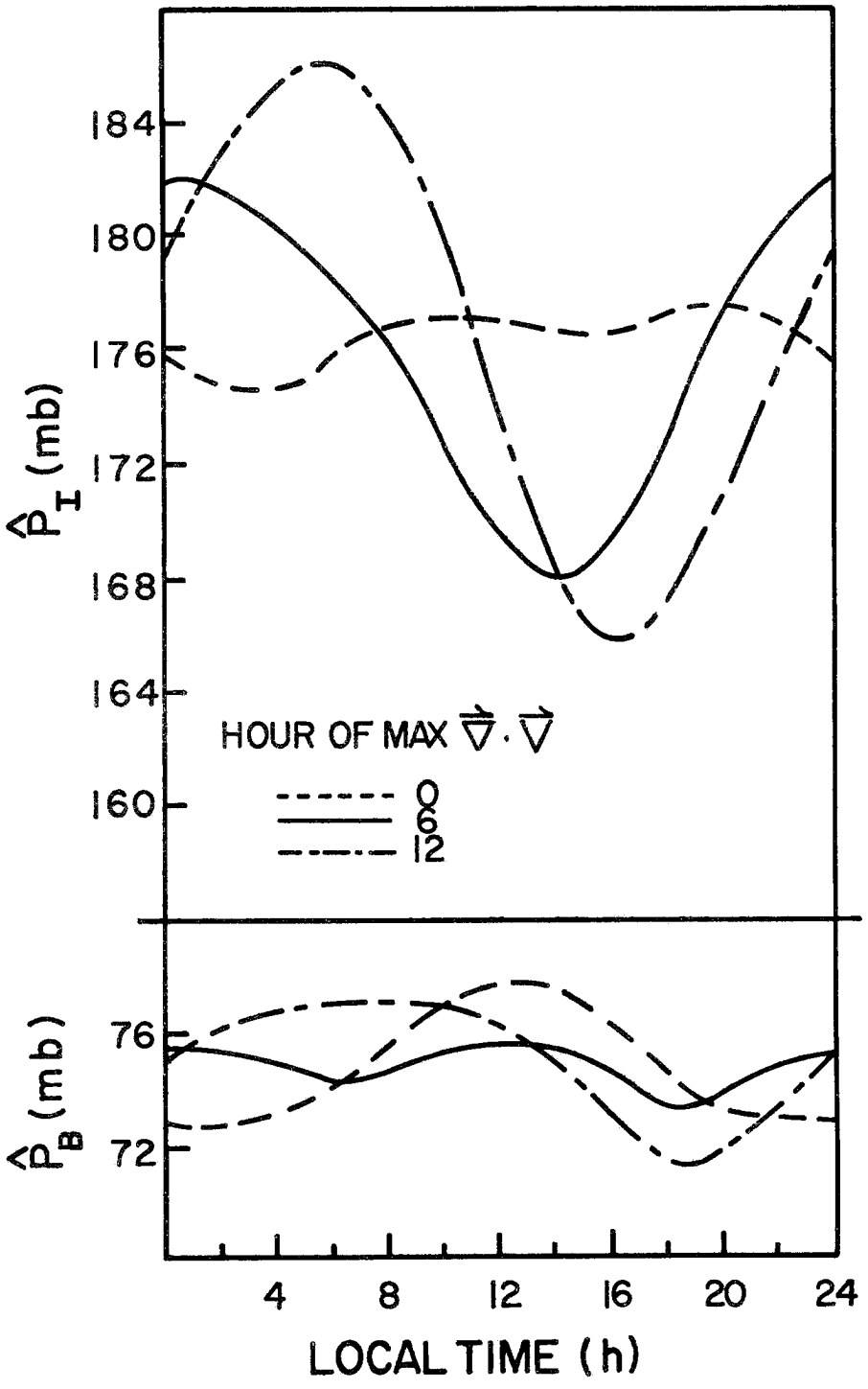

Figure 41. Time variation of cloud base and inversion height predicted by the model with a diurnally varying solar heating rate and a diurnally varying large-scale divergence field. The three cases shown correspond to the maximum divergence occurring at 00, 600 and 1200 LT.

The buoyancy constraint discussed in Chapter III is also altered slightly since the cloud-environment difference in virtual dry static energy is given as

$$s_{vc} - \bar{s}_v = \beta (h_c - \bar{h}) - \varepsilon' L(q_c + \ell_c - \bar{q} + \bar{\ell}) \qquad (V.2)$$

in the regions where the environment is saturated. The entrainment relationships remain valid for the determination of the cloud environment differences shown in (V.2). Consequently, the entrainment factor may still be determined from the buoyancy constraint. In this case, however, the integration over the depth of the cloud layer is evaluated as the sum of the integrations over the saturated and unsaturated portions of the cloud layer.

The model results obtained with the model when the cloud layer is saturated is compared to the results obtained by Schubert (1976) using the stratocumulus model described by Lilly (1968). To make this comparison boundary conditions and parameters similar to those specified by Schubert are assumed. The conditions and parameters assumed are presented in Table X. Parameters not specifically noted in Table X are the same as those specified previously. The parameters shown in Table X do differ slightly from those assumed by Schubert (1976) since his results were obtained by assuming no radiative cooling below the inversion layer. The solutions described here, however, are not stable when the boundary layer radiative heating is zero.

BOUNDARY CONDITIONS

a) Surface Parameters

i) $p_o = 102.20$ k·Pa (1022 mb)

ii) $T_o = 13°C$

b) Profiles Specified Above Inversion

i) $h(\hat{p}) = 313.95\ (kJ \cdot kg^{-1}) + .251 (J \cdot kg^{-1}\ Pa^{-1})\ \hat{p}$

ii) $q(\hat{p}) = 3.3\ g \cdot kg^{-1} - .043 X 10^{-3} (g \cdot kg^{-1} \cdot Pa^{-1})\ \hat{p}$

SPECIFIED PARAMETERS

a) Large-Scale Parameters

$\bar{D} = 5.0 X 10^{-6}\ s^{-1}$

b) Convective Parameters

i) $k = .25$

ii) $\Delta T_o = .5°C$

iii) $\delta q = 0.0$

iv) $\tau_{adj} = 1/3$ day

c) Radiative Parameters

$(F_R)_{I-} = (F_R)_{I+} - 65.65\ Wm^{-2}$

$(F_R)_o = (F_R)_{I-} - \frac{c_p}{g} \hat{p}_I\ (.40°C\ d^{-1})$

$(F_R)_B = (F_R)_{I-} - \frac{c_p}{g} \delta\hat{p}\ (.40°C\ d^{-1})$

$(F_R)_A = [(F_R)_{I-} + (F_R)_B]/2$

Table X. A summary of boundary conditions used for simulation of stratocumulus conditions.

The initial conditions assumed for the simulation are shown in Fig. 42 and consist of a cloud layer which is initially unsaturated. For simplicity, the radiative heating is specified to be constant with time. However, in actuality the radiative heating may change since the cloudiness would vary from broken cloudiness to complete overcast as the cloud layer becomes saturated.

As the model is integrated from the initial conditions shown in Fig. 42 the top part of the layer does become saturated after ≈ 30 h of integration. The model results obtained after 60 h of integration are compared with the steady-state results of Schubert (1976) in Fig. 42. The agreement is excellent and the slight differences which do exist between these model results may be explained in terms of the differences in the assumed model structure. The parameter $\hat{p}_c$ shown in Fig. 42 represents the level in the models where the environment becomes saturated. The model fluxes which correspond to the structure shown in Fig. 42 are shown in Fig. 43. There is good agreement between the fluxes of these two models.

The difference between the results obtained with Lilly's model and the model described above are consistent with the differences in the structures assumed for each model. The small amount of radiative cooling assumed for the trade-cumulus model is consistent with the fact that the structure predicted with this model is slightly cooler than the structure obtained with Lilly's model. In Lilly's model, the thermodynamic variables are assumed to be well mixed with height. Consequently, there is no distinction between the height of cloud base and the level where the environment becomes saturated. In the trade-cumulus model the updrafts are assumed to have the properties of the subcloud

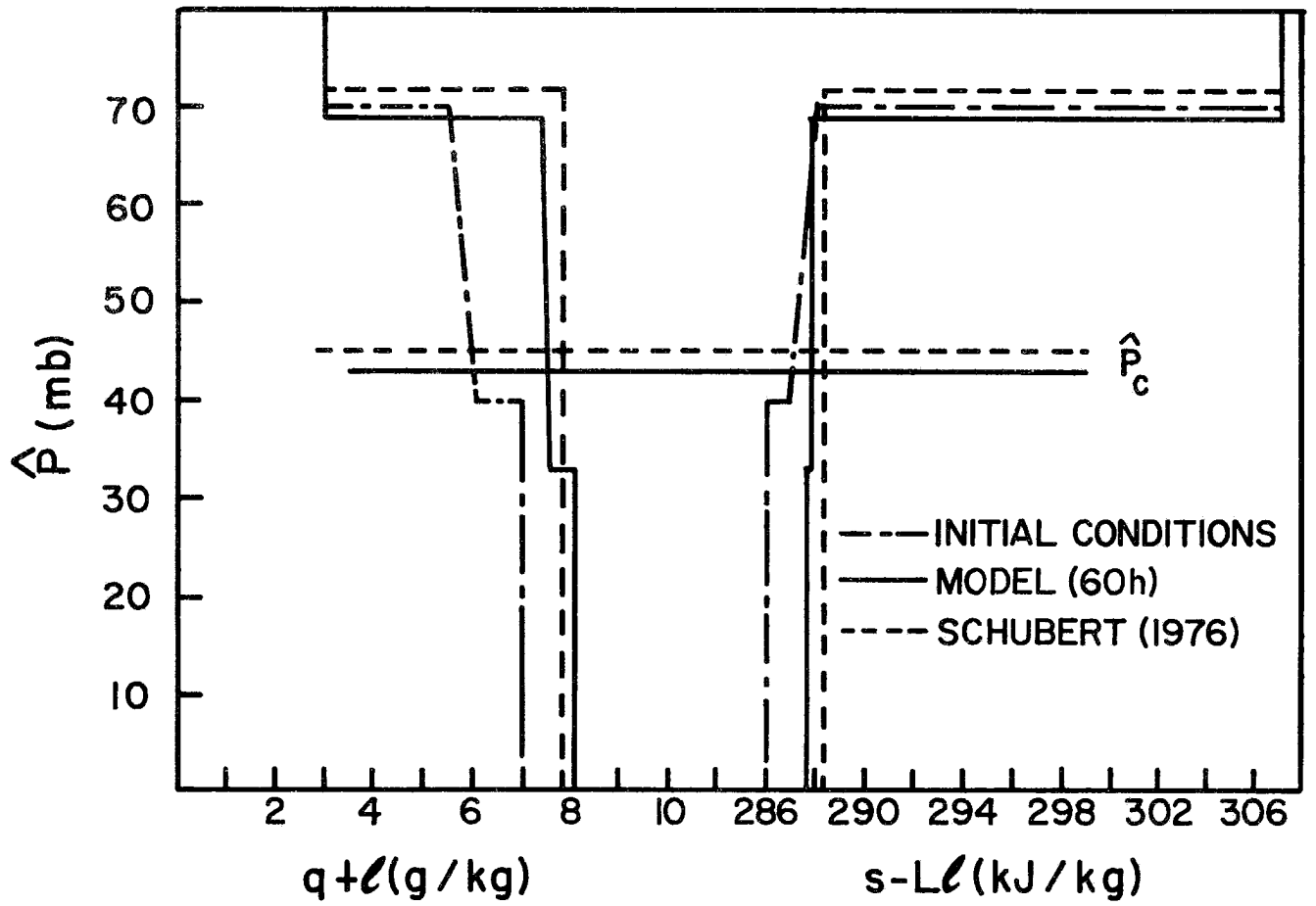

Figure 42. Initial conditions, model results after 60 h of integration and results given by Schubert (1976) for stratocumulus conditions.

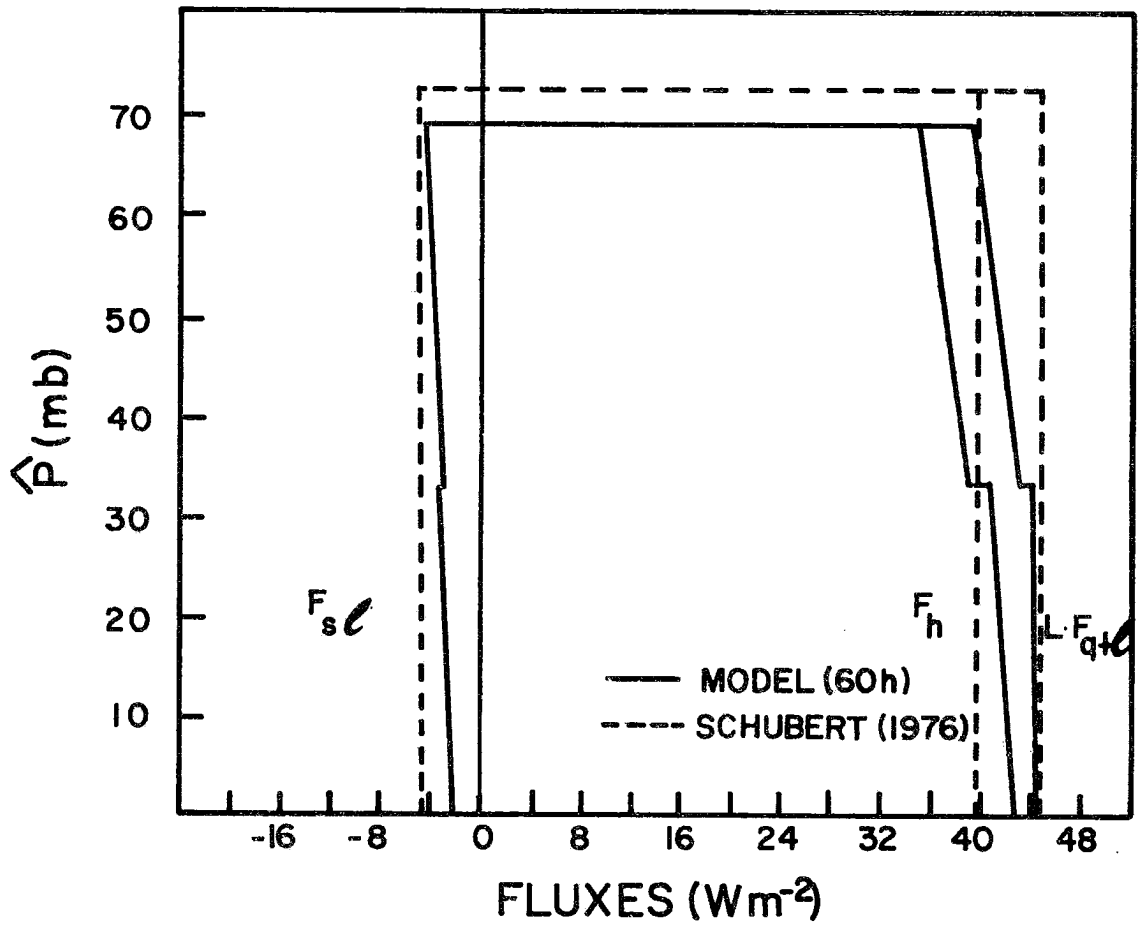

Figure 43. A comparison of model fluxes with fluxes calculated by Schubert (1976) for stratocumulus conditions.

layer. Since there is a small jump in the thermodynamic variable at the transition layer, cloud base occurs below the level where the environment becomes saturated. In the cloud layer there is a slight lapse rate of the thermodynamic variables and some radiative cooling for the trade-cumulus model. Consequently, for steady-state conditions the fluxes vary slightly with height. In Lilly's model, however, the fluxes are constant with height for steady-state conditions.

The time-dependent behavior of the two models was also compared. This was done by assuming a diurnally varying discontinuity in the radiative fluxes at cloud top of the same form assumed by Schubert (1976). This form is given as

$$(\Delta F_R) = 90.0 - 69.77 \max \left\{ \begin{matrix} 0.202 + 0.779 \cos \left(2\pi \frac{t-12}{24}\right) \\ 0 \end{matrix} \right\}$$

where t is local time in hours and (ΔF_R) is in Wm^{-2}. The pressure level of the inversion and the level of cloud base as a function of time obtained by Schubert (1976) for this forcing function are shown in Fig. 44a. These results were obtained with a sea surface temperature of 13°C and a large-scale divergence of $5X10^{-6}$ s^{-1}. The equivalent results obtained with the "trade-cumulus" model are shown in Fig. 44b. These results show remarkable agreement in both phase and amplitude of the heights predicted by the model. The fluxes corresponding to the results shown in Fig. 44 are shown in Fig. 45 and also indicate good agreement in the phase and amplitude of the variations as a function of time.

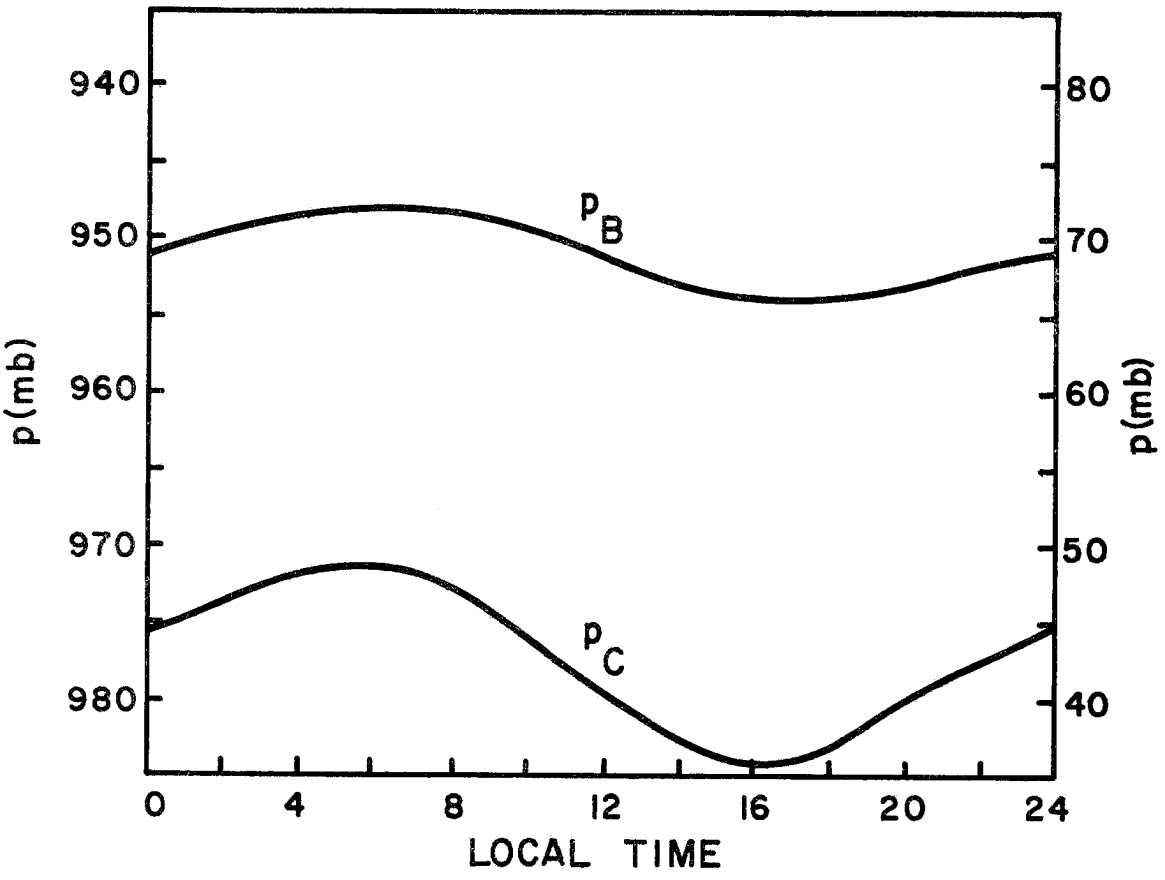

Figure 44a. Diurnal variation of the inversion (p_B) and cloud base height (p_C) predicted by Schubert (1976) for a sea surface temperature of 13°C and large-scale divergence of $5X10^{-6}$ s^{-1}. The symbol p_B in Schubert's notation is the pressure level of the inversion.

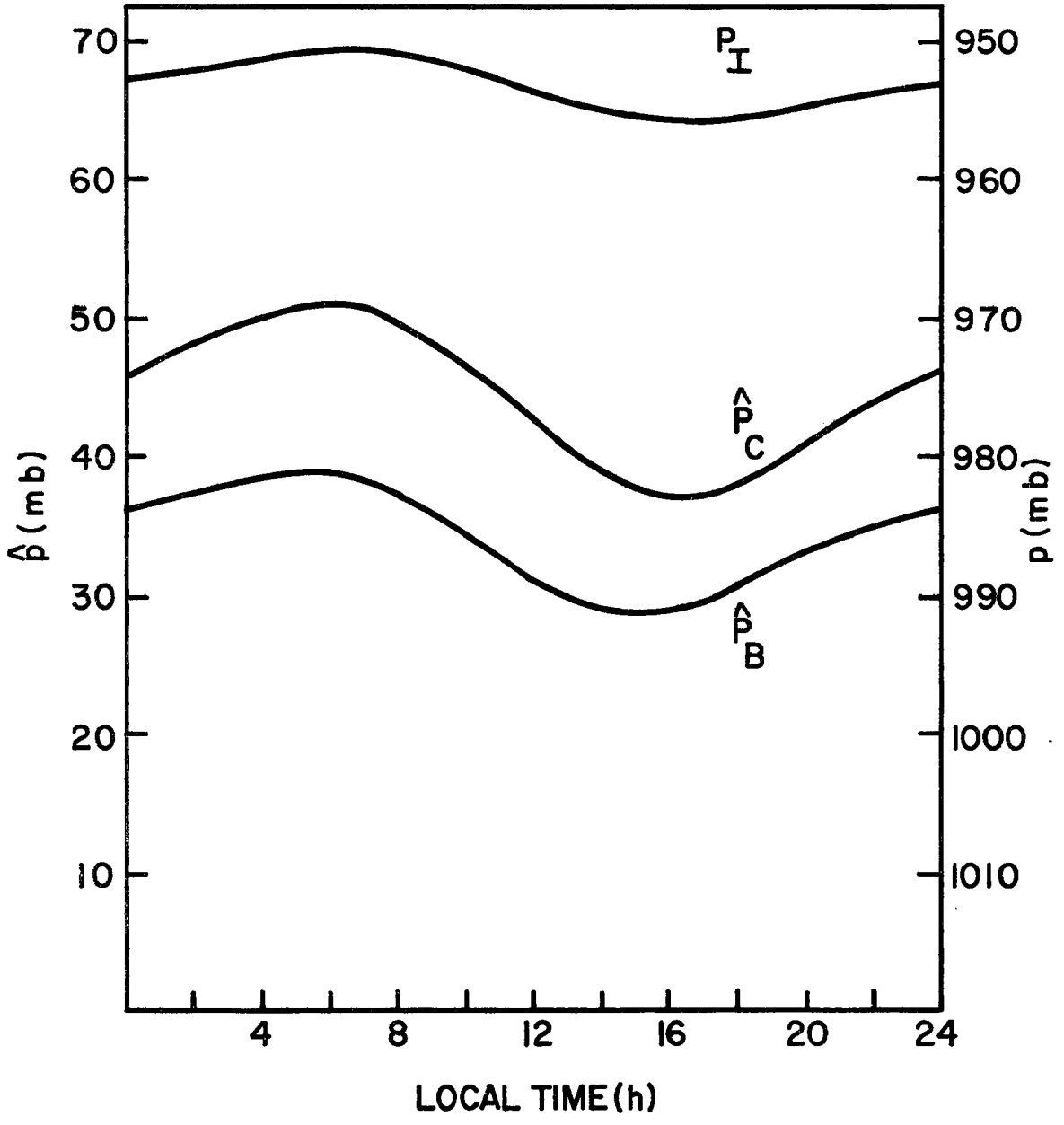

Figure 44b. Results obtained with "trade cumulus" model for same conditions as Figure 44a.

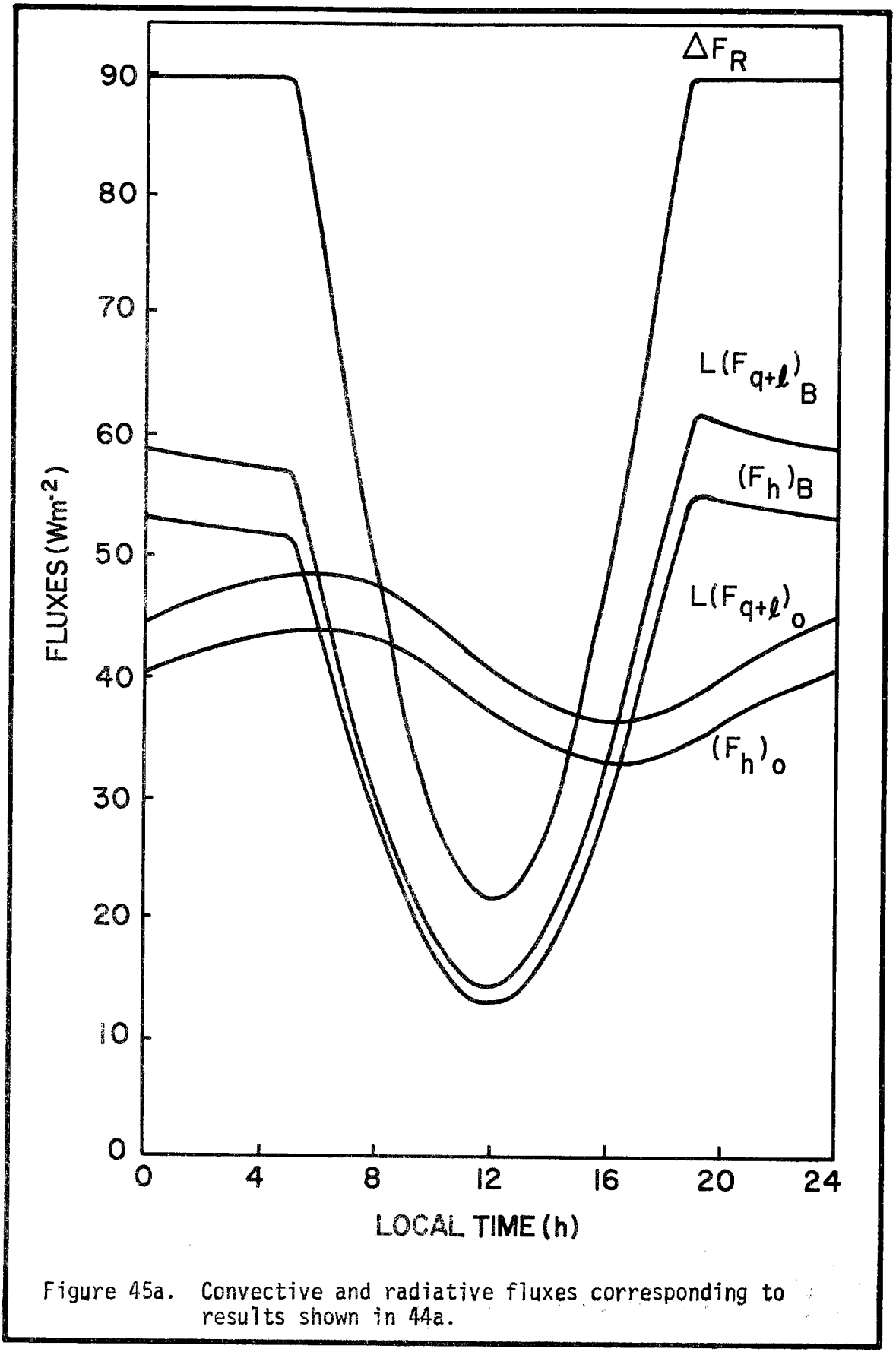

Figure 45a. Convective and radiative fluxes corresponding to results shown in 44a.

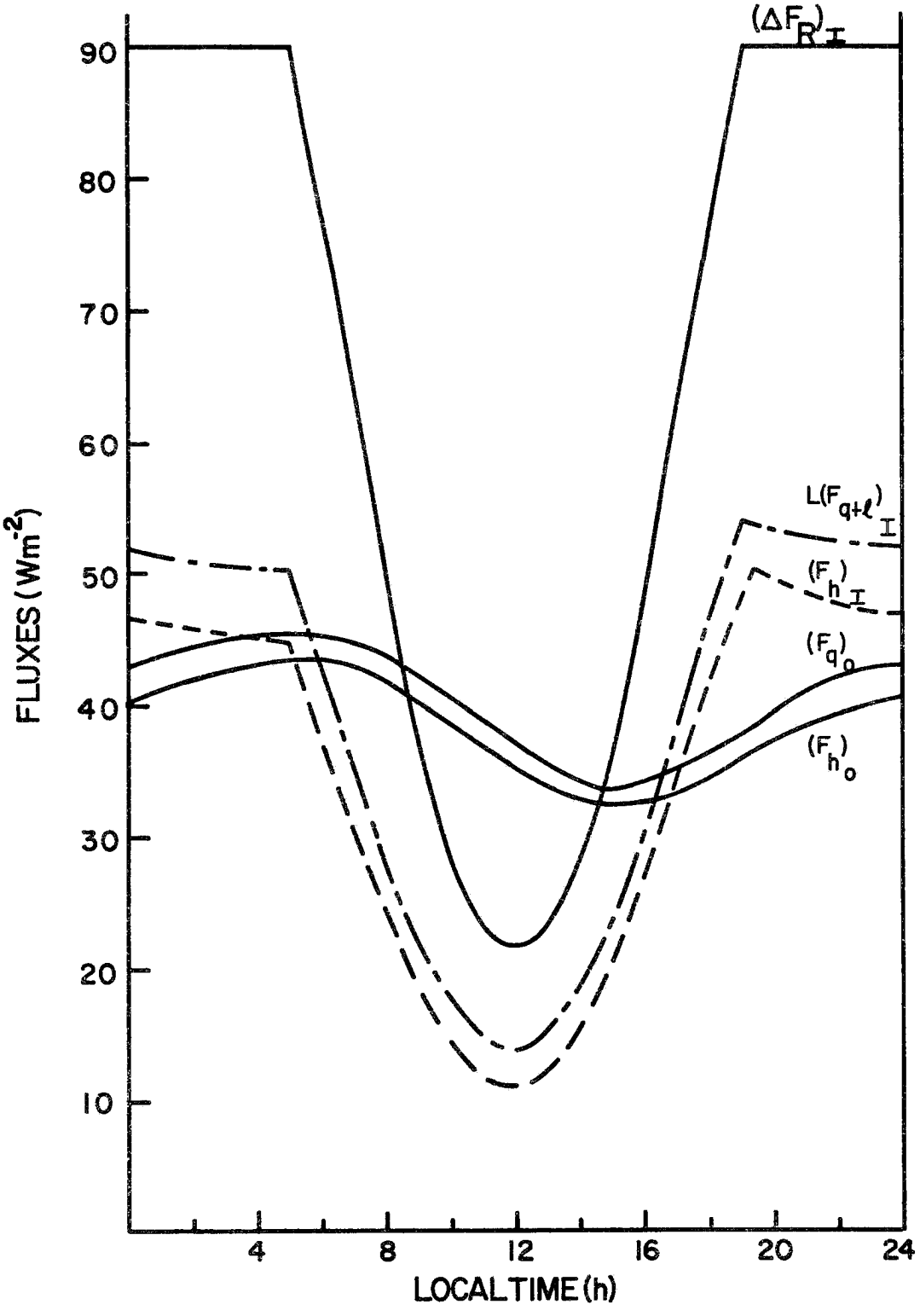

Figure 45b. Same as 45a but for results shown in 44b.

The exact relationship of the closure assumptions made for both models is not obvious. However, both closure schemes insure that the inequality

$$\int_0^{\hat{p}_I} (F_{SV})\, d\hat{p} \geq 0$$

is satisfied. It is encouraging, however, that neither model is extremely sensitive to the specification of closure parameters. Furthermore, although the closure assumptions for the two results are not identical, the fact that the results are quantitatively similar indicates that these assumptions are not crucial to the results. The "trade-cumulus" model does not, however, reduce exactly to Lilly's model. It is possible in Lilly's model for the integral of the virtual dry static energy flux in the subcloud layer to be less than zero. In the "trade-cumulus" model the integral of the virtual dry static energy flux in the subcloud layer is always greater than or equal to zero. Situations in which this difference in the closure assumptions results in significant differences in the predicted results have not been encountered.

F. Summary

In this chapter the fluxes discussed in Chapter III and IV were combined with the predictive equations derived in Chapter II. These equations were integrated numerically to predict the time variation of the boundary layer structure. The boundary layer structure was

predicted with the sea surface temperature, surface wind speed, and large-scale divergence values obtained from the ship Planet during ATEX. The model was initialized with a mixed layer 40 mb in depth. After 48 h of integration the solutions approached steady-state. The boundary layer structure predicted agreed reasonably well with the thermodynamic structure observed from the Planet. The predicted solution, however, was slightly warmer and more moist than that observed. These differences were shown to be principally due to the neglect of horizontal advection in the model. The model fluxes agreed well with those obtained from ATEX and BOMEX budget studies.

The sensitivity of the solutions to various parameters was assessed. The model solutions were shown to be relatively insensitive to τ_{adj}, ΔT_o and the mixed layer k. This is encouraging since these parameters may be difficult to define accurately from measurements. The height of the inversion and the thermodynamic structure below the inversion were shown to be sensitive to sea surface temperature, surface wind speed, large-scale divergence, average boundary layer radiative heating and radiatively active cloud cover.

The time dependent capability of the model was demonstrated by simulating the reformation of the trade-wind boundary layer structure in the wake of disturbed conditions. The initial growth rate of the boundary layer was shown to be most sensitive to parameters and conditions which directly control the surface fluxes.

The variation of the height of the inversion to diurnally varying solar heating and diurnally varying large-scale divergence was predicted with the model. The results obtained by simultaneously considering the

effect due to radiation and that due to divergence resulted in the best agreement between the observed and the predicted diurnal variations of the inversion height.

The model was used to simulate the atmospheric structure when the cloud layer becomes saturated. The steady-state and time-dependent results obtained with the model are in excellent agreement with the theoretical stratocumulus results of Lilly (1968) and Schubert (1976).

VI. CONCLUSIONS

This paper presents the development and testing of a one-dimensional predictive model of the trade-wind boundary layer. The analysis is simplified by assuming that moist static energy and water vapor mixing ratio are constant with pressure in the subcloud layer and linear with pressure in the cloud layer. The subcloud and cloud layer are separated by a transition layer which is assumed to be infinitesimally thin and the upper boundary of the model is defined by the trade inversion which is also assumed to be infinitesimally thin. Heat and moisture budgets are used to derive equations which express the time variation of this simplified structure in terms of the large-scale subsidence (a specified parameter) and convective and radiative fluxes. These equations may be integrated numerically provided the convective and radiative fluxes are defined in terms of the boundary-layer structure itself.

The surface fluxes of heat and moisture are given by a bulk aerodynamic formulation while fluxes at the top of the subcloud layer are specified with a mixed-layer parameterization. The cloud-layer fluxes are represented as the product of a mass flux term which is linear with pressure and a cloud-environment difference in thermodynamic quantities which is linear with pressure. Closure is obtained by assuming that cloud-base is at the transition layer, the cloud-environment difference in virtual temperature averaged over the depth of the cloud layer is a constant, ΔT_o, and by assuming an adjustment time, τ_{adj}, that is constant. The numerical results indicate that the model structure is relatively insensitive to the specification of ΔT_o or τ_{adj}.

Radiative transfer calculations were performed and show that the average radiative heating in the cloud layer is relatively insensitive to variations in temperature, moisture, and cloud cover within the boundary layer. The vertical distribution of the radiative heating does, however, vary significantly with the amount of boundary layer cloudiness. In the clear atmosphere the longwave cooling and shortwave heating are nearly uniformly distributed within the boundary layer. In clouds, however, the heating and cooling are confined to a thin layer at cloud top. This cloud top radiative heating and cooling is explicitly included in the budget equations used to predict the height of the inversion in the model.

The model described above was integrated numerically assuming a sea surface temperature and large-scale subsidence field which were consistent with observations made from the ship Planet during ATEX. The model structure predicted was in good agreement with the observed structure. The predicted structure was, however, slightly warmer and more moist than that observed. These discrepancies were shown to result from the neglect of the horizontal advection terms in the budget equations.

The steady-state thermodynamic structure below the inversion is shown to be sensitive to the specification of surface wind speed, sea surface temperature, radiative heating and cloud cover. The height of the inversion depends on these parameters and also on the specification of the large-scale divergence.

The reformation of the inversion in the wake of disturbed conditions was simulated by assuming an initial structure consisting of a mixed layer 40 mb in depth that was cooler and drier than the Planet structure. After 32 h of simulation, the predicted structure was similar to that observed. The initial growth rate of the depth of the

boundary layer was shown to be most sensitive to the specification of parameters and conditions which directly control the surface fluxes. These results indicate that the trade inversion can easily form from a shallow dry mixed layer.

The variation of the height of the inversion to a diurnally varying solar heating and a dirunally varying large-scale divergence was predicted with the model. The results obtained by simultaneously considering the effect due to radiation and that due to divergence resulted in the best agreement between the observed and the predicted variations of the inversion height.

The model was also used to simulate the thermodynamic structure for conditions where the cloud layer is saturated (assuming no precipitation). The steady-state and time-dependent results of this simulation are in excellent agreement with the theoretical results obtained from the stratocumulus model described by Lilly (1968) and Schubert (1976).

The results presented in this dissertation suggest several future avenues of research for the improvement and application of the model. Detailed cumulus models (see review by Cotton, 1975), for example, may be useful in better defining ΔT_o and τ_{CLD} and any possible relationship between these variables for trade-wind cumulus. The detailed turbulence model of Sommeria (1976) may also be useful in further evaluating the generality of the ΔT_o and τ_{adj} parameters. These parameters may be of different magnitudes for non-precipitating convective systems other than those of the trade winds. The convective heat flux obtained by Betts (1976b) for diurnal convection over Venezuela, for example, is an order of magnitude greater than the BOMEX and ATEX fluxes. Consequently, the effect that these larger heat fluxes might have on the closure parameters

should be evaluated if convection over land is to be simulated. It is also obvious that the model results should be compared with additional observations. In particular, the reformation of the boundary layer structure in the wake of disturbed conditions needs to be compared with observations in order to verify the time-dependent characteristics of the model. Aircraft or radiometersonde observations would be useful in verifying the average boundary layer radiative heating and its variability. An investigation into the magnitude of solar radiative heating and diurnal variations in the large-scale subsidence would be useful in clarifying diurnal variations in the trades. It would also be useful to parameterize the visible cloud cover so that it would be a predicted rather than a specified parameter in the model. Such a parameterization would allow the model to be applied in both trade cumulus and stratocumulus conditions without externally respecifying the radiative fluxes. In general, the use of the model to simulate stratocumulus conditions also needs to be studied more carefully. A model which realistically simulates the structure of the atmosphere for both stratocumulus and trade-cumulus conditions would be an extremely useful tool for increasing our understanding of the undisturbed convective boundary layer.

REFERENCES

Albrecht, B., M. Poellot, and S.K. Cox, 1974: Pyrgeometer measurements from aircraft. Rev. Sci. Instrum., 45, 33-38.

_____, and S.K. Cox, 1975: The large-scale response of the tropical atmosphere to cloud modulated infrared heating. J. Atmos. Sci., 32, 16-24.

_____, and S.K. Cox, 1976: Radiation data reduction procedures for Sabreliner, C-130, and DC-6 aircraft during the GARP Atlantic Tropical Experiment. Colorado State University, Atmospheric Science Paper No. 244, 100 pp.

_____, and S.K. Cox, 1977: Procedures for improving pyrgeometer performance. J. Appl. Meteor., 16, 188-197.

Arakawa, A., and W.H. Schubert, 1974: Interaction of cumulus cloud ensemble with the large-scale environment, Part I. J. Atmos. Sci., 31, 674-701.

Augstein, A., H. Riehl, F. Ostapoff, and V. Wagner, 1973: Mass and energy transports in an undisturbed Atlantic trade wind flow. Mon. Wea. Rev., 101, 101-111.

Augstein, E., H. Schmidt, F. Ostapoff, 1974: The vertical structure of the atmospheric planetary boundary layer in undisturbed trade winds over the Atlantic ocean. Boundary Layer Met., 6, 129-150.

Betts, A.K., 1973: Non-precipitating cumulus convection and its parameterization. Quart. J. Roy. Meteor. Soc., 86, 178-196.

_____, F.J. Dugan and R.W. Grover, 1974: Residual errors of the VIZ radiosonde hygristor as deduced from observations of the sub-cloud layer structures. Bull. Amer. Met. Soc., 55, 1123-1125.

_____, 1975: Parametric interpretation of trade-wind cumulus budget studies. J. Atmos. Sci., 32, 1934-1945.

_____, 1976a: The thermodynamic transformation of the tropical subcloud layer by precipitation downdrafts. J. Atmos. Sci., 33, 1008-1020.

_____, 1976b: Modeling subcloud layer structure and interaction with a shallow cumulus layer. J. Atmos. Sci., 33, 2363-2382.

Bunker, A.F., B. Haurwitz, J.S. Malkus, and H. Stommel, 1949: Vertical distribution of temperature and humidity over the Caribbean sea. Pap. Phys. Oceanog. and Meteor., Mass. Inst. of Tech. and Woods Hole Ocean. Ins., 11, 82 pp.

REFERENCES - Continued

Conte, S.D., 1965: Elementary Numerical Analysis. McGraw-Hill, New York, 278 pp.

Cotton W.R., 1975: Theoretical cumulus dynamics. Rev. of Geo. Spa. Phy., 13, 419-447.

Cox, S.K., 1968: A radiation model in which the effects of clouds are simulated from moisture and temperature parameters. Annual Report of WBG 88, Dept. of Meteorology, Univ. of Wisconsin, 2-50.

_____, 1969: Observational evidence of anomalous infra-red cooling in a clear tropical atmosphere. J. Atmos. Sci., 26, 1347-1349.

_____, 1973: Infrared heating calculations with a water vapor pressure broadened continuum. Quart. J. Roy. Meteor. Soc., 99, 669-679.

Deardorff, J.W., 1972: Numerical investigations of neutral and unstable boundary layers. J. Atmos. Sci., 29, 91-115.

Esbensen, S., 1976: Thermodynamic effects of clouds in the trade wind planetary boundary layer. Ph.D. Thesis. U.C.L.A., 110 pp.

Feigel'son, E.M., 1973: Radiant heat transfer in a cloudy atmosphere. Transl. from Russian by IPST, Jerusalem, 191 pp.

Ficker, H. von, 1936: Die passatinversion. Veroff. Meteor. Inst., Berlin, 1, 33 p.

Fissel, D.B., S. Pond, and M. Miyake, 1977: Computation of surface fluxes from climatological and synoptic data. Mon. Wea. Rev., 105, 26-36.

Fraedrich, K., 1973: On the parameterization of cumulus convection by lateral mixing and compensating subsidence, Part I. J. Atmos. Sci., 30, 408-413.

_____, 1976: A mass budget of an ensemble of transient clouds determined from direct cloud observations. J. Atmos. Sci., 33, p. 262-268.

Friche, C.A., and K.F. Schmitt, 1976: Parameterization of air sea interface fluxes of sensible heat and moisture by the bulk aerodynamic formulas. J. Phys. Oceanogr., 6, 801-809.

Griffith, K., 1977: Radiative properties of clouds inferred from broadband measurements. Master's Thesis, Department of Atmospheric Science, Colorado State University.

REFERENCES - Continued

Holland, J. and E. Rasmusson, 1973: Measurements of the atmospheric mass, energy, and momentum budgets over a 500-kilometer square of tropical ocean. Mon. Wea. Rev., 101, 44-55.

Kondratyev, K.Ya., et al., 1976: Aerosol in the GATE area and its radiative properties. Colorado State University Atmospheric Science Paper No. 247, Fort Collins, Colorado.

Kuo, H.L., 1965: On the formation and intensification of tropical cyclones through latent heat release by cumulus convection. J. Atmos. Sci., 22, 40-63.

_____, 1974: Further studies of the parameterization of the influence of cumulus convection on large-scale flow. J. Atmos. Sci., 31, 1232-1240.

LeMone, M.A., and W.T. Pennell, 1976: The relationship of trade wind cumulus distribution to subcloud layer fluxes and structure. Mon. Wea. Rev., 104, 524-539.

Lilly, D.K., 1968: Models of cloud topped mixed layers under a strong inversion. Quart. J. Roy. Met. Soc., 94, p. 292-309.

Lindzen, R.S., 1967: Thermally driven diurnal tide in the atmosphere. Quart. J. Roy. Met. Soc., 93, 18-42.

Liou, K-N, 1976: On the absorption, reflection and transmission of solar radiation in cloudy atmospheres. J. Atmos. Sci., 5, 798-505.

Mak, Man Kin, 1976: A study of the downstream variation of the lower trade-wind circulation. Tellus, 28, 97-107.

Malkus, J.S., 1956: On the maintenance of the trade winds. Tellus, 3, 335-350.

_____, 1958: On the structure of the trade wind moist layer. Pap. in Phys. Oceanog. and Meteor., Mass. Inst. of Tech. and Woods Hole Ocean. Inst., XII, No. 2, 47 pp.

Manabe, S. and F. Möller, 1961: On the radiative equilibrium and heat balance of the atmosphere. Mon. Wea. Rev., 89, 503-532.

_____, and R.F. Strickler, 1964: Thermal equilibrium of the atmosphere with a convective adjustment. J. Atmos. Sci., 24, 361-385.

McKee, T., and S. Cox, 1974: Scattering of visible radiation by finite clouds. J. Atmos. Sci., 31, 1885-1892.

_____, and S.K. Cox, 1976: Simulated radiance patterns for finite cubic clouds. J. Atmos. Sci., 33, 2014-2020.

REFERENCES - Continued

Murray, F.W., 1967: On the computation of saturation vapor pressure. J. Appl. Meteor., 6, 203-204.

Nitta, T., and S. Esbensen, 1974: Heat and moisture budgets using BOMEX data. Mon. Wea. Rev., 102, 17-28.

_____, 1975: Observational determination of cloud mass flux distributions. J. Atmos. Sci., 32, 73-91.

Ogura, Y., and H-R. Cho, 1974: On the interaction between the subcloud and cloud layers on tropical regions. J. Atmos. Sci., 31, 1850-1859.

Ooyama, K., 1971: A theory on parameterization of cumulus convection. J. Met. Soc., Japan, 49, (special issue), 744-756.

Paltridge, G.W., 1974: Infrared emissivity, short-wave albedo, and the microphysics of stratiform water clouds. J. of Geophys. Res., 79, p. 4053-4058.

Reynolds, D.W., T.H. Vonder Haar and S.K. Cox, 1975: The effect of solar radiation absorption in the tropical troposphere. J. Appl. Meteor., 14, 433-444.

Riehl, H., T.C. Yeh, J.S. Malkus, and N.E. LaSeur, 1951: The north-east trade of the pacific ocean. Quart. J. Roy. Met. Soc., 72, 598-626.

_____, and J.S. Malkus, 1957: On the heat balance and maintenance of circulation in the trades. Quart. J. Roy. Meteor. Soc., 83, 21-28.

Sarachik, E.S., 1974: The tropical mixed layer and cumulus parameterization. J. Atmos. Sci., 31, p. 2225-2230.

Schubert, W.H., 1976: Experiments with Lilly's cloud-topped mixed layer model. J. Atmos. Sci., 33, p. 436-446.

Sequin, W.R., and M. Garstang, 1976: Some evidence of the effects of convection on the structure of the tropical subcloud layer. J. Atmos. Sci., 33, p. 660-666.

Sommeria, G., 1976: Three dimensional simulation of turbulent processes in the undisturbed trade wind boundary layer. J. Atmos. Sci., 33, 216-241.

Staley, D.O., 1965: Radiative cooling in the vicinity of inversions and the tropopause. Quart. J. Roy. Met. Soc., 91, p. 282-301.

REFERENCES - Continued

Starr, D. O'C., 1976: The sensitivity of tropical radiative budgets to cloud distribution and the radiative properties of clouds. Colorado State University, Atmospheric Science Paper No. 254, 117 p.

Stull, R.B., 1976a: The energetics of entrainment across a density interface. J. Atmos. Sci., 33, 1260-1267.

_____, 1976b: Mixed-layer depth model based on turbulent energetics. J. Atmos. Sci., 33, 1268-1278.

Tennekes, H., 1973: A model for the dynamics of the inversion above a convective boundary layer. J. Atmos. Sci., 30, 558-567.

Twomey, S., 1976: Computations of the absorption of solar radiation by clouds. J. Atmos. Sci., 33, 1087-1091.

Warner, J., 1955: The water content of cumuliform clouds. Tellus, 7, 449-457.

Yamamoto, G., M. Tanaka and S. Asano, 1970: Radiative transfer in water clouds in the infrared region. J. Atmos. Sci., 27, 282-292.

Yanai, M., S. Esbensen and J.H. Chu, 1973: Determination of bulk properties of tropical cloud clusters from large-scale heat and moisture budgets. J. Atmos. Sci., 30, 611-627.

_____, J-H. Chu, T.E. Stark and T. Nitta, 1976: Response of deep and shallow maritime cumuli to large-scale processes. J. Atmos Sci., 33, 976-991.

APPENDIX A.

AN EXPRESSION FOR THE TIME VARIATION OF THE HEIGHT OF CLOUD BASE

Differentiation of (III.22) with respect to time gives

$$\frac{1}{(q_M + \delta q)} \frac{\partial q_M}{\partial t} = \frac{p_o - p_B}{e_s\, p^*} \frac{\partial e_s}{\partial t} + \frac{1}{p^*} \frac{\partial \hat{p}_B}{\partial t} \qquad (A.1)$$

where $p^* \equiv \hat{p}_o - p_B - e_s$ and $\frac{\partial(\partial q)}{\partial t} = 0$. The saturation vapor pressure, e_s, may be determined from Teton's Formula (Murray, 1976) as

$$e_s = 6.1078 \text{ (mb)} \exp\left[\frac{a(T - 273.16)}{(T - b)}\right] \qquad (A.2)$$

where a = 17.27, b = 35.86, and T is in degrees K.

Eq. (A.2) may be evaluated at $T=T_B+\delta t$ and differentiated w.r.t. time to give the expression

$$\frac{1}{e_s} \frac{\partial e_s}{\partial t} = \frac{1}{T^*} \frac{\partial T_B}{\partial t} \qquad (A.3)$$

where $T^* = 4098.0/(T_B + \delta T - 35.86)^2$, e_s is evaluated at the temperature $T_B + \delta T$, and it is assumed that $\frac{\partial(\delta T)}{\partial t} = 0$. The temperature at the top of the mixed layer is given from (D-3) of Appendix D as

APPENDIX A. - Continued

$$T_B = \frac{s_M}{c_p} \left(\frac{p_o - \hat{p}_B}{p_o}\right)^{\kappa} . \tag{A.4}$$

Eq. (A.4) may be differentiated with respect to time to give

$$\frac{\partial T_B}{\partial t} = \frac{T_B}{s_M} \frac{\partial s_M}{\partial t} - \left(\frac{\kappa T_B}{p_o - \hat{p}_B}\right) \frac{\partial \hat{p}_B}{\partial t} \tag{A.5}$$

where it is assumed that $\frac{\partial p_o}{\partial t} = 0$.

Combining Eqs. A5, A3, and A2, and solving for $\frac{\partial \hat{p}_B}{\partial t}$ gives

$$\frac{\partial \hat{p}_B}{\partial t} = \frac{T^* p^*}{(T^* - \kappa T_B)} \frac{1}{(q_M + \delta q)} \frac{\partial q_M}{\partial t} - \frac{(p_o - \hat{p}_B) T_B}{(T^* - \kappa T_B) s_M} \frac{\partial s_M}{\partial t}$$

APPENDIX B.

LINEAR EXPRESSIONS FOR CLOUD-ENVIRONMENT DIFFERENCES IN THERMODYNAMIC VARIABLES

To linearize the equations for the cloud-environment differences, Eq. (III.30) and (III.31), it is assumed that the linearized cloud-environment differences integrated through the depth of the layer are equivalent to the integral of the exact expressions. This assumption may be written as

$$\int_0^{\delta\hat{p}} \left\{\left[\frac{\gamma_h\,\delta\hat{p}}{E} - (\Delta h)_{CB}\right] \exp\left(\frac{-Ep'}{\delta p}\right) - \frac{\gamma_h\,\delta\hat{p}}{E}\right\} dp' \tag{B.1}$$

$$= \int_0^{\delta\hat{p}} -(\Delta h)_{CB}\,(1 + \lambda_h p')\,dp'$$

and

$$\int_0^{\delta p} \left\{\left[\frac{\gamma_q\,\delta\hat{p}}{E} - (\Delta q)_{CB}\right] \exp\left(-\frac{Ep'}{\delta\hat{p}}\right) - \frac{\gamma_q\,\delta\hat{p}}{E}\right]\right\} dp' \tag{B.2}$$

$$= \int_0^{\delta p} -(\Delta q)_{CB}\,(1 + \lambda_q\, p')\,dp' \,.$$

APPENDIX B. - Continued

A linearization based on the integral of the exact solution is used since an integral constraint is applied to the cloud-environment differences in order to determine E.

If the integrals in (B.1) and (B.2) are evaluated, λ_h and λ_q are given as

$$\lambda_h = 2 \left(\frac{\gamma_h}{(\Delta h)_{CB}} - \frac{E}{\delta \hat{p}}\right) \left(\frac{\exp(-E) - 1 + E}{E^2}\right) \tag{B.3}$$

and

$$\lambda_q = 2 \left(\frac{\gamma_q}{(\Delta q)_{CB}} - \frac{E}{\delta \hat{p}}\right) \left(\frac{\exp(-E) - 1 + E}{E^2}\right). \tag{B.4}$$

Expressing the exponential term as $\exp(-E) = 1 - E + \frac{E^2}{2} - \frac{E^3}{2 \cdot 3} + \ldots\ldots$ allows (B.3) and (B.4) to be approximated as

$$\lambda_h = \left[\frac{\gamma_h}{(\Delta h)_{CB}} - \frac{E}{\delta \hat{p}}\right] \left(1 - \frac{E}{3}\right) \tag{B.5}$$

$$\lambda_q = \left[\frac{\gamma_q}{(\Delta q)_{CB}} - \frac{E}{\delta \hat{p}}\right] \left(1 - \frac{E}{3}\right) \tag{B.6}$$

where terms $O(E^4)$ have been ignored.

APPENDIX C.

EXPRESSION FOR VIRTUAL DRY STATIC ENERGY CLOUD-ENVIRONMENT DIFFERENCES

The definition of cloud-environment differences of virtual dry static energy given in (III.41) may be written as

$$(s_{vc}-\bar{s}_v) = (s_c-\bar{s}) + \varepsilon L(1+\delta)\,(q_c-\bar{q}) - \varepsilon L(\ell_c + q_c - \bar{q}). \qquad (C.1)$$

Following the derivation given by Arakawa and Schubert (1974) it is convenient to note that

$$s_c-\bar{s} = \frac{1}{1+\gamma}\,(h_c-\bar{h}^*) \qquad (C.2)$$

and

$$q_c-\bar{q}^* = \frac{\gamma}{1+\gamma}\,\frac{1}{L}\,(h_c-\bar{h}^*) \qquad (C.3)$$

where

$$\gamma \equiv \frac{L}{c_p}\frac{\partial \bar{q}^*}{\partial \bar{T}})_{\hat{p}}$$

With slight additional manipulation (C.2) and (C.3) may be written as

$$(s_c-\bar{s}) = \frac{1}{1+\gamma}\,(h_c-\bar{h}) - \frac{L}{(1+\gamma)}\,(\bar{q}^* - \bar{q}) \qquad (C.4)$$

APPENDIX C. - Continued

and $$(q_c-\bar{q}) = \frac{\gamma}{L(1+\gamma)}(h_c-\bar{h}) + \frac{1}{1+\gamma}(\bar{q}^*-\bar{q}). \qquad (C.5)$$

If (C.4) and (C.5) are used in (C.1) the expression which results is

$$(s_{vc}-\bar{s}_v) = \frac{1 + \gamma\varepsilon(\delta+1)}{1+\gamma}(h_c-\bar{h}) - \varepsilon L(l_c + q_c - \bar{q}) - \frac{L(1 - \varepsilon(1+\delta))}{1+\gamma}(\bar{q}^* - \bar{q}). \qquad (C.6)$$

Since $(h_c-\bar{h})$ and $(q_c + l_c - \bar{q})$ have been expressed as linear expressions in Chapter III it is convenient to write $\bar{q}^*$ as

$$\bar{q}^* = \bar{q}_B^* + \gamma_q^* p'. \qquad (C.7)$$

Appropriate expressions for γ_q^* and q_B^* are given in Appendix D. With (C.7), (III.32), and (III.33), (C.6) may be written as

APPENDIX C. - Continued

$$(s_{vc}-\bar{s}_v) = -\beta(\Delta h)_{CB}\,(1 + \lambda_h p') + \varepsilon L(\Delta q)_{CB}\,(1 + \lambda_q p')$$

$$-\alpha L[q_B^* - q_B + (\gamma_q^* - \gamma_q)\,p'] \qquad (C.8)$$

where $$\beta = \frac{1 + \gamma\varepsilon(1 + \delta)}{1 + \gamma}$$

and $$\alpha = \frac{1 - \varepsilon(1 + \delta)}{1 + \gamma}\,.$$

Values of γ, α and β calculated from the trade wind structure shown in Fig. 1 are given in Table C.I as a function of pressure.

Pressure (mb)	γ	α	β
925	1.854	.284	.474
905	1.755	.294	.484
885	1.660	.305	.494
865	1.567	.316	.505
845	1.473	.328	.517

Table C.I Values of γ, α and β calculated from ship Planet ATEX data (Feb. 7-11).

APPENDIX D.

EXPRESSIONS FOR TEMPERATURE AND SATURATION MIXING RATIO IN THE SUBCLOUD AND CLOUD LAYER

The temperature in the mixed layer is obtained by noting that the subcloud layer value of dry static energy is constant with pressure and given as

$$s = c_p T + gz. \tag{D.1}$$

Differentiation of (D.1) with respect to $\hat{p}$ gives

$$c_p \frac{dT}{d\hat{p}} = \frac{RT}{(p_o - \hat{p})} \tag{D.2}$$

where hydrostatic approximation has been made. Integrating (D.2) and noting that $T = s_M/c_p$ at $\hat{p} = 0$ results in the expression

$$T = \frac{s_M}{c_p} \left(\frac{p_o - \hat{p}}{p_o}\right)^{\kappa} \tag{D.3}$$

where $\kappa = R/c_p$.

APPENDIX D. - Continued

The saturation mixing ratio at any level $\hat{p}$ may be evaluated as

$$q^*(\hat{p}) = \frac{\varepsilon e_s(T)}{p_o - \hat{p} - e_s(T)} \qquad (D.4)$$

where $\varepsilon = .622$ and $e_s(T)$ is the saturation vapor pressure at the temperature T. In the subcloud layer (D.3) may be used to evaluate the temperature at any level and Teton's formula (Eq. A.2) may be used to calculate $e_s(T)$.

It is convenient in the cloud layer to express the temperature and saturation mixing ratio as linear functions of pressure. In the cloud layer the dry static energy is given as

$$s = s_A + \gamma_s(\hat{p} - \hat{p}_A) = c_p T + gz \qquad (D.5)$$

for $\hat{p}_B < \hat{p} < \hat{p}_I$.

Differentiation of (D.5) w.r.t. $\hat{p}$, employing the hydrostatic approximation, separating variables and integrating results in the expression

$$T = -\frac{\gamma_s}{c_v}(p_o - \hat{p}) + [T_{B+} + \frac{\gamma_s}{c_v}(p_o - \hat{p}_B)]\left[\frac{p_o - \hat{p}}{p_o - \hat{p}_B}\right]^{\kappa} \qquad (D.6)$$

APPENDIX D. - Continued

where c_v is the specific heat of dry air at constant specific volume and T_{B+} is the air temperature just above the transition layer. For a cloud layer approximately 100 mb in depth $\frac{\hat{p}_o - \hat{p}_B}{(p_o - \hat{p}_B)} << 1$ so that (D.6) may be written approximately as

$$T \simeq T_{B+} + \gamma_T (\hat{p} - \hat{p}_B) \qquad (D.7)$$

where $$\gamma_T = \frac{\gamma_s}{c_p} - \frac{\kappa T_{B+}}{(p_o - \hat{p}_B)}.$$

For a typical trade cumulus structure (D.7) differs from (D.6) by less than .5°C at all levels.

The saturation mixing ratio in the cloud layer is given by using (D.4) with (A.2) where the temperature needed in these expressions is given by either (D.6) or (D.7). Again, however, it is desirable to express the mixing ratio as a linear function of pressure. If the temperature, T, is expressed from (D.7) as $T = T_{B+} + T'$ where $T' = \gamma_T (\hat{p} - \hat{p}_B)$ and it is noted that $T'/(T_{B-} - b)$ is typically << 1, Teton's formula may be approximated as

$$e_s \simeq e_{sB} (1 + K_1 T') \qquad (D.8)$$

APPENDIX D. - Continued

where $e_{sB} = e_s\ (T_{B+})$ and $K_1 = \frac{a(273.16 - b)}{(T_{B+} - b)^2}$.

It is convenient to define $p' \equiv \hat{p} - \hat{p}_B$ so that (D.4) may be approximated to the same order of approximation as (D.8) as

$$q^* \simeq \frac{\varepsilon_s\ e_s}{p_o - \hat{p}_B}\left[1 + \frac{p' + e_s}{(p_o - \hat{p}_B)}\right]. \qquad (D.9)$$

(D.8) and (D.9) may be combined to give an approximate linear expression for q of

$$q^* \simeq q_B^* + \gamma_q^*\ p' \qquad (D.10)$$

where $$q_B^* = \frac{\varepsilon_s\ e_{sB}}{(p_o - \hat{p}_B)}\left[1 + \frac{e_{sB}}{(p_o - \hat{p}_B)}\right]$$

and $$\gamma_q^* = \frac{\varepsilon_s\ e_{sB}}{(p_o - \hat{p}_B)}\left[K_1\gamma_T + \frac{1 + K_1\gamma_T\ e_{sB}}{(p_o - \hat{p}_B)}\right].$$

and all terms $O(p'^2)$ have been ignored. For a typical trade cumulus structure (D.10) gives the $\simeq$ .2 g/kg of the actual value at all levels.

APPENDIX E.

EXPRESSIONS FOR THE RADIATIVE FLUXES IN TERMS OF HEATING RATES

The radiative fluxes which appear in the predictive equations may be written by definition in terms of the heating rates as

$$-\frac{g}{c_p}\frac{[(F_R)_{I+} - (F_R)_0]}{\hat{p}_I} = (1-\sigma_R)\,(Q_R)_0^{CLR} + \sigma_R(Q_R)_0^{CLD} \qquad (E.1)$$

$$-\frac{g}{c_p}\frac{[(F_R)_{I-} - (F_R)_B]}{\delta\hat{p}} = (1-\sigma_R)\,(Q_R)_C^{CLR} + \sigma_R(Q_R)_C^{CLD} \qquad (E.2)$$

and $$-\frac{g}{c_p}\frac{[(F_R)_B - (F_R)_0]}{\hat{p}_B} = (1-\sigma_R)\,(Q_R)_M^{CLR} + \sigma_R(Q_R)_M^{CLD} \qquad (E.3)$$

Since the expressions (E.1) - (E.3) relate the heating rates to a difference in the fluxes and since the heating rates are specified parameters, one of the fluxes in these expressions is arbitrary from the point of view of the energetics of the layer. It is convenient in this formulation to assume $(F_R)_{I+}$ is arbitrary. Eq. (E.1) and (E.2) may then be rewritten as

$$(F_R)_0 = (F_R)_{I+} + \frac{c_p}{g}\left[(1-\sigma_R)\,(Q_R)_0^{CLR} + \sigma_R(Q_R)_0^{CLD}\right]\hat{p}_I \qquad (E.4)$$

APPENDIX E. - Continued

$$\text{and} \quad (F_R)_B = (F_R)_{I+} + \frac{c_p}{g}\left[(1-\sigma_R)(Q_R)_O^{CLR} + \sigma_R(Q_R)_O^{CLD}\right]\hat{p}_I$$

$$- \frac{c_p}{g}\left[(1-\sigma_R)(Q_R)_M^{CLR} + \sigma_R(Q_R)_M^{CLD}\right]\hat{p}_B. \tag{E.5}$$

Since for the clear sky heating rates

$$(Q_R)_O^{CLR} = \frac{\{(Q_R)_M^{CLR}\,\hat{p}_B + (Q_R)_C^{CLR}\,\delta\hat{p}\}}{\hat{p}_I}. \tag{E.6}$$

(E.6) and (E.5) may be combined to give

$$(F_R)_{I-} = (F_R)_{I+} + \frac{c_p}{g}\sigma_R(Q_R)_O^{CLD}\,\hat{p}_I$$

$$- \frac{c_p}{g}\sigma_R\left[(Q_R)_M^{CLD}\,\hat{p}_B + (Q_R)_C^{CLD}\,\delta\hat{p}\right]. \tag{E.7}$$

Using the definitions given above the flux at the midpoint of the cloud layer may be written as

APPENDIX E. - Continued

$$(F_R)_A = \frac{c_p}{g} \{[(Q_R)_{CT}^{CLR} - (Q_R)_{CB}^{CLR}] (1-\sigma_R) + [(Q_R)_{CT}^{CLD} - (Q_R)_{CB}^{CLR}] \sigma_R\} \frac{\hat{\delta p}}{4}$$

$$+ [(F_R)_{I-} + (F_R)_B] / 2.0. \qquad (E.8)$$

Eq. (E.4) - (E.8) express the fluxes $(F_R)_O$, $(F_R)_B$, $(F_R)_I$ and $(F_R)_A$ in terms of the specified radiative heating rates.

APPENDIX F.

RUNGE-KUTTA SOLUTION TO A SET OF ORDINARY DIFFERENTIAL EQUATIONS

The differential equations used to solve the boundary layer model may be written as a set of M equations and M unknowns of the form

$$\frac{dy_m}{dt} = f_m\,(t, y_1, y_2, \ldots y_M) \qquad (F.1)$$

where $m = 1, 2, \ldots M$. The Runge-Kutta method used to solve these equations (c.f. Conte, 1965) may be written as

$$y_m^{(n+1)} = y_m^{(n)} + \frac{1}{6}\,(k_{1,m} + 2k_{2,m} + 2k_{3,m} + k_{4,m}) \qquad (F.2)$$

where Δt is the time step used in the integration so that $t = n\Delta t$. The factors $k_{1,m}$, $k_{2,m}$, $k_{3,m}$ and $k_{4,m}$ which appear in (F.2) may be written as

$$k_{1,m} = \Delta t\, f_m\,(t, y_1^{(n)}, y_2^{(n)} \ldots y_M^{(n)}), \qquad (F.3)$$

APPENDIX F. - Continued

$$k_{2,m} = \Delta t\, f_m \left(t + \Delta t/2,\ y_1^{(n)} + \frac{k_{1,1}}{2},\ y_2^{(n)}\right.$$

$$\left. + \frac{k_{1,2}}{2} \ldots\ y_M(n) + \frac{k_{1,M}}{2}\right), \tag{F.4}$$

$$k_{3,m} = \Delta t\, f_m \left(t + \Delta t/2,\ y_1^{(n)} + \frac{k_{2,1}}{2},\ y_2^{(n)}\right.$$

$$\left. + \frac{k_{2,2}}{2},\ \ldots\ y_M^{(n)} + \frac{k_{2,M}}{2}\right), \tag{F.5}$$

and

$$k_{4,m} = \Delta t\, f_m \left(t + \Delta t,\ y_1^{(n)} + k_{3,1},\ y_2^{(n)}\right.$$

$$\left. + k_{3,2} \ldots\ y_M^{(n)} + k_{3,M}\right). \tag{F.6}$$